

Inflationary Model Selection ft. Dark Matter in the CMB



Wei Chieh Ng

Department of Physics
The University of Auckland

Supervisor: Professor Richard Easther

A dissertation submitted in partial fulfilment of the requirements for the degree of BSc (Hons)
in Physics, The University of Auckland, 2017.

Abstract

With the ever evolving volume of cosmological data available, we need a way to distinguish between different inflationary models in a robust manner. We apply Bayesian model comparison to selected inflationary models with a monomial inflaton potential. We also incorporate the new inflection point inflation model in the analysis and compare its predictions and Bayesian evidence to the other inflaton potentials.

We use Bayesian evidence to quantify the model comparison. This usually involves a multi-dimensional integral which is typically very computationally expensive. However, we employ `PolyChord`, a novel nested sampling algorithm that efficiently samples high-dimensional parameter spaces. This is coupled with `ModeCode`, the inflationary perturbation equation solver. We also couple them with `CosmoMC` for post-inflationary cosmological parameter estimation.

We also quantify the impacts of dark matter in explaining the cosmic microwave background temperature angular power spectrum using a χ^2 analysis. We demonstrate the predictive power of dark matter and show its drastic improvement to the fit to data.

Contents

Abstract	i
List of Figures	1
1 Introduction	5
2 Inflation	7
2.1 History	7
2.2 Horizon problem	9
2.3 Flatness problem	11
2.4 Inflation	12
2.4.1 Definitions and Conditions	12
2.4.2 Scalar Fields	13
2.4.3 Slow-Roll Inflation	13
2.4.4 Horizon Problem	15
2.4.5 Flatness Problem	15
2.4.6 Bayesian Model Selection	16
3 Cosmic Microwave Background	17
3.1 Formation	17
3.2 Detection	19
3.3 Angular Power Spectrum	21
3.4 Likelihoods	22
3.5 CAMB	23
3.6 Parameterisation	24
3.7 Implications	25
4 Bayesian Evidence and Model Selection	27
4.1 Bayesian Evidence	27
4.1.1 Theory	27
4.1.2 Calculation	28
4.2 Inflationary Model Selection	29
4.3 Models	29
4.4 Set-up	29
4.5 Results and Discussion	31
4.5.1 Instant reheating	31
4.5.2 Non-instant reheating	32
4.5.3 Adding the BK14 likelihood	36
4.5.4 Inflection Point Inflation	40

5 Understanding the Need for Dark Matter	43
5.1 Algorithms	44
5.1.1 Metropolis-Hastings	44
5.1.2 BOBYQA	44
5.2 Methodology	45
5.3 Minimal Dark Matter	46
5.3.1 Example	46
5.3.2 Lensing + TEB	49
5.3.3 Fixed H ₀ + Lensing + TEB	51
5.4 Discussion	53
6 Conclusions	61
7 Bibliography	63
References	63
8 Appendix	67
8.1 CMB blackbody spectrum	67
8.2 Last Scattering Surface	68
8.3 Angular Size of Largest Fluctuation	69
8.4 First Evidence Calculation	69
8.5 Typical Parameter File	74
8.6 Making Triangle Plots	77

List of Figures

2.1	Radial Velocity-Distance Relation among Extra-Galactic Nebulae.	7
2.2	Cosmic microwave background as seen by Planck	8
2.3	CMB blackbody spectrum	8
2.4	Spacetime diagram illustrating the horizon problem	10
2.5	Spacetime diagram with inflationary phase	16
3.1	Photon Visibility Function	18
3.2	Frequency bands used	20
3.3	CMB Angular Power Spectrum; the bottom plot shows the residuals.	21
3.4	Changing $\ln(10^{10}A_s)$	24
3.5	Changing n_s	25
3.6	$\Delta\phi$ against Ω_K	26
4.1	$V(\phi) = \lambda\phi$ with instant reheating	31
4.2	Testing the sensitivity of the reheating energy density for the quartic potential .	33
4.3	Testing the sensitivity of the reheating energy density for the quadratic potential	34
4.4	Testing the sensitivity of the energy density assumption for the linear potential .	35
4.5	Comparing between two different priors for λ in the quartic potential with the BK14 likelihood	37
4.6	Comparing between two different priors for m^2 in the quadratic potential with the BK14 likelihood	38
4.7	Comparing between two different priors for λ in the linear potential with the BK14 likelihood	39
4.8	Comparing between priors for M in the inflection point inflation model; blue corresponds to a); red corresponds to b)	41
5.1	Comparing $\Omega_c h^2 = 0.00005$ and Planck best fit power spectrum for no lensing .	48
5.2	Triangle plot for $\Omega_c h^2 = 0.00005$ and no lensing	48
5.3	Comparing $\Omega_c h^2 = 0.00005$ and Planck best fit power spectrum for lensing . .	49
5.4	Triangle plot for $\Omega_c h^2 = 0.00005$ and lensing and lowl TEB likelihood . . .	50
5.5	Comparing $\Omega_c h^2 = 0.00005$ and Planck best fit power spectrum for lensing . .	51
5.6	Triangle plot for $\Omega_c h^2 = 0.00005$ and lensing and lowl TEB likelihood with fixed H_0	52
5.7	Comparing all the angular power spectra	53
5.8	Changing $\Omega_b h^2$	54
5.9	Changing H_0	55
5.10	Changing H_0 for the case of lensing + High- l TT and low- l TEB	56
5.11	Fixed H_0 + Lensing + High- l TT and low- l TEB; changing $\Omega_b h^2$	57
5.12	Fixed H_0 + Lensing + High- l TT and low- l TEB; changing curvature Ω_k . . .	58
5.13	Comparing the change in parameters needed for the best fit	58
5.14	Comparing all the angular power spectra for $l \leq 20$	59

Acknowledgements

I used to have McDonald's Filet-o-Fish often as a kid. I would eat the buns first and then have the fish last. An amused friend pointed the oddity out to me, and a nearby teacher commented that it is because I 'save the best for last'. I still possess that trait, but I am learning the value of writing out the most germane things first, to emphasise their significance. In light of this...

Firstly and most importantly, I would like to thank my supervisor, Richard Easterer. I can be a slow person at times, so thank you for your endless patience and dedication to making sure that my experiences this year have been fruitful and manageable. You are one of the busiest people I know, yet you find the time to write references for me and reply to my emails at 12am in the morning when I hit trouble! I am grateful for all the pieces of advice you have bestowed upon me. I will continue working hard every day to make sure your expectations are not displaced.

Thanks to JJ Eldridge for being supportive of my progress, ever since I approached you back in high school about astrophysics research. Likewise, thanks to Grant Christie for continuously encouraging me to pursue astrophysics ever since I joined the Auckland Astronomical Society in 2011, even if it took me awhile to start on research. Thanks to Fiona Panther for advice on being a better student and always believing that I can do things.

I would like to thank the support staff at NeSI, especially Albert Savary, for their persistence in helping me get my suite of code working. It was definitely a long process!

Thanks to Nathan Musoke and Shaun Hotchkiss for comments and insights particularly in cosmology. I am also grateful to be a part of the department's Astronomy Journal Club, and the cosmology group's lunch seminar and afternoon tea, for providing undergraduates and I the opportunity to keep up with the latest research in astrophysics and cosmology.

Thanks to my parents Kristy Ho and Che Ng for supporting me and making my life easier, even though they are all the way in sunny Nelson.

Thanks to my ex for at least strengthening my mental fortitude; much needed for the final push this semester.

Thanks to Samantha Lees, Chooi-An Khoo, Nicola Gujer, and Rochelle Koh especially for making sure that I am mentally functional most of the time.

Thanks to Maria Rodrigues, Lucy Mo, Tama Ngahere, and Angela Asekona, the Department administration team, as well as the janitors for making our lives easier and letting us focus on our studies by providing us with a conducive environment for doing so.

Thanks to the crew in the Honours Room, especially Utsav Patel for being there whenever I needed help academically. Toby Bi, Alex Elliott, Nickolas Morton, Jacob Ngaha, Georgia Nixon, and Katya Zossimova, thanks to you all for the pleasant distractions (no sarcasm) whenever it felt like things got too difficult, and also for tolerating my incessant rants.

Thanks to my flatmates, Angela Tang and Miles Langdon, for being incredibly patient with me while I learn how to be an adult.

Chapter 1

Introduction

Observations of the cosmic microwave background (CMB) allow us to perform cosmological parameter estimation and put constraints on inflationary models. In this dissertation we look at two facets of cosmology, model selection applied to inflationary models, and quantifying the ‘need’ for dark matter in explaining the CMB (temperature) angular power spectrum.

We are interested in using model selection to discriminate between different inflationary models. In particular, we perform evidence calculations with a new model, the inflection point inflation model, which has not been done before. We also extend `ModeCode`, the inflationary perturbation equation solver, to include the inflection point inflation model for the evidence calculations. We recover the broad conclusions from the 2015 Planck analysis for the other inflationary models. Additionally, we explore the impacts of different likelihood combinations and reheating scenarios.

We also demonstrate the necessity of dark matter in explaining the CMB angular power spectrum and quantify, with a χ^2 analysis, the extent to which dark matter impacts the cosmological best fit. In this way, we ascribe a probability to how a dark matter-less universe can explain current measurements of the CMB compared to when dark matter is included in the mix. The physical implications of this are well-known and well-understood, but the quantitative analysis we perform has not been done before.

We start with a review of inflation in Chapter 2 and introduce model selection for the project. In Chapter 3 we review the CMB and the angular power spectrum. We report our evidence calculations and triangle plots in Chapter 4 for various inflationary models, likelihood combinations and physical scenarios. In Chapter 5, we demonstrate the extent to which dark matter is necessary to explain the current measurements of the CMB angular power spectrum. Finally in Chapter 6 we conclude the dissertation.

Chapter 2

Inflation

2.1 History

Cosmology, in part, attempts to provide an answer to the age-old questions - where did we come from? How did everything come to be? Efforts started with the work of Edwin Hubble in 1923 (A. Guth, 1997). Using the 2.5m Hooker telescope atop Mt. Wilson in California, Hubble used a Cepheid variable in the Andromeda Galaxy ('nebula' back then) to show that our Milky Way galaxy is not all there is in the universe. Hubble then, with his assistant Milton Humason in 1928, made observations of Cepheids in 24 other galaxies and inferred the distances to those galaxies. In combination with the redshifts determined by Slipher, Hubble inferred the redshift-distance relation (Hubble, 1929).

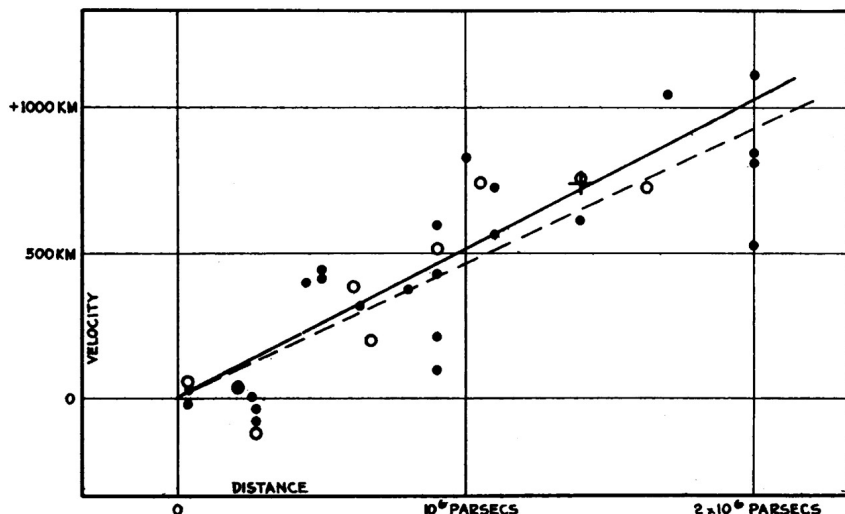


Figure 2.1: Radial Velocity-Distance Relation among Extra-Galactic Nebulae.

Hubble's observations showed that galaxies further away are receding from us at faster speeds. This led to the paradigm-changing idea of the expansion of the universe, and gave rise to the development of the Big Bang theory. Over the forthcoming three decades, key players such as Georges Lemaître, Ralph Alpher, Robert Herman, and George Gamow polished the Big Bang theory.

In 1965, Arno Penzias and Robert Wilson of Bell Laboratories detected the cosmic microwave background (CMB) radiation. This is remnant radiation leftover from the Big Bang. This

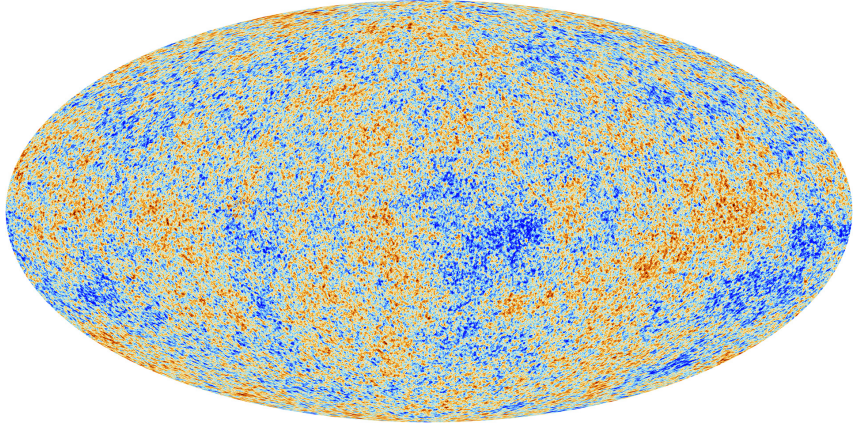


Figure 2.2: Cosmic microwave background as seen by Planck

radiation is a result of the recombination of electrons and nuclei, which decreased the scattering rate of photons, allowing them to propagate freely throughout the universe. This occurred around 380,000 years after the Big Bang, when the temperature was about 3000K (corresponds to visible wavelengths). It is worth noting that recombination did not occur at a single instant of time, but over an interval of 100,000 years. We expand on this in Section 3.1. Cosmological expansion redshifted the radiation to wavelengths in the microwave region of the electromagnetic spectrum today. The best map we have of the CMB¹ (Fig. 2.2) to date is provided by the Planck satellite (described later):

The Big Bang theory predicts that the CMB spectrum is a blackbody spectrum. This was confirmed (Fixsen et al., 1996) by the Far Infra-Red Absolute Spectrophotometer (FIRAS) instrument on the Cosmic Background Explorer (COBE) instrument in the 1990s. Below is the blackbody spectrum observed by COBE - this was plotted in Python using the code provided in Section 8.1 and data from (Fixsen et al., 1996).

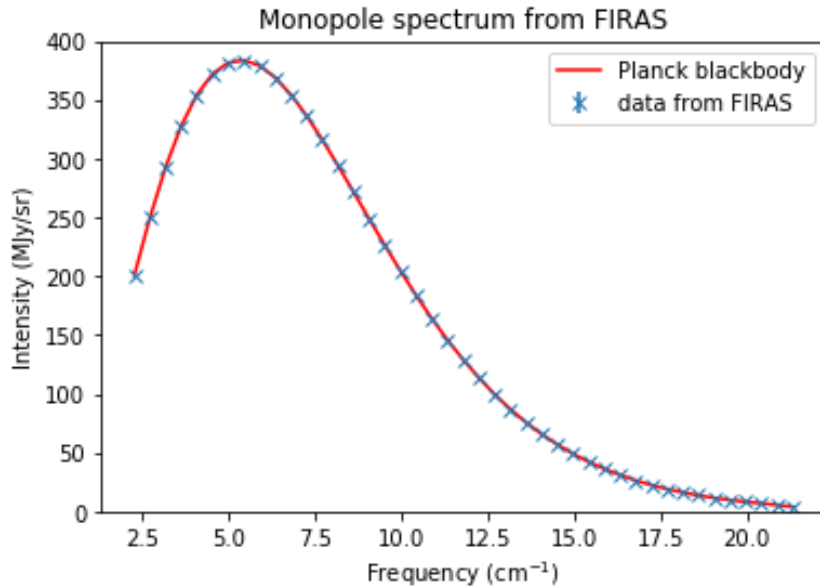


Figure 2.3: CMB blackbody spectrum

¹http://www.esa.int/spaceinimages/Images/2013/03/Planck_CMB

The CMB map (Fig. 2.2) shows temperature fluctuations in the sky on the order of 1 part in 100,000, which indicates incredible uniformity. An obvious question arises: how did the universe get to be so smooth? A logical follow-on question would be to ask: if the universe is *that* smooth, why is it not perfectly smooth? This brings up two puzzles, the horizon problem, and the flatness problem.

2.2 Horizon problem

Let us first obtain an expression for the Hubble parameter H as a function of the redshift z . We start with the first Friedmann equation

$$\left(\frac{\dot{a}}{a}\right)^2 = \frac{8\pi G}{3}\rho - \frac{k}{a^2}. \quad (2.1)$$

The scale factor is a - it parameterises the expansion of the universe. In what follows, we will assume a flat universe, i.e. $k = 0$. Now, let us suppose that the density of the universe comprises $\rho = \rho_M + \rho_R + \rho_\Lambda$, for matter, radiation and the cosmological constant respectively. We also have

$$\Omega_M = \frac{\rho_M}{\rho_c} \quad ; \quad \Omega_R = \frac{\rho_R}{\rho_c} \quad ; \quad \Omega_\Lambda = \frac{\rho_\Lambda}{\rho_c}, \quad (2.2)$$

where

$$\rho_c = \frac{3H_0^2}{8\pi G}$$

is the critical density today; so $\Omega_M + \Omega_R + \Omega_\Lambda = 1$. Now, since we know

$$\rho_M \propto \frac{1}{a^3}$$

and

$$\rho_R \propto \frac{1}{a^4},$$

and taking $a_0 = 1$ for today,

$$\begin{aligned} \left(\frac{\dot{a}}{a}\right)^2 &= H^2 = \frac{8\pi G}{3}\rho_c \left(\frac{\Omega_M}{a^3} + \frac{\Omega_R}{a^4} + \Omega_\Lambda \right) \\ &= \frac{8\pi G}{3} \frac{3H_0^2}{8\pi G} \left(\frac{\Omega_M}{a^3} + \frac{\Omega_R}{a^4} + \Omega_\Lambda \right) \\ &= H_0^2 \left(\frac{\Omega_M}{a^3} + \frac{\Omega_R}{a^4} + \Omega_\Lambda \right). \end{aligned}$$

Since

$$a = \frac{1}{1+z},$$

we finally get

$$H(z) = H_0 \sqrt{\Omega_M(1+z)^3 + \Omega_R(1+z)^4 + \Omega_\Lambda}. \quad (2.3)$$

In a matter-dominated universe (just after CMB is released), we can write $H(z) \approx H_0(1+z)^{\frac{3}{2}}$.

We also introduce the notion of the particle horizon. This quantity ascribes a sense of ‘physical distance’ in space. It is simply the maximum distance that light can travel over the concurrent age of the universe. This distance, the comoving redshift-distance relation, is given by

$$d = \frac{c}{a_0} \int \frac{1}{H(z)} dz \approx \frac{c}{a_0 H_0} \int_0^z (1+z')^{-\frac{3}{2}} dz' \quad (2.4)$$

where c is the speed of light; a_0 is the scale factor at some given time; H_0 is the Hubble parameter at some given time; $H(z)$ is the Hubble parameter at some specified redshift z .

Integrating, we get

$$d_H = \frac{2c}{a_0 H_0} \left(1 - \frac{1}{(1+z)^{\frac{1}{2}}} \right), \quad (2.5)$$

so the particle horizon at current time is

$$d_H = \frac{2c}{a_0 H_0},$$

i.e. take $z \rightarrow \infty$. The angle subtended is

$$\theta = \frac{x}{d_H} = x \frac{a_0 H_0}{2c}.$$

The particle horizon *at* the time of last scattering (elaborated below) is

$$d = \frac{c}{a_0 H_0} \int_{z_{\text{LS}}}^{\infty} (1+z')^{-\frac{3}{2}} dz' = \frac{2c}{a_0 H_0} \frac{1}{\sqrt{1+z_{\text{LS}}}}, \quad (2.6)$$

So the angle subtended by the particle horizon at last scattering is

$$\theta = \frac{a_0 H_0}{2c} \times \frac{2c}{a_0 H_0} \frac{1}{\sqrt{1+z_{\text{LS}}}} = \frac{1}{\sqrt{1+z_{\text{LS}}}}.$$

We know that $z_{\text{LS}} \approx 1100$ (Takahashi et al., 2017), which corresponds to $\theta = 0.03 \text{ rad} = 1.7^\circ$.

This tells us that regions in the sky separated by scales larger than 1.7° should not be causally connected. However, as we have noted above, the CMB is uniform (isotropy). Conventional Big Bang theory cannot explain this apparent connectedness of seemingly disconnected regions of the sky. There is no conventional possibility that these regions could have ever interacted and thermally equilibrated, which is what the CMB observations imply.

The horizon problem is illustrated through a spacetime diagram (Baumann, 2014) below

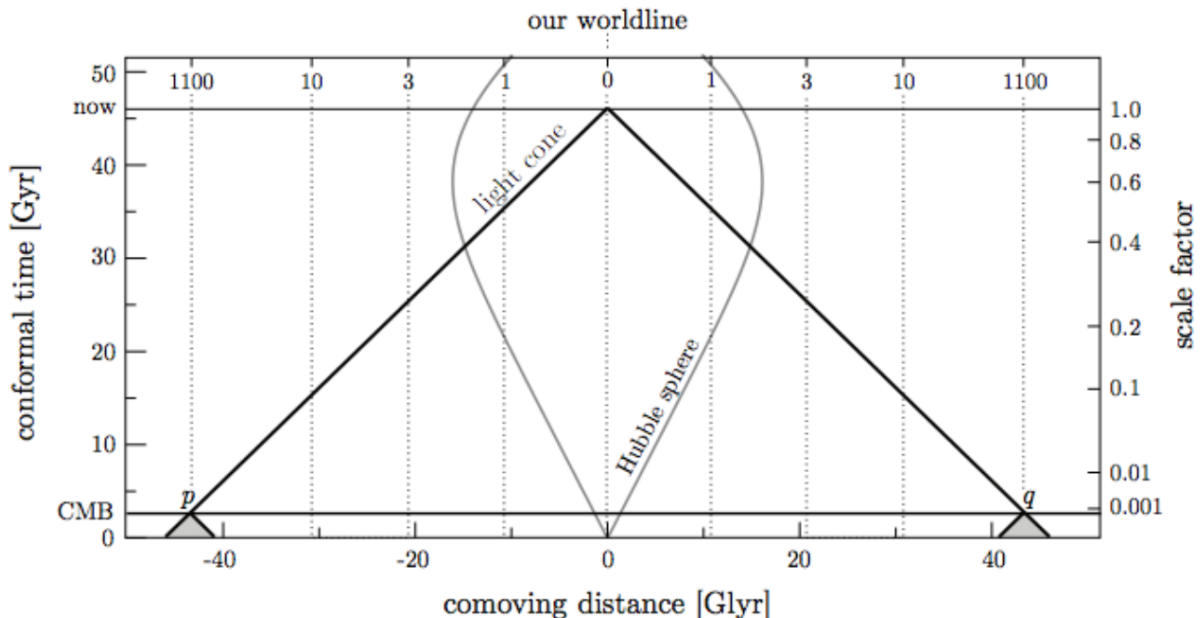


Figure 2.4: Spacetime diagram illustrating the horizon problem

where the conformal time is defined as

$$\tau = \int_0^t \frac{dt'}{a(t')},$$

which is simply the particle horizon divided by c , the speed of light. The Hubble sphere describes the observable universe. Let us look at any two points on the CMB, p and q , and trace them on the spacetime diagram. We see from their past light cones that in the early universe, the two points were acausal, i.e. under conventional Big Bang theory, they would not have interacted.

2.3 Flatness problem

Let us now look at the Friedmann equation 2.1. If we write the critical density as

$$\rho_c = \frac{3H^2}{8\pi G},$$

we can rearrange Eq. 2.1 to get

$$\begin{aligned} \frac{3H^2}{8\pi G\rho} &= 1 - \frac{3}{8\pi G\rho} \frac{k}{a^2} \\ \implies (\Omega^{-1} - 1)\rho a^2 &= -\frac{3k}{8\pi G} = \text{constant}, \end{aligned} \quad (2.7)$$

where

$$\Omega = \frac{\rho}{\rho_c},$$

i.e. the quantity stays constant over time. So we have

$$(\Omega_0^{-1} - 1)\rho_0 a_0^2 = (\Omega^{-1} - 1)\rho a^2,$$

which yields

$$\Omega^{-1} - 1 = (\Omega_0^{-1} - 1) \frac{\rho_0}{\rho} \left(\frac{a_0}{a} \right)^2 \quad (2.8)$$

We consider matter-radiation equality, where $\rho_M = \rho_R$. From Paper XIII of (Planck Collaboration, Ade, P. A. R., et al., 2016), $z_{\text{eq}} = 3371$. We use $\rho = \rho_0(1+z)^4$. Also,

$$a = \frac{a_0}{1+z};$$

then substituting into Eq. 2.8, we get

$$\Omega^{-1} - 1 = \frac{\Omega_0^{-1} - 1}{(1+z)^2}. \quad (2.9)$$

We know that from Paper XIII of (Planck Collaboration, Ade, P. A. R., et al., 2016) $|\Omega_K| < 0.005$. Now, as $\Omega_0 = 1 - \Omega_K$, we have that $0.995 < \Omega_0 < 1.005$, the present value of the total density. This means that at matter-radiation equality, $0.9999999996 < \Omega < 1.0000000004$ - the universe must have been extraordinarily flat. This is even more striking at times on the order of 10^{-36} s, when cosmological inflation was purported to take place, where $|\Omega_K| \lesssim 10^{-61}$ (Baumann, 2009). The conventional Big Bang theory does not propose a mechanism that results in such a fine-tuned initial condition of the universe. This is the flatness problem.

2.4 Inflation

2.4.1 Definitions and Conditions

In the early 1980s, Alan Guth, then at Stanford University, proposed a solution (A. H. Guth, 1981) to the horizon problem and flatness problem and also addressed other issues such as the monopole problem (beyond intended scope of the dissertation). Guth posited the idea of inflation, a period of rapid expansion of space in the very early universe from 10^{-35} s to about 10^{-32} s, with the exact details depending on the energy scale at which inflation takes place.

Inflation is not meant to supplant the Big Bang itself, but supplements the successful aspects of the Big Bang theory. The Big Bang accounts for the relative abundance of primordial elements, such as helium and hydrogen (and their isotopes).

By definition, inflation is any epoch where the growth of the size of the universe, is accelerating:

$$\frac{d^2a(t)}{dt^2} > 0.$$

An alternative condition of inflation is that the Hubble length decreases, i.e.

$$\frac{d}{dt} \frac{1}{aH} < 0.$$

The Hubble length tells us about the size of the observable universe at any given point in time. This will be elaborated upon further below when we discuss how inflation solves the horizon problem. Using the Friedmann equation 2.1 and the continuity equation

$$\dot{\rho} + 3\frac{\dot{a}}{a}(\rho + P) = 0, \quad (2.10)$$

we derive (using $k = 0$)

$$\begin{aligned} \frac{d}{dt} \left(\frac{\dot{a}}{a} \right)^2 &= \frac{8\pi G}{3} \dot{\rho} \\ 2\frac{\dot{a}}{a} \left[\frac{\ddot{a}}{a} - \frac{\dot{a}^2}{a^2} \right] &= \frac{8\pi G}{3} \dot{\rho} \\ \frac{\ddot{a}}{a} - \frac{\dot{a}^2}{a^2} &= \frac{4\pi G}{3} \dot{\rho} \left(\frac{\dot{a}}{a} \right)^{-1} \\ &= -4\pi G(\rho + P); \\ \frac{\ddot{a}}{a} &= -4\pi G(\rho + P) + \left(\frac{\dot{a}}{a} \right)^2 \\ &= -4\pi G(\rho + P) + \frac{8\pi G}{3} \rho \\ &= -\frac{4\pi G}{3}(\rho + 3P). \end{aligned}$$

Since we require $\ddot{a} > 0$ (and $a(t) > 0$), we want

$$\rho + 3P < 0 \implies P < -\frac{\rho}{3},$$

i.e. we require negative pressure (ρ is a positive quantity).

2.4.2 Scalar Fields

The negative pressure is typically provided by a scalar field. A scalar field describes scalar (spin-0) particles and has an associated potential energy. In inflation, these scalar fields are known as inflatons. One possible inflaton is the Higgs field - ongoing research is being carried out to determine whether the Higgs inflaton can explain the dynamics of inflation (Bezrukov, 2013), although this would not be the case for the Standard Model Higgs.

The potential energy of the inflaton may redshift extremely slowly with the expansion of the universe in the early universe - this is associated with an effective equation of state with a negative pressure.

The energy density and pressure for a homogeneous scalar field $\phi = \phi(t)$ is

$$\rho = \frac{1}{2}\dot{\phi}^2 + V(\phi), \quad (2.11)$$

$$P = \frac{1}{2}\dot{\phi}^2 - V(\phi), \quad (2.12)$$

with $V(\phi)$ being the associated scalar field potential. We will soon discuss different inflationary models where we specify different forms for the inflaton potentials.

Rewriting the Friedmann equation using the reduced Planck mass $M_{Pl} = 2.43 \times 10^{18}$ GeV, we have (with $k = 0$)

$$H^2 = \left(\frac{\dot{a}}{a}\right)^2 = \frac{\rho}{3M_{Pl}^2}$$

where H is the Hubble parameter. Now, along with Eq. 2.11, we get

$$H^2 = \frac{1}{3M_{Pl}^2} \left[\frac{1}{2}\dot{\phi}^2 + V(\phi) \right]. \quad (2.13)$$

Next, substituting the time derivatives of Eq. 2.11 and Eq. 2.12 into Eq. 2.10, we obtain

$$\begin{aligned} \dot{\rho} + 3\frac{\dot{a}}{a}(\rho + P) &= 0 \\ \dot{\phi}\ddot{\phi} + \dot{\phi}\frac{dV}{d\phi} + 3H\dot{\phi}^2 &= 0 \\ \ddot{\phi} + 3H\dot{\phi} &= -\frac{dV}{d\phi}, \end{aligned}$$

which is the Klein-Gordon equation, the equation of motion describing the evolution of a scalar field (an inflaton in particular).

At the end of inflation, there are two general scenarios that could have taken place: either all of the potential energy of the inflation field instantaneously decayed into relativistic Standard Model particles (instant reheating), or that this reheating process occurred over a long, gradual timescale (Easther, Flauger, & Gilmore, 2011). For this project, we adopt the latter reheating scenario. This will be elaborated upon in Chapter 4.

2.4.3 Slow-Roll Inflation

When analysing inflationary models, we employ the slow-roll approximation, which posits that

$$\dot{\phi}^2 \ll V(\phi),$$

i.e. the kinetic term is negligible. From (2.13) then, we have

$$H^2 \simeq \frac{V(\phi)}{3M_{Pl}^2},$$

and the Klein-Gordon equation becomes

$$3H\dot{\phi} \simeq -\frac{dV}{d\phi}$$

as $\ddot{\phi} \ll 1$.

In order for these approximations to be hold, the slow-roll conditions have to be satisfied, these are

$$\epsilon(\phi) \ll 1, \quad (2.14)$$

$$|\eta(\phi)| \ll 1; \quad (2.15)$$

the slow-roll parameters are defined as

$$\epsilon(\phi) = \frac{M_{Pl}^2}{2} \left(\frac{V'}{V} \right)^2, \quad (2.16)$$

$$\eta(\phi) = M_{Pl}^2 \frac{V''}{V}, \quad (2.17)$$

where the primes denote derivatives with respect to the inflaton.

For the sake of illustration, say for instance we have

$$V(\phi) = \frac{1}{2}m^2\phi^2,$$

then with

$$V'(\phi) = m^2\phi,$$

the slow-roll conditions (2.14) and (2.15) dictate that

$$\phi^2 \gg 2M_{Pl}^2.$$

As long as the slow-roll conditions are satisfied, inflation will proceed until the inflaton approaches the minimum (i.e. kinetic energy is no longer negligible) at which point inflation stops (i.e. when $\epsilon = 1$).

We can quantify the amount of inflation with the number of e-folds, i.e.

$$N(t) \equiv \ln \left(\frac{a(t_{\text{end}})}{a(t)} \right),$$

where $N(t)$ describes how much inflation occurred from time t until t_{end} , the time at the end of

inflation. We can express this as

$$N(t) = \ln \frac{a(t_{\text{end}})}{a(t)} \quad (2.18)$$

$$= [\ln(a(t'))]_t^{t_{\text{end}}} \quad (2.19)$$

$$= \int_t^{t_{\text{end}}} \frac{\dot{a}}{a} dt' \quad (2.20)$$

$$= \int_t^{t_{\text{end}}} H dt' \quad (2.21)$$

$$= \int_{\phi}^{\phi_{\text{end}}} H \frac{dt'}{d\phi'} d\phi' \quad (2.22)$$

$$\simeq - \int_{\phi}^{\phi_{\text{end}}} H \frac{3H}{\left(\frac{dV}{d\phi}\right)} d\phi' \quad (2.23)$$

$$= \int_{\phi_{\text{end}}}^{\phi} 3H^2 \frac{1}{V'} d\phi' \quad (2.24)$$

$$\simeq \frac{1}{M_{\text{Pl}}^2} \int_{\phi_{\text{end}}}^{\phi} \frac{V}{V'} d\phi'. \quad (2.25)$$

For example, in the canonical case $V = m^2 \phi^2 / 2$,

$$N(t) = \frac{1}{M_{\text{Pl}}^2} \int_{\phi_{\text{end}}}^{\phi} \frac{\phi'}{2} d\phi' = \frac{1}{2M_{\text{Pl}}^2} \left[\frac{\phi^2}{2} - \frac{\phi_{\text{end}}^2}{2} \right].$$

In order to solve the horizon problem (below), inflation predicts that there should be 60 e-folds of expansion.

2.4.4 Horizon Problem

The horizon problem is solved by inflation. We illustrate the solution using this spacetime diagram (Baumann, 2014) in Fig. 2.5. This is equivalent to Fig. 2.4, with the inflationary picture incorporated. As mentioned above, one of the conditions of inflation is that the Hubble length, $1/aH$, decreases. This is illustrated in the diagram as the two converging light grey lines moving upwards in the diagram towards the ‘bottleneck’.

Recall that the Hubble length tells us about the distance that some given particle can travel over one expansion time $1/H$. Now consider again the two arbitrary points in the CMB, and with the inflationary picture in mind, trace their past light cones. The two disparate CMB points were, during inflation, able to be in causal contact with each other as they were within the Hubble radius at that time. Thus the two points were able to interact with each other and be in thermal equilibrium. After inflation, the universe undergone its conventional growth in size to the current universe. This explains why the universe is so homogeneous - points in the CMB which are acausal today, were in causal contact in the very early universe.

2.4.5 Flatness Problem

As mentioned above, inflation solves the flatness problem. We see how this is the case. Earlier on, we derived Eq. 2.7,

$$(\Omega^{-1} - 1)\rho a^2 = -\frac{3k}{8\pi G} \in \mathbb{R}.$$

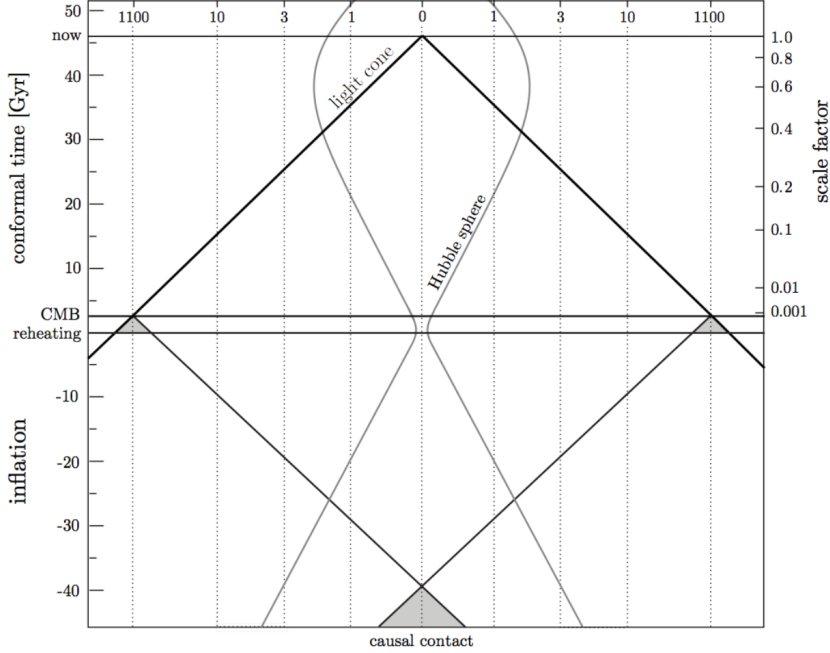


Figure 2.5: Spacetime diagram with inflationary phase

Inflation posits that the universe undergoes rapid expansion, i.e. that a grows exponentially. During inflation, ρ is roughly constant. This means that the quantity ρa^2 is growing extremely quickly. Since the right hand side is constant as all the quantities are constants, this means that whatever the initial value of $(\Omega^{-1} - 1)$, it will be very close to 0 at the end of inflation, i.e. Ω is very close to 1. In fact, it will be around 10^{-61} , the value quoted in Section 2.3. This means that inflation drives Ω to 1; inflation drives the universe to flatness. After inflation, this quantity (parameterised by Ω_K) could increase to its present value of around 0.005 (Planck Collaboration, Ade, P. A. R., et al., 2016). This solves the flatness problem.

2.4.6 Bayesian Model Selection

We will discuss this in greater detail in Chapter 4, but let us first summarise the aim. We wish to be able to quantitatively compare different inflationary models. Specifically, we would like to discuss how likely any one inflationary model is able to explain the current observations over another model. To do this, we employ Bayesian model selection. We make use of a quantity, the ratio of Bayesian evidences (model-averaged likelihood) to tell us the relative betting odds of the models being able to explain the current universe.

To specify any inflationary model (Easter & Peiris, 2012), one needs to put forward an inflaton potential. For this project, we have mainly considered inflationary potentials of monomial form, i.e.

$$V(\phi) = \lambda \frac{\phi^n}{n}.$$

We look at the cases where $n = 2/3, 1, 2, 4$. We will also look at the novel inflection point inflation model. We also have to specify the priors (initial probability) for post-inflationary parameters, such as τ , the optical depth, and the baryonic matter content, $\Omega_b h^2$.

Chapter 3

Cosmic Microwave Background

The cosmic microwave background (CMB) is relic radiation from the early Universe. We will discuss below how this relates to the reheating phase just after inflation, and also the recombination phase that ended around 380,000 years after the Big Bang. In this chapter, we go into more detail about the formation of the CMB, how it is detected, and the analysis tools that we employed to study the CMB. It is by studying the CMB that we can understand many of the nuances of the Big Bang theory, and it even tells us something about the composition of the universe. In particular, to explain the CMB, dark matter is required in the recipe. We will discuss this in Chapter 5.

3.1 Formation

In the previous chapter, we posited that inflation was driven by some scalar field that we call the inflaton. In talking about the CMB, we asked the following: why is the universe not perfectly smooth? This can be answered by invoking quantum fluctuations of the inflaton (Liddle & Lyth, 2000). During inflation, these quantum fluctuations were stretched to large macroscopic sizes, much larger than the Hubble scale, that is they were outside the particle horizon (i.e. outside causality), thus unable to evolve and were ‘frozen-in’. When inflation ended, the Hubble length increased again (expansion of universe) and these ‘frozen-in’ quantum fluctuations re-entered the particle horizon. These became the seeds for structure formation (i.e. CMB anisotropy). We look briefly into the details of how this structure formation came about.

After the reheating phase of the post-inflationary universe where the inflaton decayed into Standard Model particles, the universe entered the electroweak epoch (Liddle & Lyth, 2000) which contained quarks, anti-quarks and gluons, mediators of the strong nuclear force. As the universe expanded and cooled, quarks were bound into hadrons ($10^{-12} - 1$ s), neutrinos decoupled from baryonic matter (1 s), and nucleons formed atomic nuclei (mainly hydrogen and helium-4; $10 - 1000$ s). At this stage we get a plasma ‘soup’ of photons and baryons which is referred to as the photon-baryon fluid.

About 380,000 years after the Big Bang, the temperature was roughly 3000 K. The universe cooled enough to the stage where electrons could combine with atomic nuclei to form atoms. At this point, the photons decoupled from the matter and were no longer in thermal equilibrium with matter. The photons then propagated freely throughout the universe. The Universe became transparent.

We noted above that recombination was not instantaneous. We can illustrate this through the photon visibility function in Fig. 3.1, which tells us about the probability that any given photon

was last scattered for some redshift interval. We can approximate the photon visibility function (Jones & Wyse, 1985) by

$$p(z) = e^{-\tau} \frac{d\tau}{dz} = 5.26 \times 10^{-3} \left(\frac{z}{1000} \right)^{13.25} e^{-0.37 \left(\frac{z}{1000} \right)^{14.25}}.$$

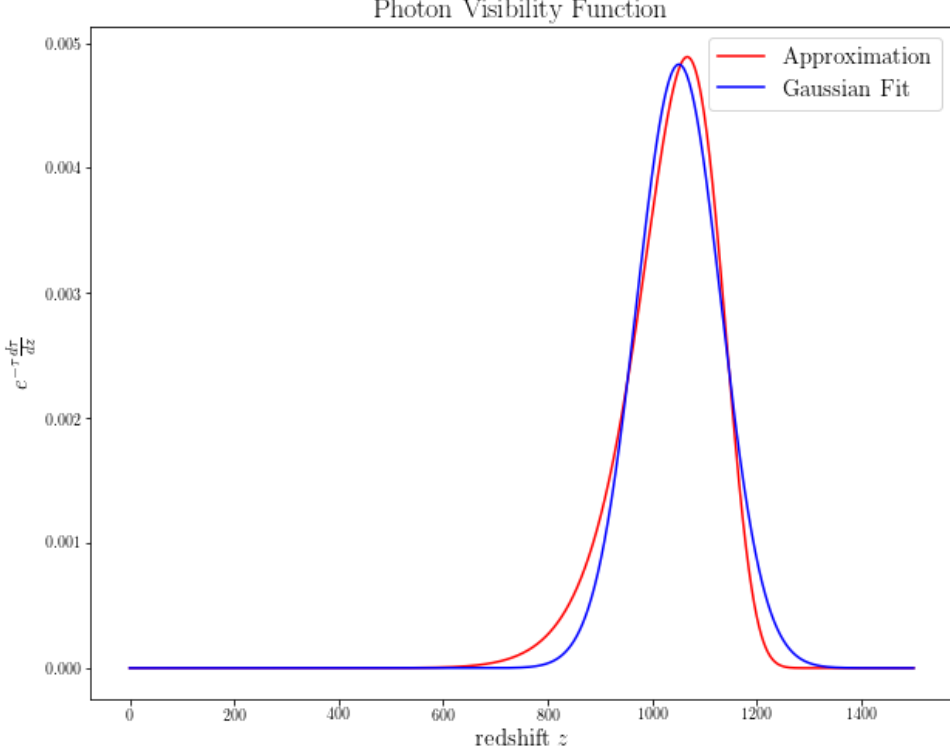


Figure 3.1: Photon Visibility Function

In cosmological parlance, this is referred to as the ‘surface of last scattering’. It is only towards the end of this recombination phase where the mean free path of most photons approached the current age of the universe (multiplied by the speed of light). Using the **Python** non-linear curve-fitting function `scipy.optimize.curve_fit`, we can approximate this photon visibility function (PVF) via a Gaussian. We then get that the PVF peaks at

$$z = 1050.73 \pm 0.11,$$

and has a width of

$$\sigma_z = 80.60 \pm 0.11.$$

To get a first approximation to the corresponding number of years, we use Eq. (2.3) and assume $\Omega_M \approx 1$ (matter-dominated), so

$$H(z) = H_0(1+z)^{\frac{3}{2}},$$

then

$$\frac{\dot{a}}{a} = H_0 a^{-\frac{3}{2}} \quad (3.1)$$

$$\sqrt{a} \frac{da}{dt} = H_0 \quad (3.2)$$

$$\int_0^a \sqrt{a'} da' = \int_0^t H_0 dt' \quad (3.3)$$

$$\frac{2}{3}a^{\frac{3}{2}} = H_0 t \quad (3.4)$$

$$\therefore t = \frac{2}{3} \frac{a^{\frac{3}{2}}}{H_0} = \frac{2}{3H_0(1+z)^{\frac{3}{2}}}. \quad (3.5)$$

If we have

$$H_0 = 100h \text{ km s}^{-1} \text{ Mpc}^{-1} \approx 3.24 \times 10^{-18} \text{ h s}^{-1},$$

with $c = 3 \times 10^8 \text{ m s}^{-1}$, $1 \text{ pc} = 3.26 \text{ light years}$, and $h = 0.6731 \pm 0.0096$ (Planck Collaboration, Ade, P. A. R., et al., 2016), the time difference between 5% ($z_{5\%} = z + 2\sigma_z = 1211.92 \pm 0.25$) of photons being able to scatter, and 95% of photons being able to scatter ($z_{95\%} = z - 2\sigma_z = 889.54 \pm 0.25$), is

$$\begin{aligned} \Delta t = t_{95\%} - t_{5\%} &= \frac{2}{3H_0} \left[\frac{1}{(1+z_{95\%})^{\frac{3}{2}}} - \frac{1}{(1+z_{5\%})^{\frac{3}{2}}} \right] \\ &\approx (4.26 \pm 0.02) \times 10^{12} \text{ s} = (135200 \pm 600) \text{ years}. \end{aligned}$$

A more careful calculation would take into account the ionization history and the sub-dominant radiation component at the time of recombination.

The error was calculated in **Python** (see Section 8.2) using

$$\sigma_{\Delta t} = \sqrt{\left(\frac{\partial \Delta t}{\partial H_0}\right)^2 \sigma_{H_0}^2 + \left(\frac{\partial \Delta t}{\partial z_1}\right)^2 \sigma_{z_1}^2 + \left(\frac{\partial \Delta t}{\partial z_2}\right)^2 \sigma_{z_2}^2},$$

where

$$\begin{aligned} \frac{\partial \Delta t}{\partial H_0} &= -\frac{2}{3H_0^2} \left[\frac{1}{(1+z_{95\%})^{\frac{3}{2}}} - \frac{1}{(1+z_{5\%})^{\frac{3}{2}}} \right]; \\ \frac{\partial \Delta t}{\partial z_{95\%}} &= -\frac{1}{H_0} \frac{1}{(1+z_{95\%})^{\frac{5}{2}}}; \\ \frac{\partial \Delta t}{\partial z_{5\%}} &= \frac{1}{H_0} \frac{1}{(1+z_{5\%})^{\frac{5}{2}}}. \end{aligned}$$

What we have described above was the primary contribution to the anisotropy of the CMB. There were also secondary contributions to the CMB anisotropy, which occurred between the surface of last scattering and the observer (us). One example of this is the Sunyaev-Zel'dovich effect (Planck Collaboration, Aghanim, et al., 2016b), where the CMB was distorted due to the inverse Compton scattering of CMB photons through collisions with electrons in galactic clusters. Another prominent secondary contribution is attributed to the scattering of the CMB photons by ions that were formed due to their liberation from neutral atoms by ionising radiation. This ionising radiation could have originated from supernovae, or it could be the radiation from young, massive Population III stars. This is an active area of research.

3.2 Detection

The primary and secondary anisotropies described above make up the CMB that we see today. The relic photons, as they traversed through the universe, were also gravitationally lensed by galactic clusters along the line-of-sight. The *Planck* satellite eventually captured some of these photons. *Planck* was launched on 14 May 2009, and was scientifically operational from 12

August 2009 to 23 October 2013 (Planck Collaboration, Adam, Ade, Aghanim, Akrami, et al., 2016). *Planck* represents, to date, the state-of-the-art scientific observatory to probe the CMB to unprecedented resolution and sensitivity.

In order to have achieved the required level of sensitivity to detect the CMB anisotropies, the instruments were cooled down to 0.1 K to minimise thermal noise. For the High Frequency Instrument (HFI), He-3 was needed. For the low-frequency counterpart, the Low Frequency Instrument (LFI), He-4 was used to cool the instrument down to a modest 20 K. The HFI had an array of 54 detectors; light was focussed onto them via 32 feed horns (signal receivers). The HFI collected data from 6 frequency bands (100, 143, 217, 353, 545 and 857 GHz) using bolometers, sensitive thermistors used to detect temperature anisotropies. Since the CMB is currently $T = 2.7255$ K and is uniform to 1 part in 100,000, it was paramount that the instruments were cooled down to low enough temperatures to minimise thermal noise.

The LFI collected data from 3 frequency bands (30, 45, and 70 GHz) using *High Electron Mobility Transistors*, under the instrument horns, which amplified the incoming analog signals and digitised them. Fig. 3.2 below summarises the frequencies covered by *Planck*.

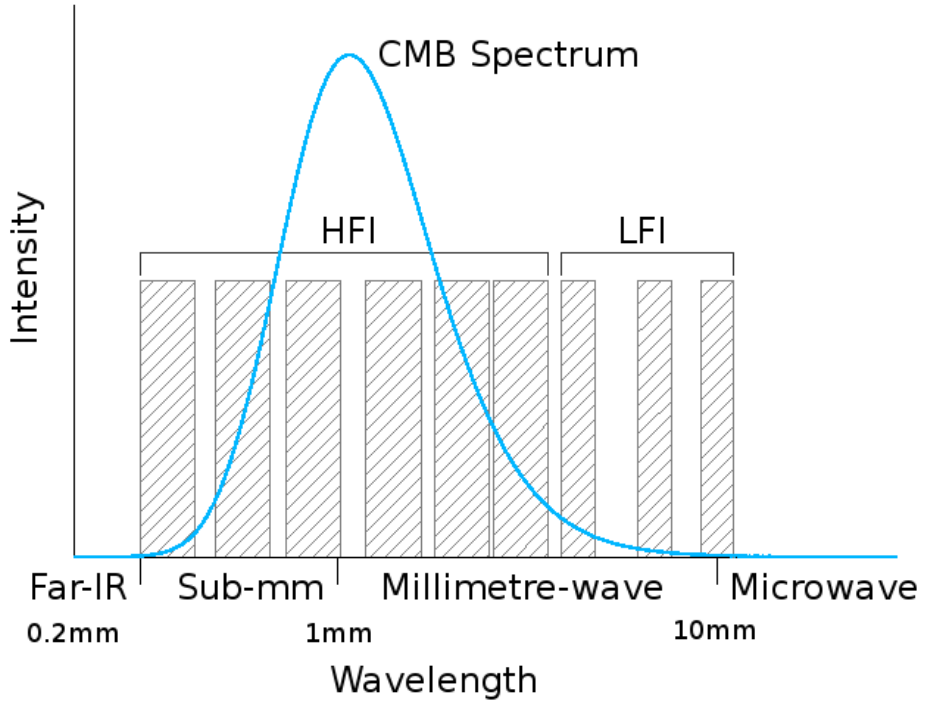


Figure 3.2: Frequency bands used

The *Planck* satellite also carried out measurements of the polarisation of the CMB photons. In inflationary model selection (Chapter 4), these will serve to better constrain r , the ratio of tensor amplitudes to scalar amplitudes.

To produce the CMB map for meaningful interpretation, there is a need to systematically and meticulously extract the CMB signal from the different frequency channels, and to account for the systematic/foreground effects. One such algorithm is SMICA (Cardoso, Le Jeune, De-labrouille, Betoule, & Patanchon, 2008). In a given signal at a given frequency ν in direction θ , it is made up of a linear combination

$$X_\nu(\theta) = X_\nu^{\text{CMB}}(\theta) + X_\nu^{\text{SZ}}(\theta) + \dots + N_\nu(\theta),$$

where X_ν^i is the absolute contribution to the signal due to some component i (e.g. Sunyaev-Zel'dovich or galactic emission); $N_\nu(\theta)$ incorporates instrument noise. The data obtained by *Planck* was first processed in Fourier space, where relative weights for the various source contributions were determined; the end result was a CMB map that was foreground-subtracted and contamination-free (as best as possible). Associated with the map are likelihood codes used in parameter estimation and inflationary model selection. This will be elaborated upon in Section 3.4.

As mentioned above, $T \approx 3000$ K at the time of last scattering. The expansion of the universe caused space, and hence the wavelength of a photon from the CMB, to stretch by about 1100 times, making the CMB cooler as the density fell. The temperature of the CMB is currently measured at $T = 2.7255$ K. The associated wavelength is about 2 mm, i.e. microwaves. The CMB has a nearly ideal blackbody spectrum that peaks at $\nu \approx 160$ GHz. The CMB is nearly uniform, with fluctuations on the order of 1 part in 100,000. These observed anisotropies can be analyzed with a power spectrum.

3.3 Angular Power Spectrum

The CMB angular power spectrum (Planck Collaboration, Aghanim, et al., 2016a) is

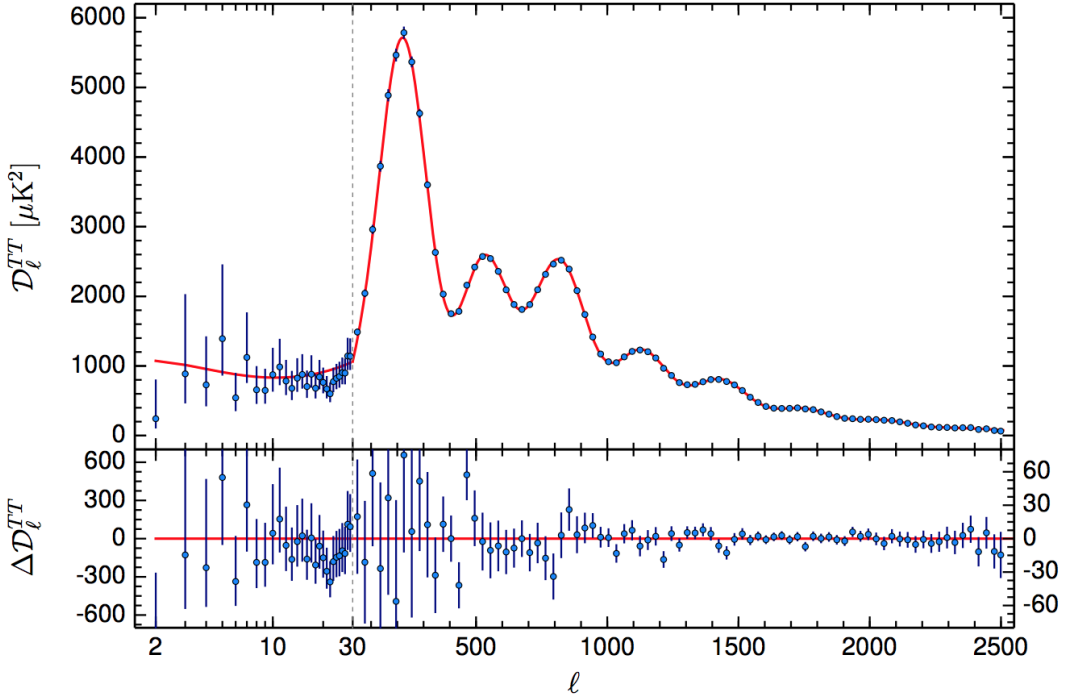


Figure 3.3: CMB Angular Power Spectrum; the bottom plot shows the residuals.

The CMB can be represented with spherical harmonics. They are an orthonormal basis for specifying functions defined on a spherical surface (i.e. sky). In this way, we decompose the CMB into spherical harmonics, and characterise the temperature fluctuations as a function of the angular scale. The temperature fluctuation is defined as

$$\Delta T = \frac{\delta T}{T_{\text{CMB}}},$$

where $\delta T = T - T_{\text{CMB}}$, and T_{CMB} is the average temperature of the CMB. We have $\Delta T = \Delta T(\theta, \phi)$, i.e. the temperature fluctuation is dependent on which direction we look at in the sky. If we work in Fourier space, the temperature fluctuation is defined as

$$\Delta T(\theta, \phi) = \sum_{l=0}^{\infty} \sum_{m=-l}^{m=l} a_{lm} Y_{lm}(\theta, \phi),$$

where

$$a_{lm} = \iint \Delta T(\theta, \phi) Y_{lm}^* d\theta d\phi$$

are the spherical harmonic coefficients Y_{lm} . Since a_{lm} represents the average fluctuation about some mean, we have that $\langle a_{lm} \rangle = 0$. A meaningful quantity is to write the power spectrum of the CMB as

$$C_l = \langle |a_{lm}|^2 \rangle,$$

i.e. correlations in temperature by angular position. By convention, we then plot D_l [in $(\mu K)^2$] as a function of l , the multipole number, where

$$D_l = \frac{l(l+1)}{2\pi} C_l \times T_{\text{CMB}}^2,$$

and we write T_{CMB} in microKelvins.

3.4 Likelihoods

Crudely speaking, the likelihood is the probability of obtaining the data given some model. The cleaning and calibration of these likelihood maps was a heavily involved process for each instrument (Planck Collaboration, Adam, Ade, Aghanim, Arnaud, et al., 2016). We have briefly discussed this above. The interested reader can refer to the papers outlined in the Introduction of the Planck 2015 results paper XI (Planck Collaboration, Aghanim, et al., 2016a). The associated statistics that go into the analysis can be understood from (Tegmark, 1997). We will explicitly mention the likelihoods employed in relation to the results in Chapters 3 and 4.

First we look at the low- l likelihood, which the Planck collaboration define to be $l \leq 29$. This will contain temperature and polarisation information for the large angular scales. The information is expressed in maps of the three Stokes parameters $\{T, Q, U\}$, where T refers to unpolarised intensity and Q, U refer to the linear polarisation state of the CMB photons. After employing a component separation algorithm such as SMICA (described above), one may summarise the information with a data vector (Planck Collaboration, Aghanim, et al., 2016a)

$$\mathbf{m}^X = \mathbf{s}^X + \mathbf{n}^X,$$

where \mathbf{s}^X corresponds to the CMB signal, modelled as a set of statistically isotropic Gaussian random fields. The quantity \mathbf{n} refers to the instrumental noise; X refers to the component - T being temperature, E being the E -mode polarisation (curl-less vector field) and B being the B -mode polarisation (divergence-less vector field).

Autocorrelations and cross-correlations C_l^{AB} for $\text{AB} \in \{TT, EE, BB, TE\}$ are calculated, resulting in the covariance matrix

$$S(C_l) = \sum_{l=2}^{l_{\max}} \sum_{\text{AB}} C_l^{\text{AB}} P_l^{\text{AB}}.$$

P_l^{AB} refers to the instrumental beam-weighted sum over the associated Legendre polynomials. For temperature for example,

$$(P_l^{\text{TT}})_{i,j} = \frac{2l+1}{4\pi} B_l^2 P_l(\hat{\mathbf{n}}_i \cdot \hat{\mathbf{n}}_j),$$

where $\hat{\mathbf{n}}_i$ is a unit vector in the direction of pixel i ; B_l represents the product of the Legendre coefficients (polynomial) corresponding to the instrumental beam, and the pixel windows. This takes into account the (possible) biases introduced due to the finite resolution of the *Planck* instruments (Wehus, Ackerman, Eriksen, & Groeneboom, 2009). See (Tegmark & de Oliveira-Costa, 2001) for the treatment of the polarisation components.

Like the CMB signal, the instrumental noise is modelled to have a Gaussian distribution, with associated covariance matrix N - determined by detector sensitivity among other factors. M is defined to be the full covariance of the data, $M = S + N$. The final likelihood expression then reads

$$\mathcal{L}(C_l) := P(\mathbf{m}|C_l) = \frac{1}{2\pi\sqrt{M}} e^{-\frac{1}{2}\mathbf{m}^T M^{-1} \mathbf{m}},$$

where we note that the conditional probability $P(\mathbf{m}|C_l)$ defines our likelihood $\mathcal{L}(C_l)$.

The corresponding likelihood expression for the high- l case is much more complicated (Planck Collaboration et al., 2014), but the idea is the same - given a signal in a given region of the sky for some given instrument with associated frequency detection band, separate it into the cosmological CMB signal and noise, and take into account smoothing effects (instrument beam function), to produce a likelihood map of the CMB.

Likelihoods from BAO (baryon acoustic oscillation) measurements from the Sloan Digital Sky Survey (Anderson et al., 2014) and the BICEP2/Keck Array collaboration (BICEP2 Collaboration et al., 2016) were also incorporated in the analyses reported in Chapters 3 and 4.

3.5 CAMB

In addition to the data that we obtain from the CMB, we must employ numerical tools to further understand the CMB. The Code for Anisotropies in the Microwave Background (CAMB) by Antony Lewis, Anthony Challinor and Anthony Lasenby (Lewis, Challinor, & Lasenby, 2000) is one such tool, and is currently the best code available for exploring different cosmological models. It is actively maintained by Antony Lewis¹, and there is a Python wrapper available with associated extensive documentation².

CAMB is a parallelised version of CMBFAST (Seljak & Zaldarriaga, 1996). Carrying out the calculations based on the linear theory of cosmological perturbations is computationally expensive, so the novelty behind CMBFAST is that it independently treats geometrical and dynamical contributions to the CMB anisotropies (looking at metric, photon and baryonic perturbations). The corresponding system of (very complicated) equations is then numerically evolved from the radiation-dominated era to the current time.

In this project, we use parameter estimation to give us parameter constraints for various cosmological models. To do this, we employ the Markov Chain Monte-Carlo (MCMC) method, the Metropolis-Hastings algorithm (described in Chapter 5). We will also incorporate the BOBYQA (J. D. Powell, 2009) algorithm for maximum likelihood searches. Together with CAMB, the suite of tools is known as CosmoMC³ (Lewis & Bridle, 2002).

¹<http://cosmocoffee.info/>

²<http://camb.readthedocs.io/en/latest/>

³<http://cosmologist.info/cosmomc/>

3.6 Parameterisation

We can parameterise the CMB angular power spectrum by

$$\mathcal{P}(k) = A_s \left(\frac{k}{k_p} \right)^{n_s - 1},$$

where A_s is amplitude of the density perturbations in the early universe, k is the wavenumber, and k_p is the arbitrary pivot scale usually fixed at $0.05h \text{ Mpc}^{-1}$ ($h = H_0/100$). We will also quote some values with respect to the pivot scale $0.002h \text{ Mpc}^{-1}$. The scalar spectral index, n_s , characterises how the power spectrum varies as the scale changes. A value of $n_s = 1$ would indicate a scale-invariant power spectrum.

We can understand A_s and n_s better by looking at how varying these affect the angular power spectrum. This is calculated using CAMB, and we use the baseline cosmological model with parameters n_s , $\ln(10^{10}A_s)$, τ (same as that below Fig. 3.1), H_0 , $\Omega_c h^2$, and $\Omega_b h^2$. Reference values were obtained using Table 4 from (Planck Collaboration, Ade, P. A. R., et al., 2016). Looking at A_s ,

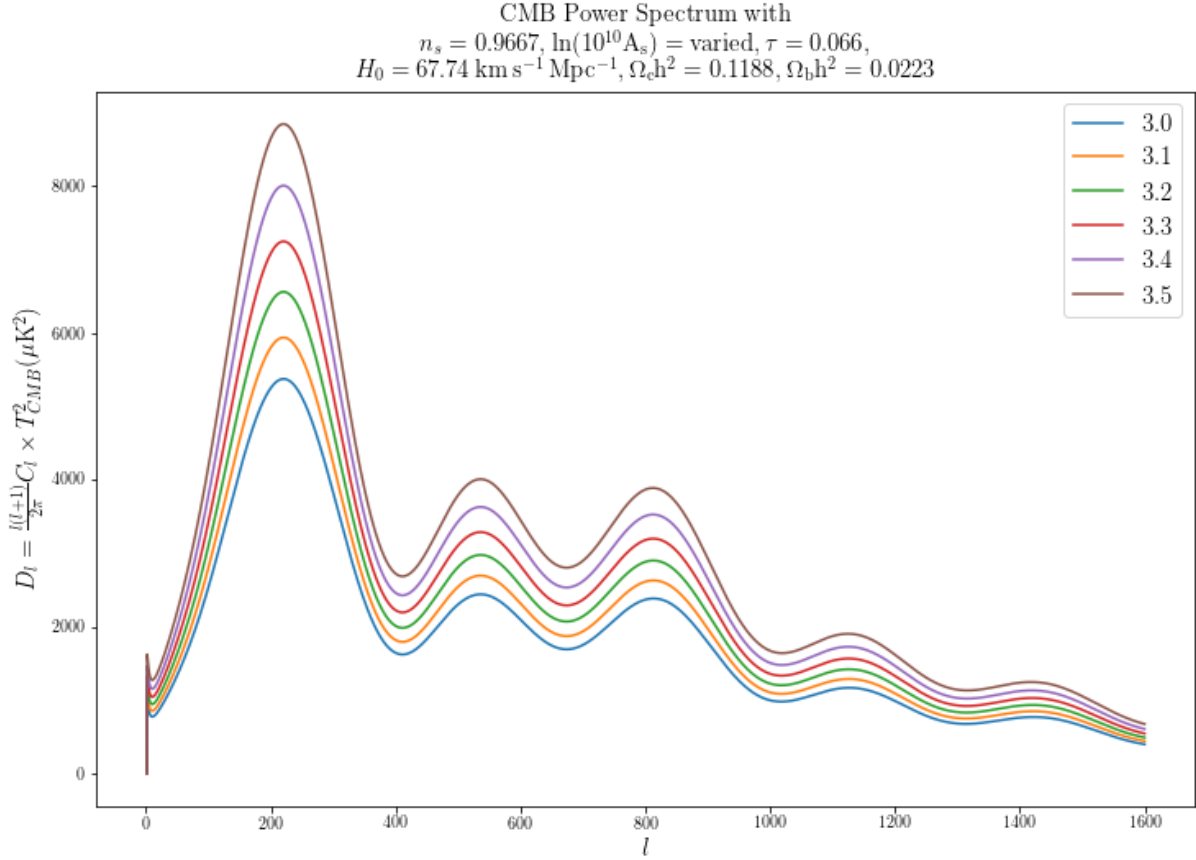


Figure 3.4: Changing $\ln(10^{10}A_s)$

We see that increasing the size of the density perturbations in the early universe lead to larger temperature fluctuations in the CMB today, by definition. The power spectrum does not shift left or right because the magnitude of these fluctuations would affect all angular scales indiscriminately.

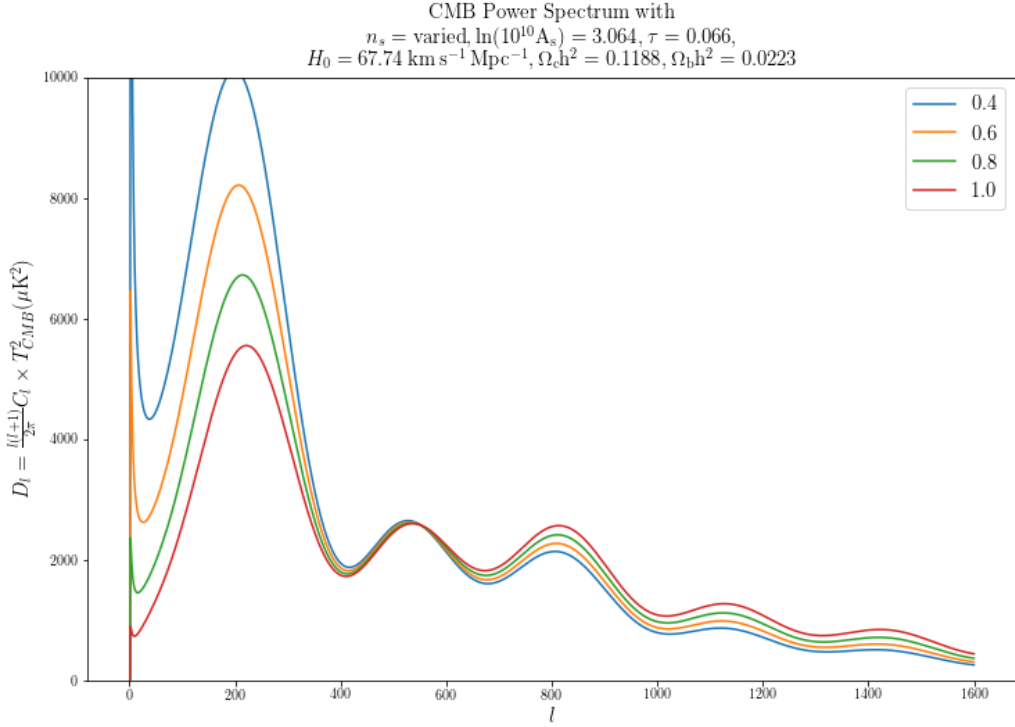


Figure 3.5: Changing n_s

In the case for the scalar spectral index, we see that increasing it will reduce the temperature fluctuations on larger angular scales (i.e. lower l). The scalar spectral index scalar, n_s , relates to the inflation potential - we will see this in the next chapter.

There are also higher order exponents to the power spectrum (Planck Collaboration, Ade, et al., 2016), i.e.

$$\mathcal{P}(k) = A_s \left(\frac{k}{k_p} \right)^{n_s - 1 + \frac{1}{2} \frac{dn_s}{d\ln(k)} \ln\left(\frac{k}{k_p}\right) + \frac{1}{6} \frac{d^2 n_s}{d\ln(k)^2} \left[\ln\left(\frac{k}{k_p}\right) \right]^2 + \dots}$$

where

$$\frac{dn_s}{d\ln(k)}$$

is defined as the running of the scalar spectral index, and

$$\frac{d^2 n_s}{d\ln(k)^2}$$

is the running of the running of the scalar spectral index. These are observables that can be derived from inflationary theory, but are beyond the scope of the current work.

3.7 Implications

Accurate measurements of the CMB allow us to determine parameters characterising the properties of the universe. Examples include the universe's geometry, composition, and reionisation history. Here we summarise the *Planck* observations and briefly mention how the angular power spectrum relates to the physics of the CMB.

Earlier on in this chapter, we discussed the formation of the CMB. We go back to the era of the photon-baryon fluid, the plasma ‘soup’ of baryons and photons. This fluid was not homogeneous -

there were regions of overdensities and underdensities. The overdensities corresponded to deeper gravitational potential wells which baryons fell into. These potential wells could have also been set up by dark matter (more in Chapter 5), which only interact gravitationally. As the baryons fell into the well, the plasma (in the region) heated up, which increased the outward radiation pressure. The compression crescendoed to some maximum value, then the plasma expanded and cooled, relaxing the radiation pressure. As this radiation pressure fell, the (gravitational) effects of the deeper potential wells took over again and resulted in another compression.

This interplay between the dominance of radiation pressure and gravitational effects (due to overdensities and/or dark matter) set up acoustic oscillations in the photon-baryon fluid (Reid, Kittell, Arsznov, & Thompson, 2002). The details of the evolution of this plasma is described by the Einstein-Boltzmann equations (Pan, Knox, Mulroe, & Narimani, 2016).

The angular size of the largest fluctuation in the baryon-photon fluid after photon decoupling is given by (Moore, 2012)

$$\Delta\phi \approx \begin{cases} \frac{\sqrt{a_{\text{PD}}k}}{\sqrt{3}\sin(k)}, & \Omega_k < 0 \\ \frac{\sqrt{a_{\text{PD}}}}{\sqrt{3}}, & \Omega_k = 0 \\ \frac{\sqrt{a_{\text{PD}}k}}{\sqrt{3}\sinh(k)}, & \Omega_k > 0 \end{cases}$$

where $k \equiv 2\sqrt{|\Omega_K|/\Omega_m}$. With $a_{\text{PD}} \approx 1100$, we have that for a flat universe,

$$\Delta\phi \approx \frac{1}{\sqrt{3}} \frac{1}{\sqrt{1 + 1100}} \approx 0.0174 \text{ rad} \approx 1^\circ,$$

which corresponds to about $l \approx 200$. $\Delta\phi$ is plotted against Ω_K in Fig. 3.6 (see Section 8.3 for code). We see that if the universe had negative curvature instead ($\Omega_K < 0$, closed universe), $\Delta\phi$ would be larger; if the universe had positive curvature ($\Omega_K > 0$, open universe), $\Delta\phi$ would be smaller.

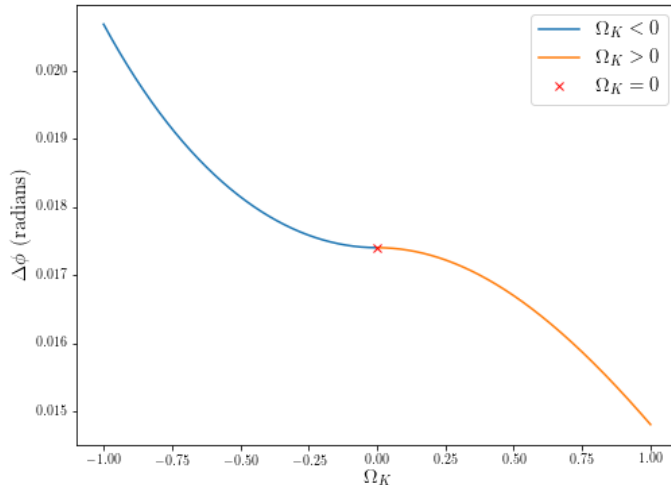


Figure 3.6: $\Delta\phi$ against Ω_K

In Fig. 3.3, there are a number of peaks in the CMB angular power spectrum. There are three peaks of notable amplitude. The odd-numbered peaks correspond to the maximal ‘compression’ phase in the photon-baryon fluid oscillations we outlined above; the even-numbered peaks correspond to the maximal ‘rarefaction’ phase. The locations of these acoustic peaks tell us something about the universe’s geometry and corresponding cosmology. For example, the fact that Planck observes the first acoustic peak in the CMB angular power spectrum at around $l \approx 200$ is consistent with the idea that the universe is flat ($\Omega_K = 0$).

Chapter 4

Bayesian Evidence and Model Selection

Over the last decade, Bayesian statistics has become more ubiquitous in astronomical data analysis. There are many pedagogical introductions with applications to cosmology (e.g. Trotta, 2017).

In this project, we use both parameter estimation and model selection under the Bayesian framework. We reserve the discussion of parameter estimation to the next chapter, looking at model selection first. What is being done here is comparing the relative ‘betting odds’ of two models in explaining the current observations of the universe. In particular, we look at the relative ‘likeliness’ of different inflationary models - i.e. asking which model is most likely to account for observations.

We use `ModeCode` and `PolyChord` (described below) to quantify the impact of different reheating scenarios. We then introduce the inflection point inflation model and compare our results to the 2015 Planck analysis of inflationary models. We perform new evidence calculations with the inflection point inflation model, which is not available in the literature. We also assess the consistency of our results from other inflationary models with Planck’s analysis. Additionally, we look at including the BK14 likelihood from the BICEP2/Keck Array analysis.

4.1 Bayesian Evidence

4.1.1 Theory

As written in Section 2.4.6, the ratio of the Bayesian evidences of two models will tell us how likely one model is over the other, in explaining current observations. Formally, the Bayesian evidence, E , is defined as

$$E = \int d\theta^N P(\theta_i) \mathcal{L}(d|\theta_i);$$

the integral of the likelihood, the probability of getting the data given some model, over the parameter volume defined by $\{\theta_1, \dots, \theta_N\}$; this is weighted by the prior $P(\theta)$, a normalised joint probability distribution of initial guesses for the range of values the parameters take.

We write the ratio of the Bayesian evidences of two models, E_a and E_b , as

$$\Delta \ln(E_{ab}) := \ln \left(\frac{E_a}{E_b} \right).$$

The evidence ratio is usually compared using the Jeffreys' scale, which provides a qualitative interpretation (Jeffreys, 1998):

$\Delta \ln(E_{ab})$	Evidence
[0, 1.1)	Weak
[1.1, 3)	Definite
[3, 5)	Strong
[5, ∞)	Very strong

Table 4.1: Jeffreys' Scale

An evidence ratio of $\Delta \ln(E_{ab})$ implies an odds ratio of $e^5 : 1$, or about $150 : 1$.

4.1.2 Calculation

In calculating the evidence values for any given model, one has to evaluate an integral over many parameters, and this is very computationally expensive. In this project, the typical number of parameters considered is around 30. This will involve both cosmologically relevant parameters (e.g. H_0, Ω_ch^2) and nuisance parameters, which are not interesting in and of themselves but must be incorporated in the analysis. In particular, the nuisance parameters relate to the likelihood data (e.g. from Planck) that we will use in calculating the evidence.

We employ ModeChord¹, which is a combination of CosmoMC, PolyChord² ³ and ModeCode⁴. We have discussed CosmoMC above. PolyChord (Handley, Hobson, & Lasenby, 2015) is a nested sampler (Skilling, 2006) which utilises slice sampling to sample multidimensional likelihoods. Simply put, the relationship between the likelihood and the prior is estimated, then for any given parameter X that is integrated over, the region (i.e. integrand associated with the variable) is ‘sliced’ and then sampled from $[0, f(x)]$, where $f(x)$ is the probability density function of X . A line is drawn across $y = f(x)$, and the algorithm then samples the point (x, y) along the curve. In the multidimensional equivalent iteration, this sampling is repeated a number of times, resulting in a chain of values with each sampled value correlated to the previous iteration. ModeCode (Mortenson, Peiris, & Easther, 2011, Easther & Peiris, 2012, Norena, Wagner, Verde, Peiris, & Easther, 2012) is a code solving for the scalar/tensor perturbation spectra for inflationary models. ModeChord also produces posterior chains, which will be useful in generating joint posterior probability distributions (in the form of triangle plots) for relevant cosmological parameters.

Both Metropolis-Hastings (see Chapter 4) and slice sampling are MCMC algorithms, but slice sampling is the method of choice in PolyChord. Slice sampling is more efficient than Metropolis-Hastings once the number of parameters involved in the evidence calculations is large, i.e. over 10 (Handley et al., 2015).

In the Appendix, we will give an example of an operational input parameter file (Section 8.5) used in the project. However, we briefly point out that there are two relevant PolyChord tuning parameters used in the sampling process, the number of live points `nlive` and `num_repeats`. Essentially `nlive` is akin to a resolution parameter - a larger number of live points roughly equates to sampling the integrand (for the evidence) more thoroughly. This is typically set to about $25 \times$ the number of parameters involved. `num_repeats` relates to the length of the slice sampling chain

¹<https://github.com/ucl-cosmoparticles/modechord/>

²<https://ccforge.cse.rl.ac.uk/gf/project/polychord/>

³http://cobaya.readthedocs.io/en/latest/sampler_polychord.html

⁴<http://modecode.org/>

that was used in the generation of new live points. Turning this parameter up reduces the correlation between the initial guess for the sample and the final sample value. A low `num_repeats` results in unreliable evidence estimates (Handley et al., 2015). A typical run sets this value to roughly $3 \times$ the number of parameters involved. Potential pitfalls that arise in practice are described in Section 8.4.

4.2 Inflationary Model Selection

We employ model selection to discriminate between the different inflationary models. This project is in part an update of previous work done in Easter & Peiris, 2012.

In order for us to specify an inflationary model, we need the form of the inflaton potential, the reheating mechanism, and priors for various cosmological and relevant inflationary parameters.

4.3 Models

As outlined in Section 2.4.6, a class of simple inflaton potentials are the monomials of the form

$$V(\phi) = \lambda \frac{\phi^n}{n}.$$

In particular,

$$\begin{aligned} V(\phi) &= \frac{3}{2} \lambda \phi^{\frac{2}{3}}; \\ V(\phi) &= \lambda \phi \text{ (linear)}; \\ V(\phi) &= \frac{1}{2} m^2 \phi^2 \text{ (quadratic)}; \\ V(\phi) &= \frac{\lambda}{4} \phi^4 \text{ (quartic)}. \end{aligned}$$

The Planck analysis (Planck Collaboration, Ade, et al., 2016) also looks at $n = 4/3$ and $n = 3$. We also look at the general inflection point model, laid out in Section 4 of (Musoke & Easter, 2017). The inflaton potential is

$$V(\phi) = \lambda \left(\frac{M^2}{2} \phi - \frac{2}{3} \Delta M \phi^3 + \frac{1}{4} \phi^4 \right).$$

The large field scenario that we specifically looked at was that of the *effective quadratic potential* where $M \gg 10M_{\text{Pl}}$, i.e. the inflaton potential is effectively quadratic during the course of inflation, but the inflection point can substantially modify the dynamics.

4.4 Set-up

With the preceding theory in mind, one can finally start running their first evidence calculation. See Section 8.4 for a comprehensive tutorial with the hilltop inflaton potential (not used in this project otherwise).

The likelihoods used in this section can be found in

`path_to_CosmoMC/batch2/`

and they have the extension ‘.ini.’ Here, we use

Designation	File name	Description
Planck High- l TT	plik_dx11dr2_HM_v18_TT	Temperature likelihood for $l \geq 30$
Planck lowTEB	lowTEB	Temperature and polarization likelihood for $l \leq 29$
BAO	BAO	Measurements of baryon acoustic oscillations
BK14	BK14	Data from BICEP2/Keck Array

Table 4.2: List of likelihoods

The bottom two likelihoods refer to likelihoods from BAO (baryon acoustic oscillation) measurements from the Sloan Digital Sky Survey (Anderson et al., 2014), and the BICEP2/Keck Array collaboration (BICEP2 Collaboration et al., 2016) respectively.

One should note that the combination *Planck TT + lowP* from Paper XX of the Planck 2015 results (Planck Collaboration, Ade, et al., 2016) is specifying the usage of the first two likelihoods in Table 4.2 in the parameter file.

One can assume instant reheating, i.e. the inflaton decayed into Standard Model particles immediately after inflation and the universe became radiation-dominated. This is done by having the line

```
DEFAULT(batch2/modecode_inst.ini)
```

in the parameter file and commenting all other reheating files (or remove the lines). Additionally, in `./batch2/modecode_defaults.ini`, one should have the logical

```
instreheat = T
```

The instant reheating results turned out to be yield overly simplistic results. Thus for most of the project, we looked at the case of non-instant reheating with following reheating settings matching that of Planck (Planck Collaboration, Ade, et al., 2016):

- The corresponding reheating file is

```
DEFAULT(batch2/modecode_reheat3a.ini)
```

- Changed the 4 lines in `./batch2/modecode_defaults` accordingly

```
modpk_rho_reheat = 1.d12
modpk_w_primordial_lower=-0.333333
modpk_w_primordial_upper=0.333333
```

```
instreheat = F
```

Physically speaking, $w \geq 1/3$ states that inflation has ended; $w \leq 1/3$ stipulates a mix of matter and radiation, eliminating exotic scenarios such as a ‘stiff fluid’.

4.5 Results and Discussion

4.5.1 Instant reheating

First we look at instant reheating. This corresponds to $w_{\text{prim}} = 1/3$, where w_{prim} characterises the primordial equation of state of the corresponding (perfect) fluid in the early universe. Using the linear potential, and the Planck High- l TT + Planck lowTEB + BAO likelihoods (in accordance with Planck Collaboration, Ade, et al., 2016), we obtain the following triangle plot showing the joint posterior distributions (generated by GetDist⁵, see Section 8.6)

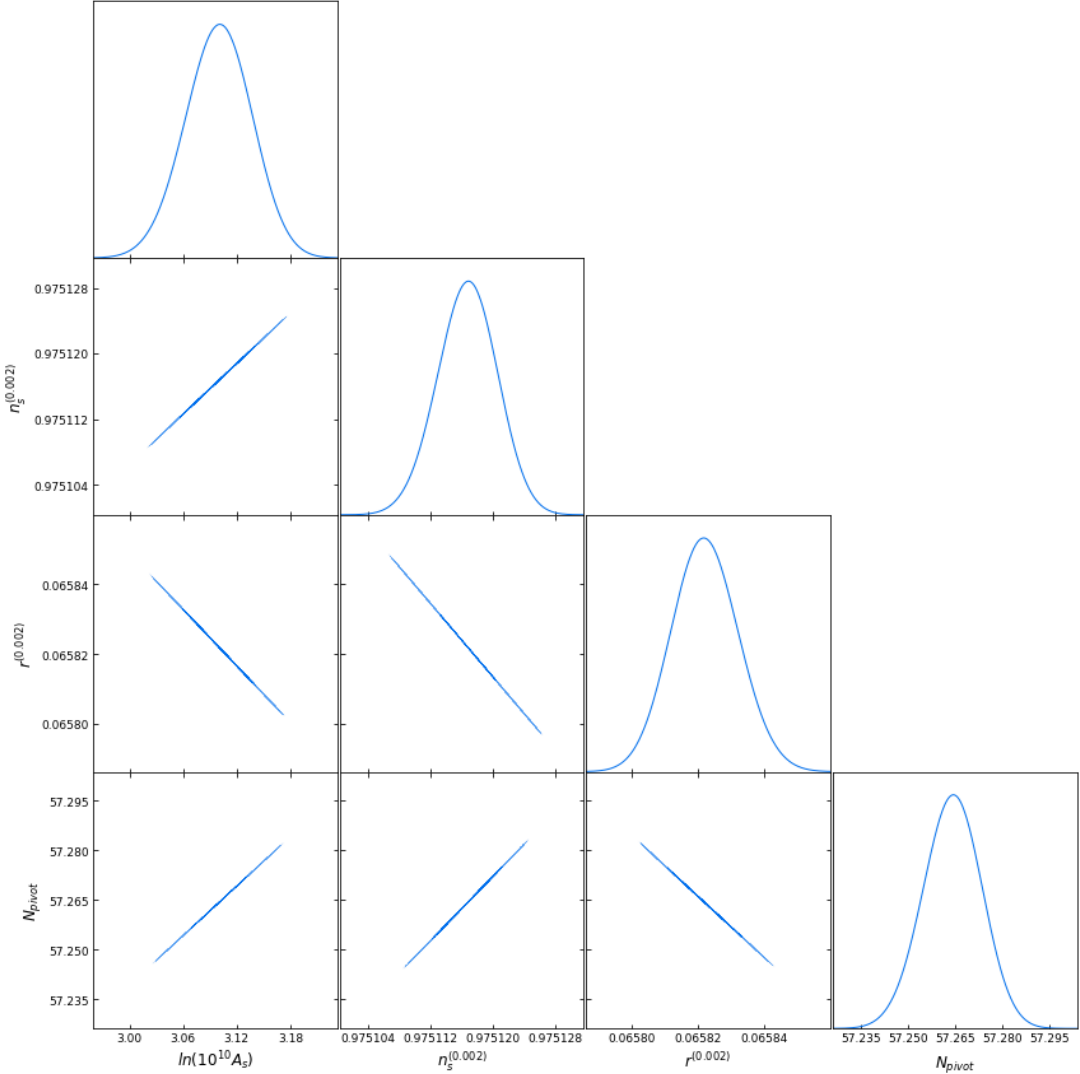


Figure 4.1: $V(\phi) = \lambda\phi$ with instant reheating

The ranges for n_s and r are very narrow (vary up to the 4th decimal place). In previous runs, Easterer attributed this to N_{pivot} , the number of e-folds after the pivot scale left the horizon, being fixed. For this example, N_{pivot} was given a uniform prior in range [30, 70] with a central value of 50. This suggests that r , the ratio of amplitudes of tensor perturbations and scalar perturbations, and n_s (derived parameters) were stuck in the first place. The line in `./batch2/modecode_inst.ini` with

⁵<http://getdist.readthedocs.io/en/latest/plots.html>

```
N_pivot = 50
```

was commented as well. This might correspond to a tight constraint on the scalar amplitude, which fixes λ , which fixes N_{pivot} .

4.5.2 Non-instant reheating

We now look at the case where reheating after inflation is not instantaneous. This pertains to having a uniform prior on w_{prim} in the range $[-1/3, 1/3]$. We also have that ρ_{th} (ρ_{end}), the energy density after thermalisation (at the end of reheating), has the prior $[(1 \text{ TeV})^4, \rho_{\text{end}}]$ with $(1 \text{ TeV})^4 = 10^{12} (\text{GeV})^4$, i.e.

```
modpk_rho_reheat = 1.d12
```

We use the Planck High- l TT + Planck lowTEB + BAO likelihoods. Here, we will present evidence ratios and also triangle plots for selected parameters.

We compare between the inflationary potentials

$$V(\phi) = \frac{\lambda}{4}\phi^4 \quad ; \quad V(\phi) = \frac{m^2}{2}\phi^2 \quad ; \quad V(\phi) = \lambda\phi \quad ; \quad V(\phi) = \frac{3}{2}\lambda\phi^{\frac{2}{3}}.$$

The corresponding evidence values will be quoted E_4, E_2, E_1 , and E_{23} respectively. For this particular run, we had

$$E_4 = -5700.99 \pm 0.20 \quad ; \quad E_2 = -5680.92 \pm 0.19 \quad ; \quad E_1 = -5677.94 \pm 0.19 \quad ; \quad E_{23} = -5677.24 \pm 0.19.$$

We choose to quote the evidence ratios with respect to the linear potential.

Evidence ratio	Value
$\ln(E_4/E_1)$	-23.04 ± 0.27
$\ln(E_2/E_1)$	-2.98 ± 0.27
$\ln(E_{23}/E_1)$	$+0.70 \pm 0.27$

Table 4.3: Evidence ratios, relative to the linear potential, corresponding to non-instant reheating scenario; $w_{\text{int}} \in [-1/3, 1/3]$, $\text{modpk_rho_reheat} = 1.\text{d}12$

For evaluation with Jeffreys' scale in Table 4.1, we simply take the absolute value of the evidence ratios, which would imply that the evidence values are flipped around in the ratio.

We can first see from Table 4.3 that the quartic potential is strongly disfavoured, i.e. there is very strong evidence against it. Thus the quartic potential can be ruled out definitively as being the inflaton potential. There is also strong evidence against the quadratic potential, which suggests that convex inflaton potentials are disfavoured. The evidence ratio between the linear potential and

$$V(\phi) = \frac{3}{2}\lambda\phi^{\frac{2}{3}}$$

tells us that we cannot discriminate between the two inflaton potentials as there is weak evidence disfavouring the linear potential, i.e. a mere 2:1 odds.

The inferences are consistent with the results from the 2015 Planck analysis (Planck Collaboration, Ade, et al., 2016). The forthcoming final data release that is expected to take place in the

next few months⁶ promises to conjure stronger discriminatory power between the inflationary models.

To gauge the impact of the reheating assumptions, we now set `modpk_rho_reheat = 1.d-4 ([model]_restr)`, i.e. ρ_{th} has the prior $[(100\text{MeV})^4, \rho_{\text{end}}]$. We have not included the potential

$$V(\phi) = \frac{3}{2} \lambda \phi^{\frac{2}{3}}$$

for this analysis. Having a lower energy density scale for reheating allows us to ‘see’ closer to the end of inflation. Blue corresponds to `modpk_rho_reheat = 1.d12`, and red corresponds to `modpk_rho_reheat = 1.d-4`.

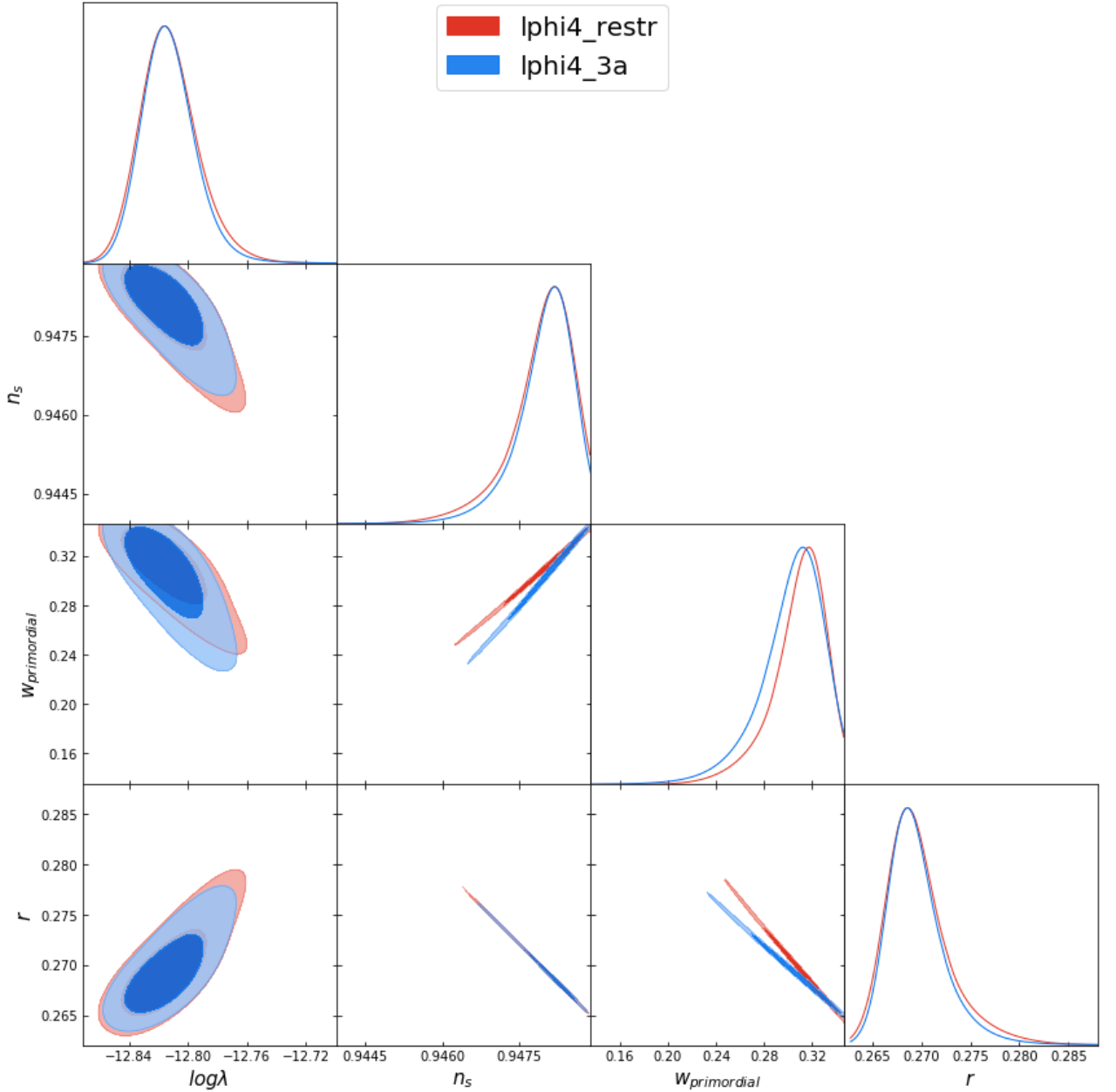


Figure 4.2: Testing the sensitivity of the reheating energy density for the quartic potential

⁶<https://www.aanda.org/2016-press-releases/1243>

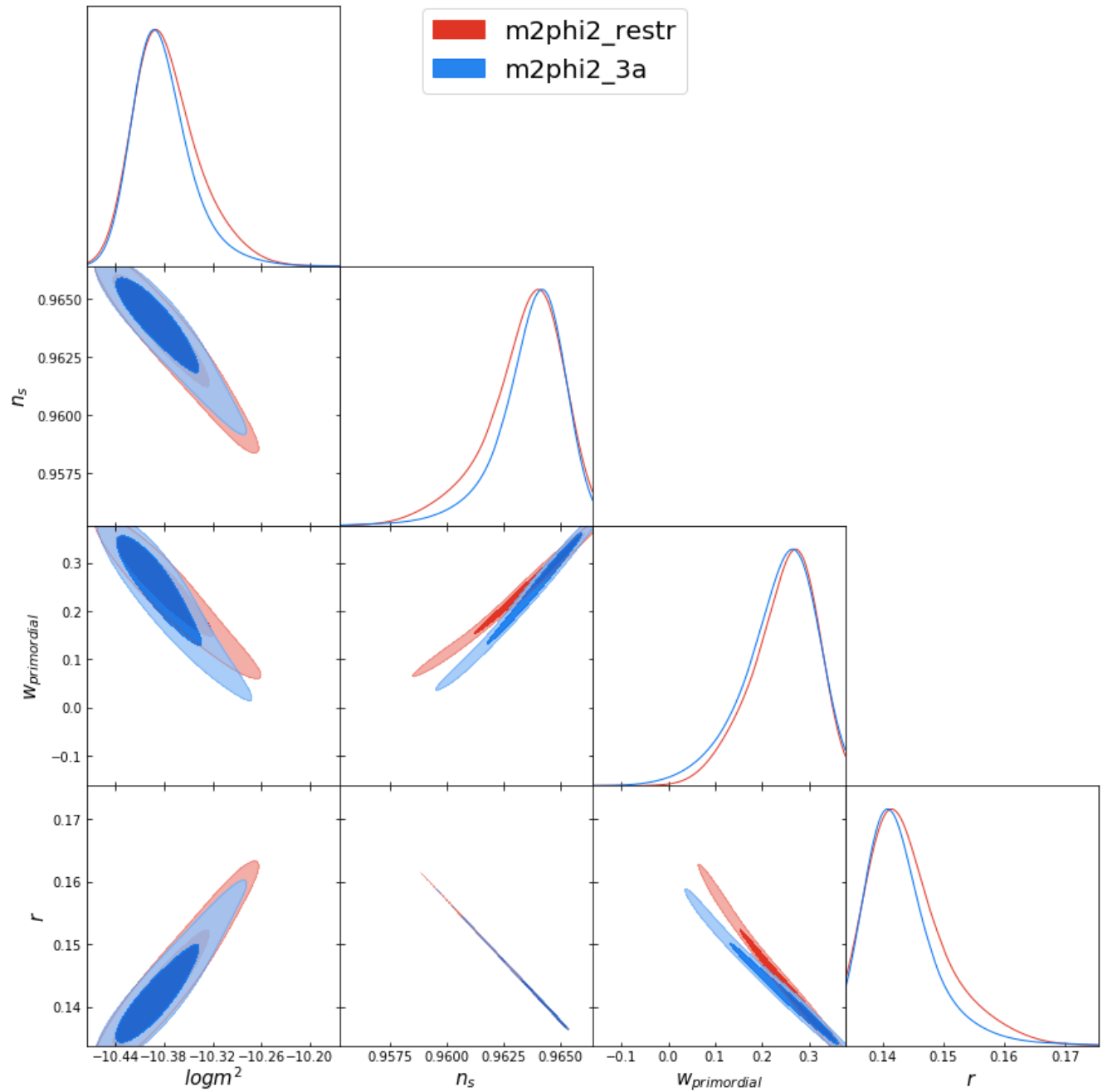


Figure 4.3: Testing the sensitivity of the reheating energy density for the quadratic potential

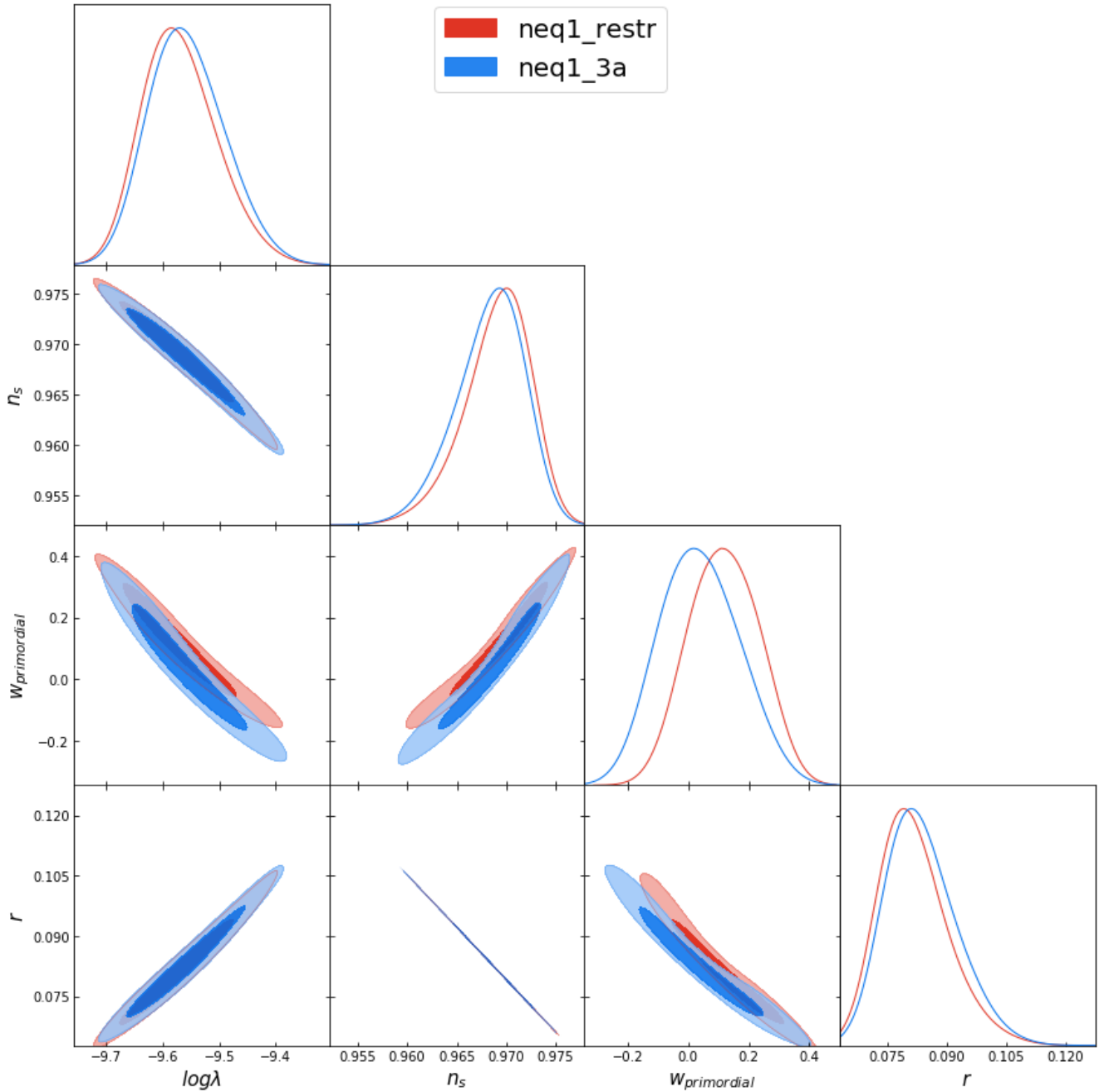


Figure 4.4: Testing the sensitivity of the energy density assumption for the linear potential

We see that for all three potentials, the biggest difference is that w_{prim} is pushed towards lower values for the larger value of ρ_{th} . We can see this with the relation (Demozzi & Ringeval, 2012)

$$\rho_{\text{th}} = \rho_{\text{end}} e^{-3\Delta N(1+w_{\text{prim}})}$$

where $\Delta N \geq 0$. Having a larger value for ρ_{th} , i.e. a large reheating energy density, would result in a preference for lower values of w_{prim} .

The corresponding evidence ratios are:

Reheating energy density	$\ln(E_4/E_1)$	$\ln(E_2/E_1)$
1.d12	-23.04 ± 0.27	-2.98 ± 0.27
1d-4	-23.39 ± 0.27	-3.79 ± 0.27
Within	0.7σ	1.6σ

Table 4.4: Comparing evidence ratios corresponding to non-instant reheating scenario; $w_{\text{int}} \in [-\frac{1}{3}, \frac{1}{3}]$, `modpk_rho_reheat = 1.d-4` and `modpk_rho_reheat = 1.d12`

The priors are specified thusly:

`param[parameter] = 'central value' 'lower bound' 'upper bound' 'starting width' 'proposed width'`.

The specific priors used here were:

- `param[omegabh2] = 0.02225 0.02 0.025 0.0001 0.0001`
- `param[omegach2] = 0.12 0.08 0.16 0.001 0.0005`
- `param[theta] = 1.0411 1.00 1.08 0.004 0.004`
- `param[tau] = 0.09 0.01 0.20 0.001 0.001`
- `param[omegak] = 0` #specify a single value if we want the parameter to be fixed
- `param[logA] = 3.1 2.5 3.5 0.001 0.001`
- `param[ns] = 0.96 0.8 1.2 0.004 0.002`
- `param[r] = 0.03 0 2 0.001 0.001`
- `param[N_pivot] = 50 30 70 0.1 0.1`
- `param[vpar1] = -13.4 -16.0 -10.0 0.1 0.1` #for $V(\phi) = \lambda\phi^4/4$
- `param[vpar1] = -10.3 -13.5 -8.0 0.1 0.1` #for $V(\phi) = m^2\phi^2/2$
- `param[vpar1] = -9.4 -13.0 -7.0 0.05 0.05` #for $V(\phi) = \lambda\phi$
- `param[vpar1] = -9.4 -13.0 -7.0 0.05 0.05` #for $V(\phi) = 3\lambda\phi^{2/3}/2$

where the priors for the post-cosmological parameters (defined previously) were chosen based on the runs that was done in Chapter 5.

The evidence ratios from Table 4.4 show that the conclusions do not change, where the quartic potential is strongly disfavoured due to very strong evidence against it, and there is strong evidence against the quadratic potential with respect to the linear potential.

4.5.3 Adding the BK14 likelihood

We now introduce the usage of BK14 likelihood from Table 4.2. The first attempts at a run were not successful. With the same set of priors for the cosmological and inflationary parameters above, the following error was obtained:

Error in Matrix_Diagonalize

Looking through the documentation, the error occurred in the module `./camb/Matrix_utils.F90`. The module was used in 6 instances, in the `.f90` files in `source/`: `CMBlikes`, `EstCovmat`, `GetDist`, `Matrix_utils_new`, `minimize`, `samples`. We suspect that the error arose because the sampler happened to probe a region in likelihood space which corresponds to a highly unphysical value of r , the tensor-to-scalar ratio, but which is allowed by the inflationary prior. This is supported by results from the run below, where we mostly use the same priors as above, with the following difference (note the tighter ranges):

- param[vpar1] = -12.82 -12.9 -12.7 0.001 0.001 # quartic potential
- param[vpar1] = -10.38 -10.5 -10.2 0.001 0.001 # quadratic potential
- param[vpar1] = -9.55 -9.7 -9.4 0.001 0.001 # linear potential

The corresponding triangle plots are

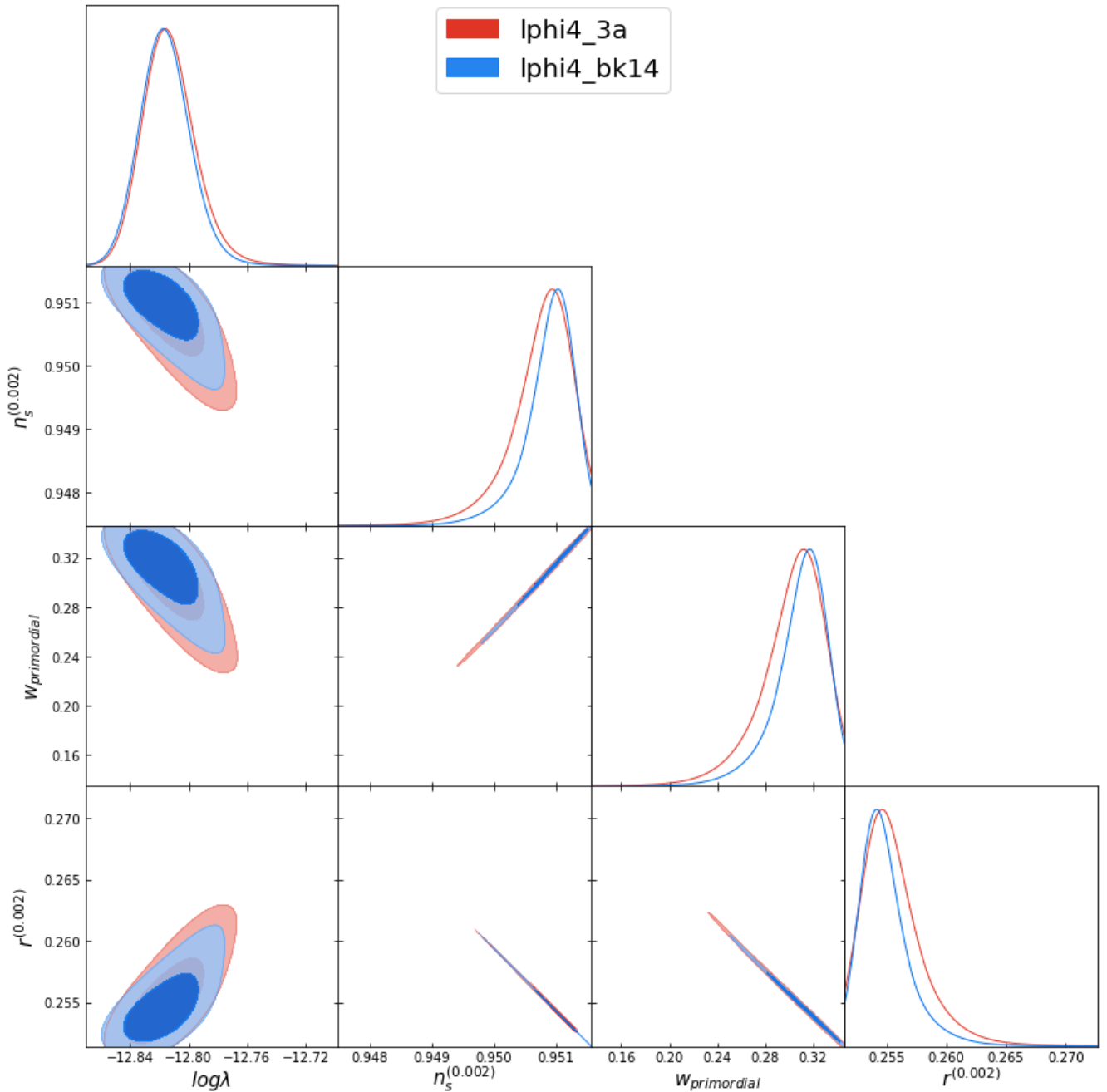


Figure 4.5: Comparing between two different priors for λ in the quartic potential with the BK14 likelihood

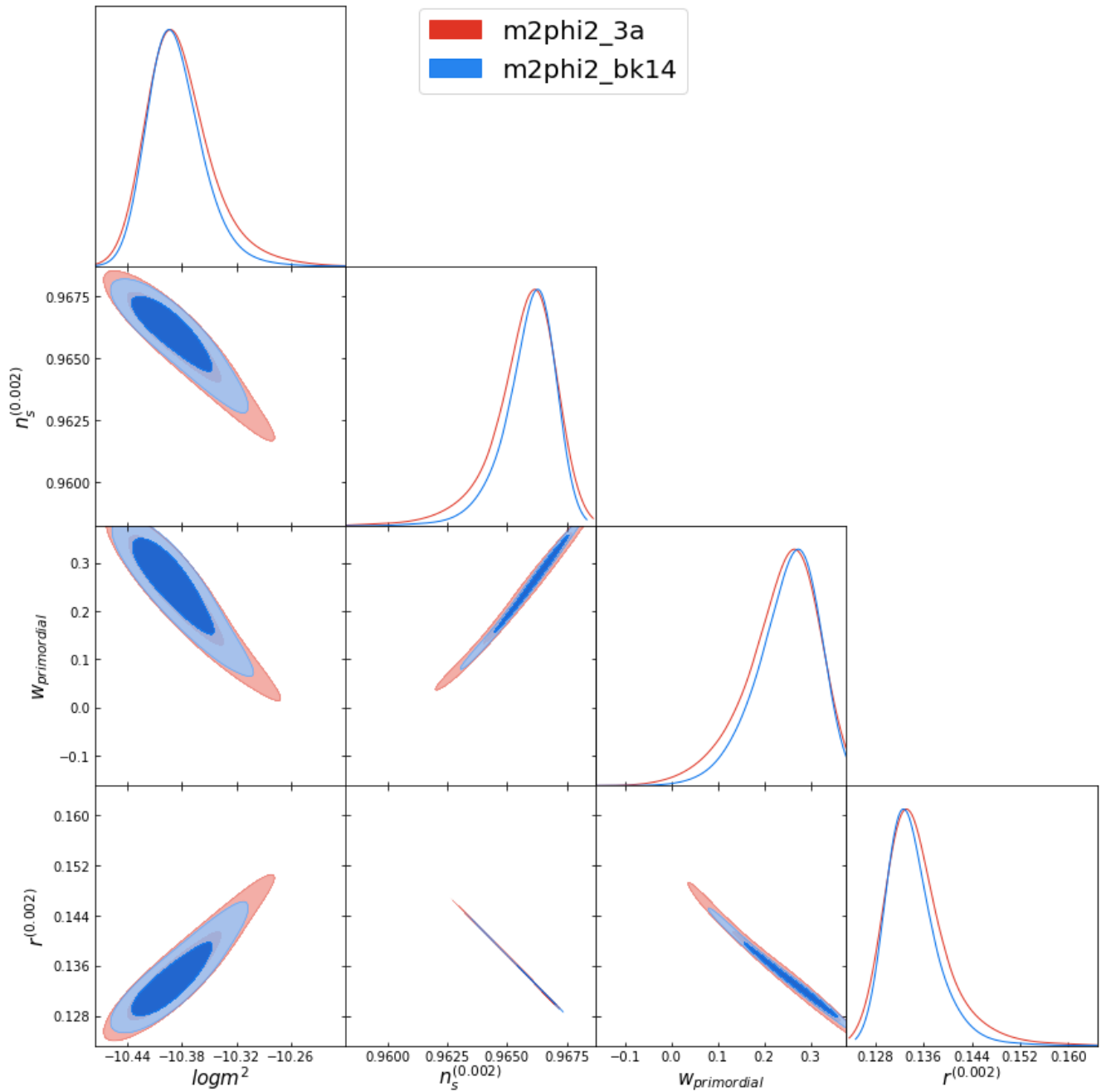


Figure 4.6: Comparing between two different priors for m^2 in the quadratic potential with the BK14 likelihood

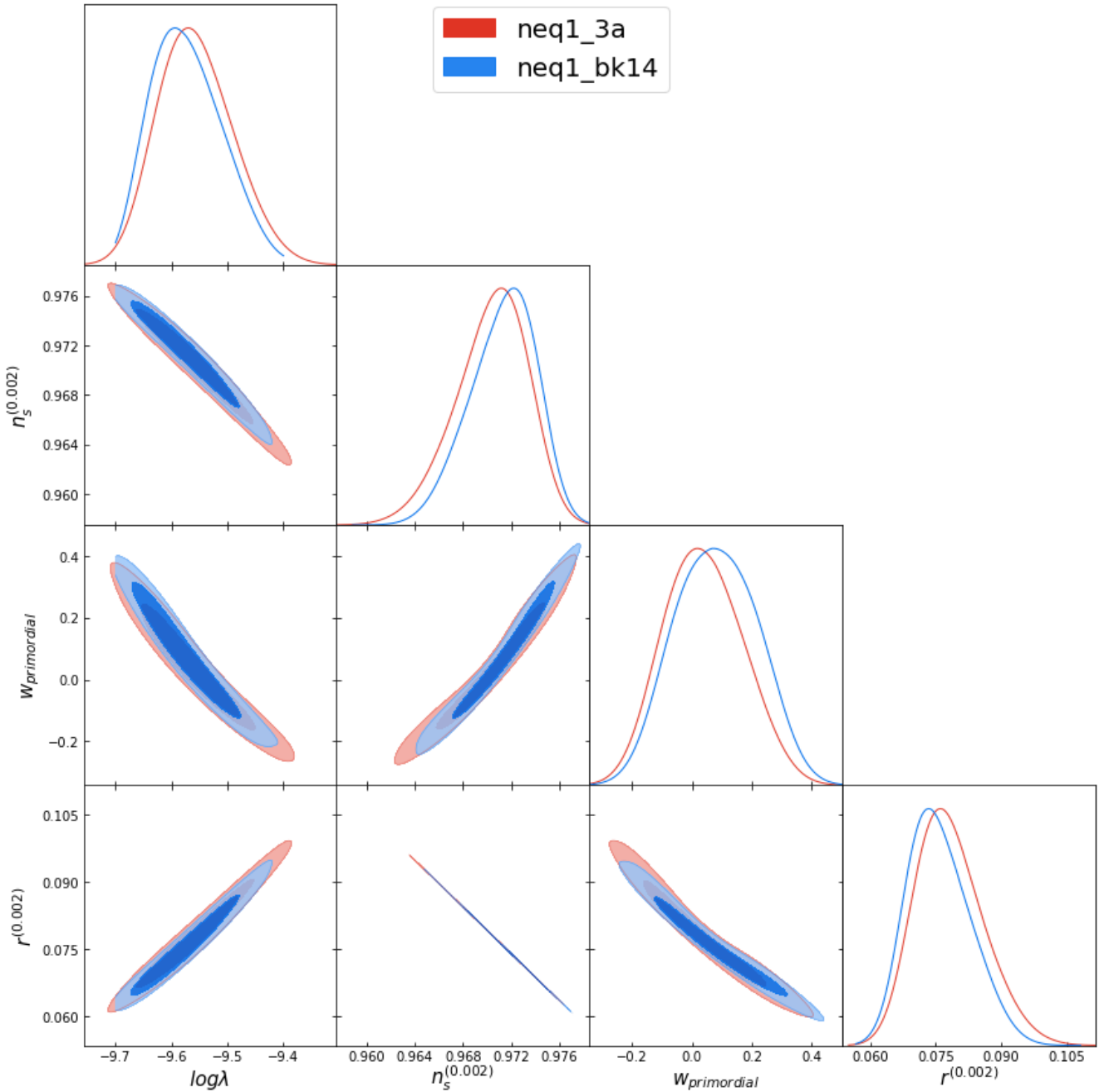


Figure 4.7: Comparing between two different priors for λ in the linear potential with the BK14 likelihood

For the quartic, quadratic, and linear potentials, we see that the posteriors corresponding to using the BK14 likelihood are narrower, i.e. the joint posterior distributions are tighter and the corresponding 1D posterior distributions are narrower. This shows the constraining power of the BK14 likelihood particularly for n_s and r , empirical inflationary spectral parameters.

Future work will involve finding out the exact cause of the `Matrix_Diagonalize` error and rerunning the models with the usual (wide) prior to provide a consistent evidence calculation. There was not enough time to implement this, but Easther recommended a cut in r (priv. comm.) similar to that of the cut for A_s (Easther & Peiris, 2012).

4.5.4 Inflection Point Inflation

Next let us look at the inflection point inflation model. Since this was a new model to be implemented, we had to add a new function to `camb/modpk_potential.f90`, which specifies the potentials, and the corresponding first and second derivatives of the potentials. Nathan Musoke and I contributed this addition. The inflaton potential is

$$V(\phi) = \lambda \left(\frac{M^2}{2} \phi - \frac{2}{3} \Delta M \phi^3 + \frac{1}{4} \phi^4 \right).$$

We looked at the *large field, log prior* scenario (Musoke & Easther, 2017) where the following priors for M , λ and Δ were suggested:

$$M_{\text{Pl}} \leq M \leq 50M_{\text{Pl}};$$

$$-6 \leq \log_{10}(|\Delta - 1|) \leq 0;$$

$$-15 \leq \log_{10}(\lambda) \leq 5.$$

We first note that for $\Delta - 1 > 0$, there is a trapping potential for the inflaton, a local maximum. We focus on the inflection point inflation scenario with $\Delta - 1 < 0$, which is more physically interesting. We use the prior $-6 \leq \log_{10}(|\Delta - 1|) \leq -1$ instead as $\log_{10}(|\Delta - 1|) \approx 0$ requires more careful specification of the initial conditions for inflation. This is appended in `modpk_potential.f90` thusly (derivatives are added in the obvious fashion; `ModeChord` was rebuilt):

```
case(18)
! Inflection point inflation - large field log

M_ii = vparams(1)
!Delta_ii = (10.d0**vparams(2))+1.d0 !Delta>1
Delta_ii = 1.d0 - 10.d0**vparams(2) !Delta<1
lambda_ii = 10.d0**vparams(3)

pot = lambda_ii * (&
+ M_ii**2 / 2.0d0 * phi**2 &
- 2.0d0 / 3.0d0 * M_ii * Delta_ii * phi**3 &
+ 1.0d0 / 4.0d0 * phi**4 &
)
```

We looked at two different cases, with:

$$a) M_{\text{Pl}} \leq M \leq 20M_{\text{Pl}} \rightarrow \text{param[vpar1]} = 10.0 \ 5.0 \ 20.0 \ 0.01 \ 0.01;$$

$$b) M_{\text{Pl}} \leq M \leq 50M_{\text{Pl}} \rightarrow \text{param[vpar1]} = 5.0 \ 2.5 \ 50.0 \ 0.01 \ 0.01,$$

with an initial value of the inflaton of 5.0. The Planck High- l , Planck lowTEB and BAO likelihoods were used for this analysis. We adopted the same reheating scenario as above.

The reason *a*) was done above was to ‘test things out’. *b*) corresponds to a more physically feasible scenario. The priors were chosen based on the analysis done by Musoke and Easther (Musoke & Easther, 2017).

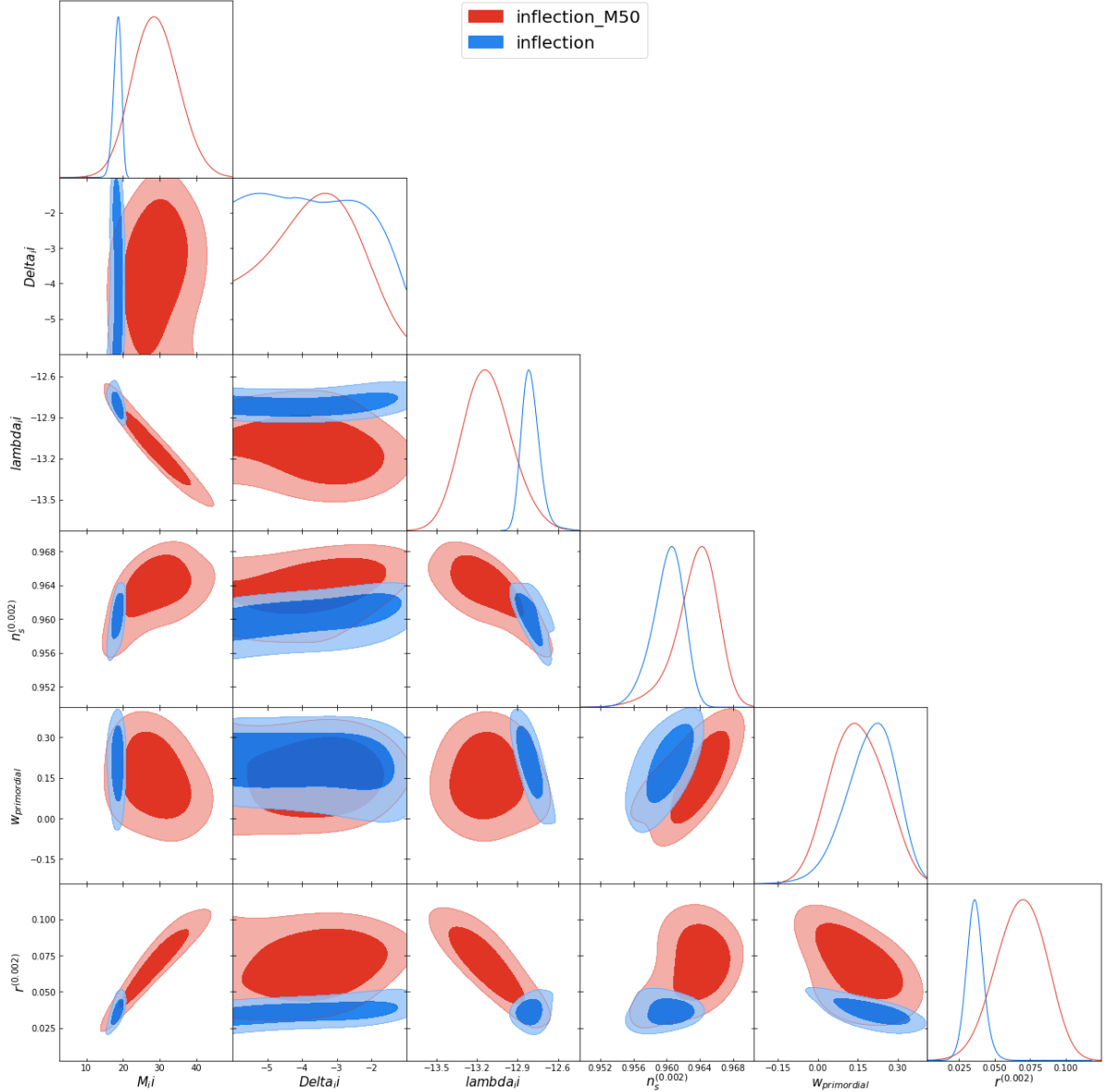


Figure 4.8: Comparing between priors for M in the inflection point inflation model; blue corresponds to a ; red corresponds to b

We extend Table 4.3 by reporting the evidence ratio calculations, with respect to the linear potential, for the inflection point inflation potential:

Evidence ratio	Value
$\ln(E_4/E_1)$	-23.04 ± 0.27
$\ln(E_2/E_1)$	-2.98 ± 0.27
$\ln(E_{23}/E_1)$	$+0.70 \pm 0.27$
$\ln(E_{\text{in},20}/E_1)$	-2.94 ± 0.27
$\ln(E_{\text{in},50}/E_1)$	-2.11 ± 0.27

Table 4.5: Evidence ratios, relative to the linear potential, corresponding to non-instant reheat-ing scenario; $w_{\text{int}} \in [-1/3, 1/3]$, `modpk_rho_reheat = 1.d12` including the inflection point inflation potential. $E_{\text{in},20}$ refers to case a); $E_{\text{in},50}$ refers to case b).

Our interpretations vary depending on which case we look at, i.e. which prior we adopt for M . Truncation in the prior for M is important since the (blue) joint posterior distribution in Fig. 4.8 shows that M favours values higher than $M = 20M_{\text{Pl}}$. This also highlights the potency of the Planck data in constraining different scenarios within an inflationary model.

In the following, we refer to case *b*) for results that correspond to a more physical model. From the evidence ratios in Table 4.5, we see that there is definite evidence against the inflection point model, so there is some disfavour against it, but it cannot be ruled out completely. Future work should look at different scenarios of this novel inflection point inflation model as it promises to draw out interesting insights, e.g. look at $\log_{10}(|\Delta - 1|) \approx 0$ taking into careful consideration the initial conditions for inflation.

Let us now look at the triangle plots. From the 2015 Planck inflation paper (Planck Collaboration, Ade, et al., 2016), the bound on r (pivot scale at $k = 0.002 \text{ Mpc}^{-1}$) is $r < 0.10$, which is consistent with the posterior distribution for r above. The scalar spectral index n_s is reported to be at 0.971 ± 0.005 , so within 2σ , our results for the inflection point inflation model are in agreement with Planck's results for the spectrum when characterised with the empirical variables r and n_s . However, large values of M corresponds to a purely quadratic potential, which is disfavoured.

The new inflection point inflation model proposed by Musoke and Easther demonstrate that it can generate a large but not arbitrary range of the empirical spectral parameters r and n_s . The analysis here shows that the constraints on r derived with the Planck High- l TT, Planck lowTEB, and BAO likelihoods lead to posteriors that are very different from the priors, indicating that current data places increasingly tight constraints on large field inflationary scenarios. Future work should incorporate the BK14 likelihood as it possesses the power to further constrain n_s and r as shown above in Section 4.5.3.

Chapter 5

Understanding the Need for Dark Matter

As mentioned above, the angular power spectrum of the cosmic microwave background (CMB) is sensitive to many cosmological parameters, including dark matter, parameterised by $\Omega_c h^2$. Dark matter is the invisible substance that does not emit or absorb light, but only interacts with baryonic matter gravitationally.

There are many independent indirect lines of evidence for dark matter. The first set of observations that suggested the existence of dark matter was made by Fritz Zwicky (Zwicky, 1937) almost 80 years ago, where he used measurements of the motion of galaxies at the Coma Cluster edge to infer its mass. This was compared with the mass estimate based on the cluster's luminosity and number of galaxies contained. The amount of visible mass could not account for the required mass to ensure stability of the motions of the galaxies at the edge of the cluster. This led Zwicky to infer the existence of dark matter.

Modern efforts started with Vera Rubin and Kent Ford in the late 1960s (Rubin & Ford, 1970), where they measured the radial velocities of 67 H II (ionized hydrogen) regions at varying distances from the centre of the Andromeda galaxy. This work formed the basis of the consensus in the astronomical community that dark matter exists. Key work by Rubin and others (Rubin, Ford, & Thonnard, 1980) asked the question ‘Is the luminous matter only a minor component of the total galaxy mass?’ The answer turned out to be ‘yes’.

Beyond measurements of galactic clusters and galaxies, there are other independent inferences of the existence of dark matter, from gravitational lensing to observations of the Bullet Cluster. In this project, we looked at how dark matter explains the CMB. Part of the motivation for this project came from criticisms by dark matter naysayers, who instead proposed modifications to Newtonian theory, the modified Newtonian dynamics (MOND), to account for the dark matter. While MOND can explain the galaxy rotation curves, it does not explain the other independent indirect observations of dark matter, including the CMB.

We look at how the addition of dark matter, parameterised by $\Omega_c h^2$, would affect the angular power spectrum. This is done by comparing the best fit from Planck and the best fit to data for $\Omega_c h^2 \approx 0$. We quantify this with a χ^2 analysis and we will demonstrate the incredible predictive power of dark matter in explaining current observations. While this is physically well-understood, such a quantitative analysis has not been done before until now. In the end, through observations of the CMB, we show that alternative explanations for dark matter (e.g. modified gravity) can be discounted by the simple addition of dark matter to existing cosmological models.

5.1 Algorithms

In order to assess the need for dark matter to explain the CMB, we used `CosmoMC` to carry out parameter estimation. Two methods incorporated in `CosmoMC` were used for this analysis - the Metropolis-Hastings algorithm and the Bound Optimisation BY Quadratic Approximation (BOBYQA).

5.1.1 Metropolis-Hastings

The Metropolis-Hastings algorithm is an MCMC method for generating a set of random samples from some probability distribution, which is well-suited to the dimensionality (on the order of about 10) of the probability distribution being probed. We describe the Metropolis-Hastings algorithm briefly:

1. Choose an initial point to start with, say $\boldsymbol{\theta}_n$ - this is based on the central values for each of the parameters in the initial input parameter file.
2. Use a proposal distribution, $q(\boldsymbol{\theta}_n, \boldsymbol{\theta}_{n+1})$, to ‘propose’ a point in the likelihood region, the ‘target distribution’, to sample next. The proposal distribution will just help to generate samples.
3. Accept the proposed new point to ‘jump’ to with probability(Lewis & Bridle, 2002)

$$\alpha(\boldsymbol{\theta}_n, \boldsymbol{\theta}_{n+1}) = \min \left\{ 1, \frac{P(\boldsymbol{\theta}_{n+1})q(\boldsymbol{\theta}_{n+1}, \boldsymbol{\theta}_n)}{P(\boldsymbol{\theta}_n)q(\boldsymbol{\theta}_n, \boldsymbol{\theta}_{n+1})} \right\},$$

where the transition probability is

$$T(\boldsymbol{\theta}_n, \boldsymbol{\theta}_{n+1}) = \alpha(\boldsymbol{\theta}_n, \boldsymbol{\theta}_{n+1})q(\boldsymbol{\theta}_n, \boldsymbol{\theta}_{n+1}).$$

We did not assume that the initial sample point starts out at or near the equilibrium region in parameter space, i.e. the chain *burns in* to equilibrium. To this end, we accounted for the burn-in period by discarding the first 20% of the MCMC chains to ensure that the samples came from the posterior distribution.

5.1.2 BOBYQA

BOBYQA (J. D. Powell, 2009) is an iterative algorithm that will eventually yield the values of the parameters corresponding to the maximum likelihood. This will work for hundreds of parameters, however, BOBYQA requires that the calculated likelihood at each ‘step’ be a valid number for every point in parameter space. For example, there were many instances whereby the algorithm stopped because after 400 samples where the corresponding region of parameter space returned a (numerical) zero likelihood. The associated error message is

```
1 Out of range finding H0: 1.040850
Warning: Minimizer does not currently properly support non-boundary LogZero rej ec-
tions
```

BOBYQA works by starting at a point in parameter space, dictated by the central values for the parameters in the initial input parameter file (.ini extension), then ‘exploring’ the likelihood space and finding the maximum likelihood through iteration. Once the parameter values converge to

within some abstract parameter space radius, the algorithm stops. Using a sensible proposal matrix helps speed up convergence.

Since BOBYQA usually finds the best-fit values much faster than Metropolis-Hastings, we used BOBYQA for the bulk of the parameter search. Finally, Metropolis-Hastings was used to refine the guess, give error estimates, and also generate triangle plots (using `GetDist`).

5.2 Methodology

Here, we will use `CosmoMC` to carry out parameter estimation. In particular, we will look at the best fit cosmological parameters that correspond to (almost) zero dark matter, and see how this affects the angular power spectrum.

Originally, we intended to find the best fit value for $\Omega_c h^2 = 0$ right away, however this led to `CAMB` not being able to easily calculate the best fit C_l values, with the output file returning

```
0 WARNING: FindBestFit did not converge
Best-fit results:
Not allocated theory!!!
```

The key problem is that setting $\Omega_c h^2 = 0$ sets the likelihood towards infinity at the ‘concordance point’. We need to ‘step’ towards this limit. Let us say that for the Metropolis-Hastings algorithm, we start at some sample point in the likelihood region, corresponding to the original best fit set of cosmological parameters (Λ CDM). With the Planck High- l temperature and lowTEB likelihoods, this set is

Parameter	Value
$\Omega_b h^2$	0.02222 ± 0.00023
$\Omega_c h^2$	0.1197 ± 0.0022
$H_0(\text{km s}^{-1} \text{Mpc}^{-1})$	67.31 ± 0.96
τ	0.078 ± 0.019
$\ln(10^{10} A_s)$	3.089 ± 0.036
n_s	0.9655 ± 0.062

Table 5.1: Best-fit cosmological parameters from Planck

The Metropolis-Hastings algorithm will be able to proceed if the next proposed sample point is not in some region of non-zero likelihood. This also means choosing a proposal distribution and parameter step size which is not too wide or large so that the target distribution is no longer sampled, but not too narrow or small such that it does not probe the entire target distribution in a meaningful manner. After many iterations, the parameter values converge around some pre-defined radius of convergence and the algorithm stops.

However, if one starts at say, $\Omega_c h^2 = 0.00005$ right away, the sample point will most likely be in a region of zero likelihood, causing the algorithm to stop and report the error in the box above. To overcome this, one can decrease $\Omega_c h^2$ in ‘steps’. Say we next want to find the corresponding best fit for $\Omega_c h^2 = 0.1100$ (i.e. a decrease in $\Omega_c h^2 = 0.01$). After running the algorithm, we are given a set of best-fit parameter values which will inform our decision for the next input sample point (with $\Omega_c h^2 = 0.1000$). This goes on until $\Omega_c h^2 = 0.00005$, effectively ‘0 dark matter’. There is nothing rigorous about this method, but it serves to provide a relatively quick way to

find sensible sample points. The task was also alleviated at times by making use of CAMB (in Python) to find a rough ‘best fit’ to the observed CMB angular power spectrum by eye.

This ‘mountain range analysis’ was done using the maximum likelihood routine in BOBYQA (action = 2 in CosmoMC). The final estimation for the parameter values was carried out with the Metropolis-Hastings algorithm (action = 0).

For various scenarios (described below), the step size for reducing $\Omega_c h^2$ was not straightforward. Sometimes $\Omega_c h^2 = 0.01$ was too large, so step sizes of $\Omega_c h^2 = 0.002$ had to be done. Additionally, the runtime for the BOBYQA algorithm ranged from 15 minutes to 40 hours for some parameter values, highlighting the difficulty of the problem. In the next section, we will show one practical example of the implementation of the ‘mountain range’ method described above.

5.3 Minimal Dark Matter

From the arguments above at the start of the section, we know that there are many independent, though indirect, observations of the effects dark matter has on baryonic matter. However, for this project, let us see what happens when we have $\Omega_c h^2 \approx 0$, using the ‘mountain range’ process we described earlier. We simply quote the final results for various scenarios. We make comparisons with respect to the baseline model with parameters in Table 5.1.

In this section, we will use the following Planck likelihoods (not all at once, though High- l TT is always used):

Designation	File name	Description
High- l TT	plik_dx11dr2_HM_v18_TT	Temperature likelihood for $l \geq 30$
Low- l TT	lowl	Temperature likelihood for $l \leq 29$
lowTEB	lowTEB	Temperature and polarization likelihood for $l \leq 29$
lensing	lensing	Lensing likelihood (temperature)

Table 5.2: List of Planck likelihoods used for $\Omega_c h^2 = 0$

In Section 5.3.1 we present an example of the implementation of the ‘mountain range’ process. We only use results in Sections 5.3.2 and 5.3.3 for our analysis.

5.3.1 Example

Here we look at the case where we set $\Omega_K = 0$ (i.e. flat universe), and we have no lensing of the CMB, i.e. in batch2/common.ini (settings),

```
use_nonlinear_lensing = F
CMB_lensing = F
```

We point out that the High- l temperature likelihood and the low- l temperature (only) likelihood (lowl.ini) were used for the ‘mountain range’ analysis example. The final result from the Metropolis-Hastings algorithm used the same likelihoods. In later sections, we use the Planck lowTEB likelihood instead. Again, we emphasise that the ‘mountain range’ analysis serves to provide sensible initial sample points corresponding to $\Omega_c h^2 = 0.00005$ (i.e. very small dark matter content) for the Metropolis-Hastings run. Let us see how this works in practice in Table 5.3. In this scenario, we went down in steps of $\Omega_c h^2 = 0.02$.

There are many degeneracies in the baseline Λ CDM model for the CMB angular power spectrum. However, we do know, ceteris paribus, how each parameter affects the CMB angular power spectrum (more below). We used CAMB to inform us (by eye) of the best initial sample point for each value of $\Omega_c h^2$ probed. One might argue that if one knows how reducing the $\Omega_c h^2$ affects the other 5 cosmological parameters and/or the angular power spectrum, surely the problem is trivial. However, this change is not known *a priori* and there is no simple, clear relationship between the change in $\Omega_c h^2$ and how the other parameters change, not to mention possible degeneracies for such a large modification to a key parameter. Thus the ‘mountain range’ analysis is the most effective way of finding the best-fit parameters (and power spectrum) corresponding to $\Omega_c h^2 = 0$.

	$\Omega_c h^2$	$\ln(10^{10} A_s)$	n_s	$\Omega_b h^2$	τ	H_0
Starting values	0.1186	3.062	0.9677	0.02226	0.066	67.81
Best fit from BOBYQA	0.1275	3.036	0.9392	0.02020	0.046	62.48
Starting values	0.1000	2.95	0.9500	0.02000	0.050	75.00
Best fit from BOBYQA	–	3.19	1.0057	0.02187	0.156	75.19
Starting values	0.0800	3.35	1.1000	0.02300	0.250	90.00
Best fit from BOBYQA	–	3.45	1.0753	0.02324	0.315	87.37
Starting values	0.0600	3.60	1.1500	0.02500	0.400	110.00
Best fit from BOBYQA	–	3.69	1.1614	0.02484	0.457	103.54
Starting values	0.0400	4.05	1.2500	0.02500	0.600	110.00
Best fit from BOBYQA	–	3.99	1.2660	0.02618	0.632	126.06
Starting values	0.0200	4.30	1.3500	0.02700	0.800	150.00
Best fit from BOBYQA	–	4.42	1.3925	0.02573	0.878	161.74
Starting values	0.00005	4.60	1.4500	0.02500	0.960	240.00
Best fit from BOBYQA	–	5.20	1.5750	0.02091	1.289	256.26

Table 5.3: Illustrating the ‘mountain range’ analysis

We note that in this case, we have

$$\Omega_c = \frac{\Omega_c h^2}{h^2} = \frac{0.00005}{\left(\frac{256.26}{100}\right)^2} \approx 7.61 \times 10^{-6},$$

which is essentially 0. Finally, we use the Metropolis-Hastings algorithm to get a refined set of parameter values and corresponding errors, and also obtain triangle plots. Let us now look at the best-fit parameters, corresponding power spectrum and the triangle plot.

Parameter	Value
$\ln(10^{10} A_s)$	5.24 ± 0.06
n_s	1.576 ± 0.004
$\Omega_b h^2$	0.0209 ± 0.0003
τ	1.31 ± 0.03
H_0	256.3 ± 1.5
-ln(likelihood)	4586.8380
χ^2	9173.6760

Table 5.4: Best-fit cosmological parameters to Planck data with no lensing and $\Omega_c h^2 = 0.00005$

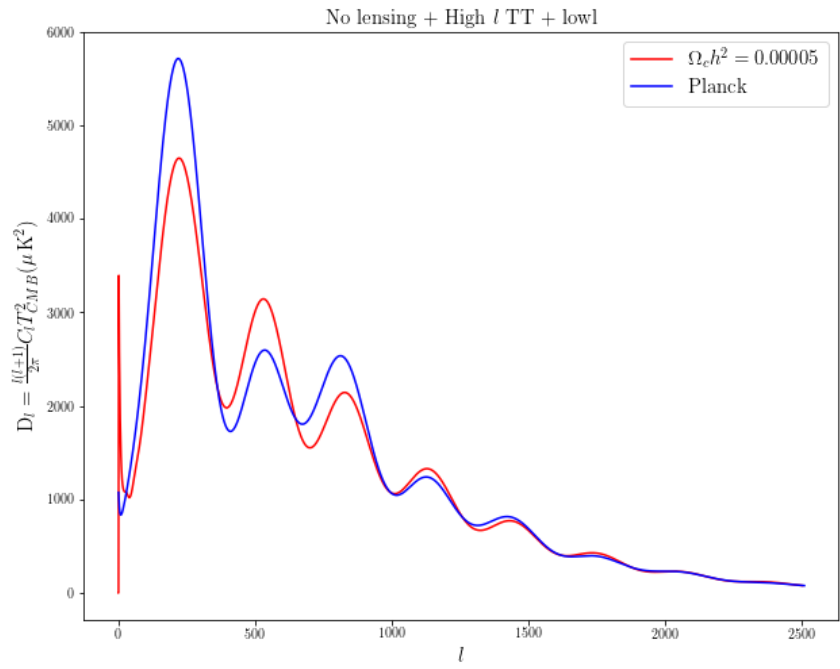


Figure 5.1: Comparing $\Omega_c h^2 = 0.00005$ and Planck best fit power spectrum for no lensing

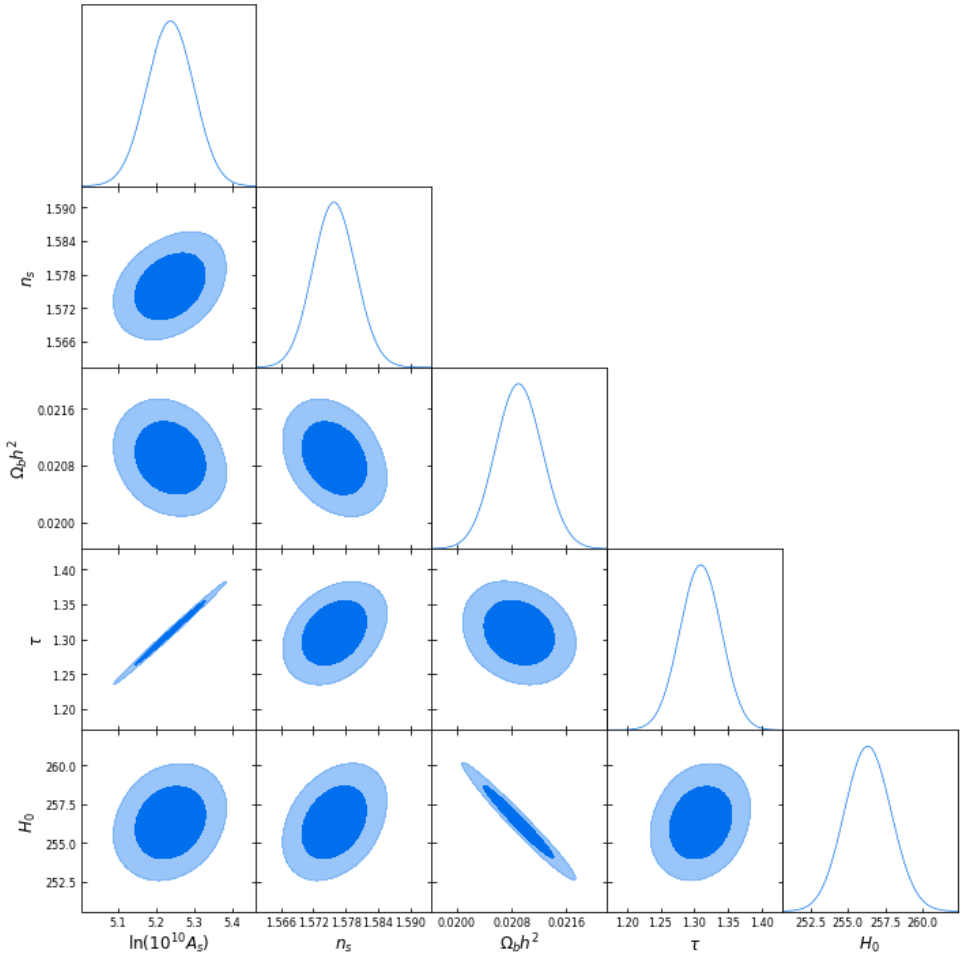


Figure 5.2: Triangle plot for $\Omega_c h^2 = 0.00005$ and no lensing

Comparing the values from Tables 5.3 and 5.4, we can see how the ‘mountain range’ analysis refines our guess for the initial sample point.

5.3.2 Lensing + TEB

Let us now look at the case where $\Omega_K = 0$, and we have that the CMB is lensed, but instead of the low- l temperature likelihood, we use the low- l temperature and polarization likelihood lowTEB. Having the polarisation likelihood allows us to put constraints on the polarisation of the CMB and on the reionisation history. The inclusion of lensing suppresses structure in the CMB angular power spectrum, but it does not have a significant impact on our analyses. The best-fit cosmological parameters are:

Parameter	Value
$\ln(10^{10} A_s)$	4.84 ± 0.05
n_s	1.566 ± 0.004
$\Omega_b h^2$	0.0240 ± 0.0004
τ	1.11 ± 0.03
H_0	242.1 ± 1.2
-ln(likelihood)	10577.2400
χ^2	21154.4800

Table 5.5: Best-fit cosmological parameters to Planck data with lensing and $\Omega_c h^2 = 0.00005$ and lowl TEB likelihood

Here we have that

$$\Omega_c = \frac{\Omega_c h^2}{h^2} = \frac{0.00005}{\left(\frac{242.1}{100}\right)^2} \approx 8.53 \times 10^{-6}.$$

The associated power spectrum and triangle plot are as follows

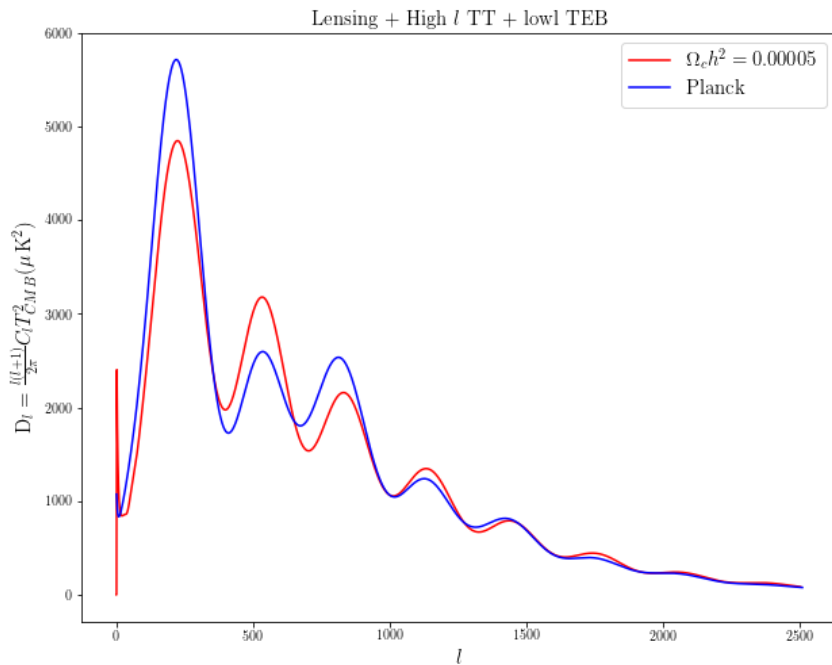


Figure 5.3: Comparing $\Omega_c h^2 = 0.00005$ and Planck best fit power spectrum for lensing

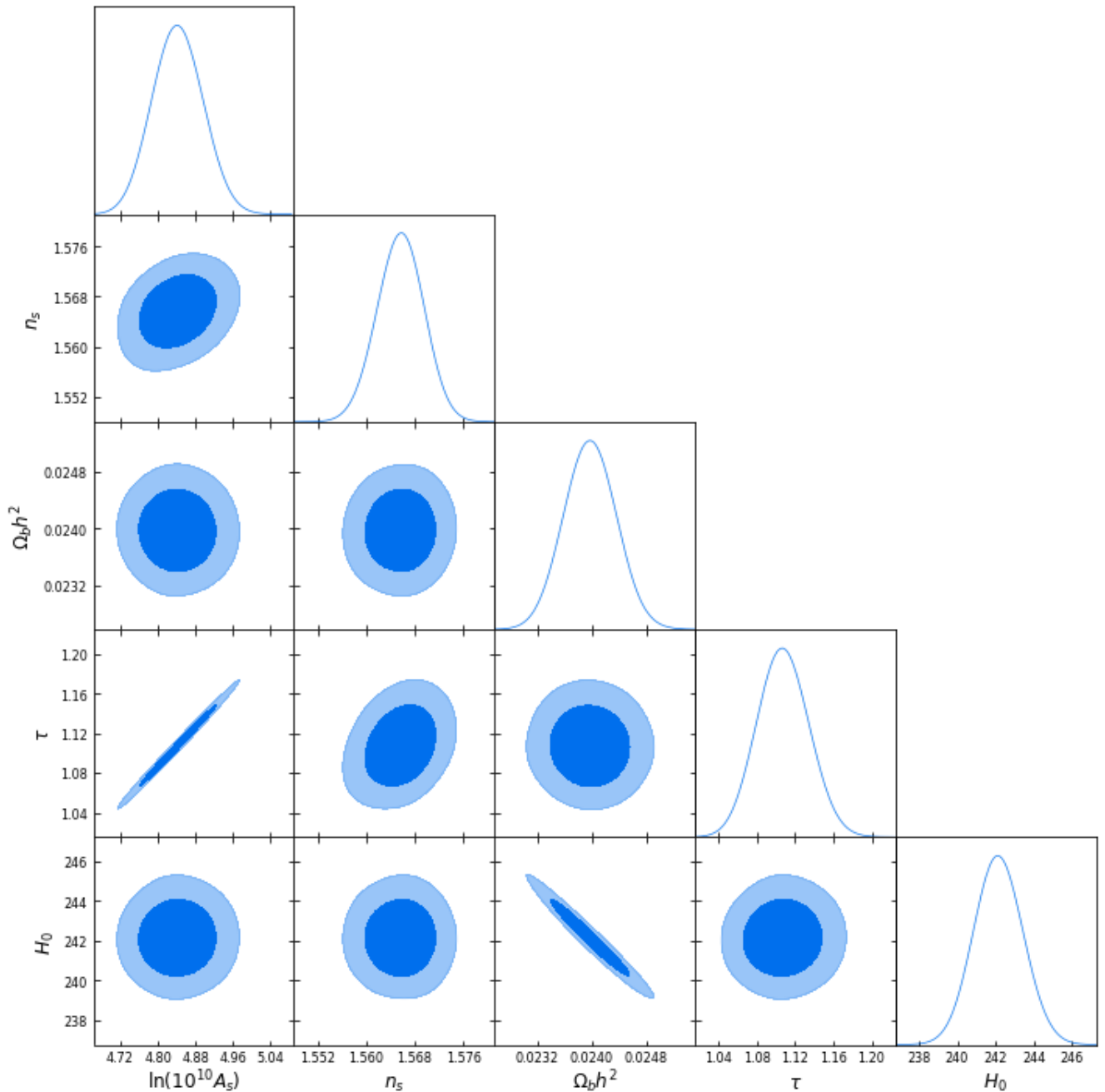


Figure 5.4: Triangle plot for $\Omega_c h^2 = 0.00005$ and lensing and lowl TEB likelihood

5.3.3 Fixed H_0 + Lensing + TEB

Let us now look at the case where Ω_K is varied, H_0 is fixed, and we have lensing of the CMB. We use the low- l temperature and polarization likelihood lowTEB here. The best-fit cosmological parameters are:

Parameter	Value
$\ln(10^{10} A_s)$	5.60 ± 0.04
n_s	1.574 ± 0.004
$\Omega_b h^2$	0.01772 ± 0.00007
τ	1.49 ± 0.02
H_0	67.10 ± 0.11
Ω_K	-0.0516 ± 0.0002
-ln(likelihood)	10749.6900
χ^2	21499.3800

Table 5.6: Best-fit cosmological parameters to Planck data with lensing and $\Omega_c h^2 = 0.00005$ and lowl TEB likelihood

Here we have that

$$\Omega_c = \frac{\Omega_c h^2}{h^2} = \frac{0.00005}{\left(\frac{67.10}{100}\right)^2} \approx 1.11 \times 10^{-4}.$$

The associated power spectrum and triangle plot are as follows

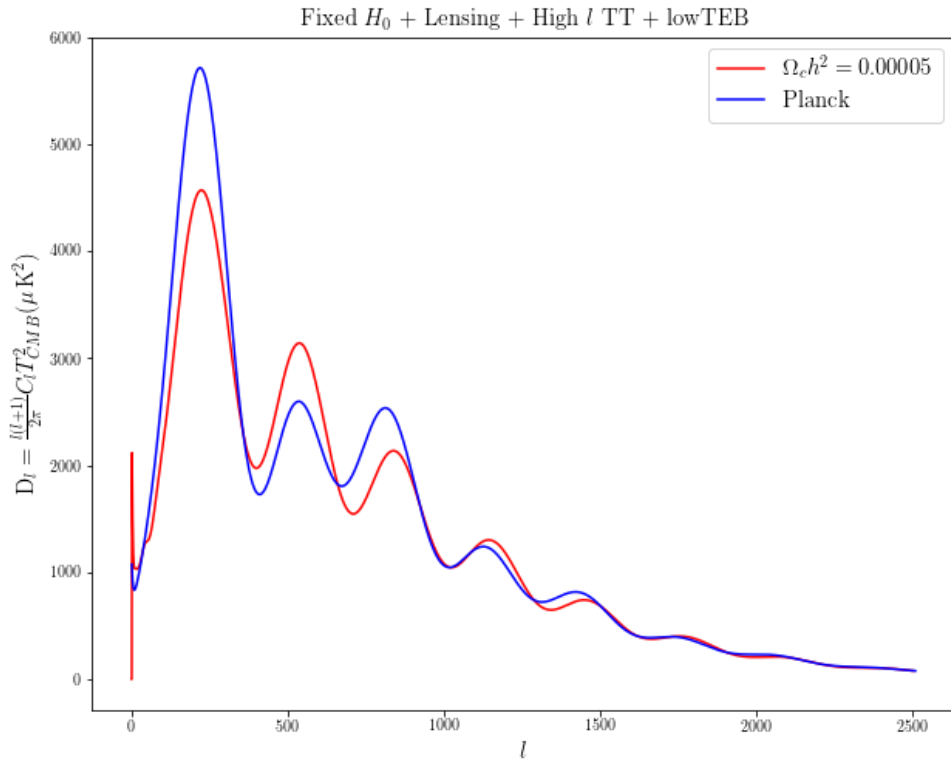


Figure 5.5: Comparing $\Omega_c h^2 = 0.00005$ and Planck best fit power spectrum for lensing

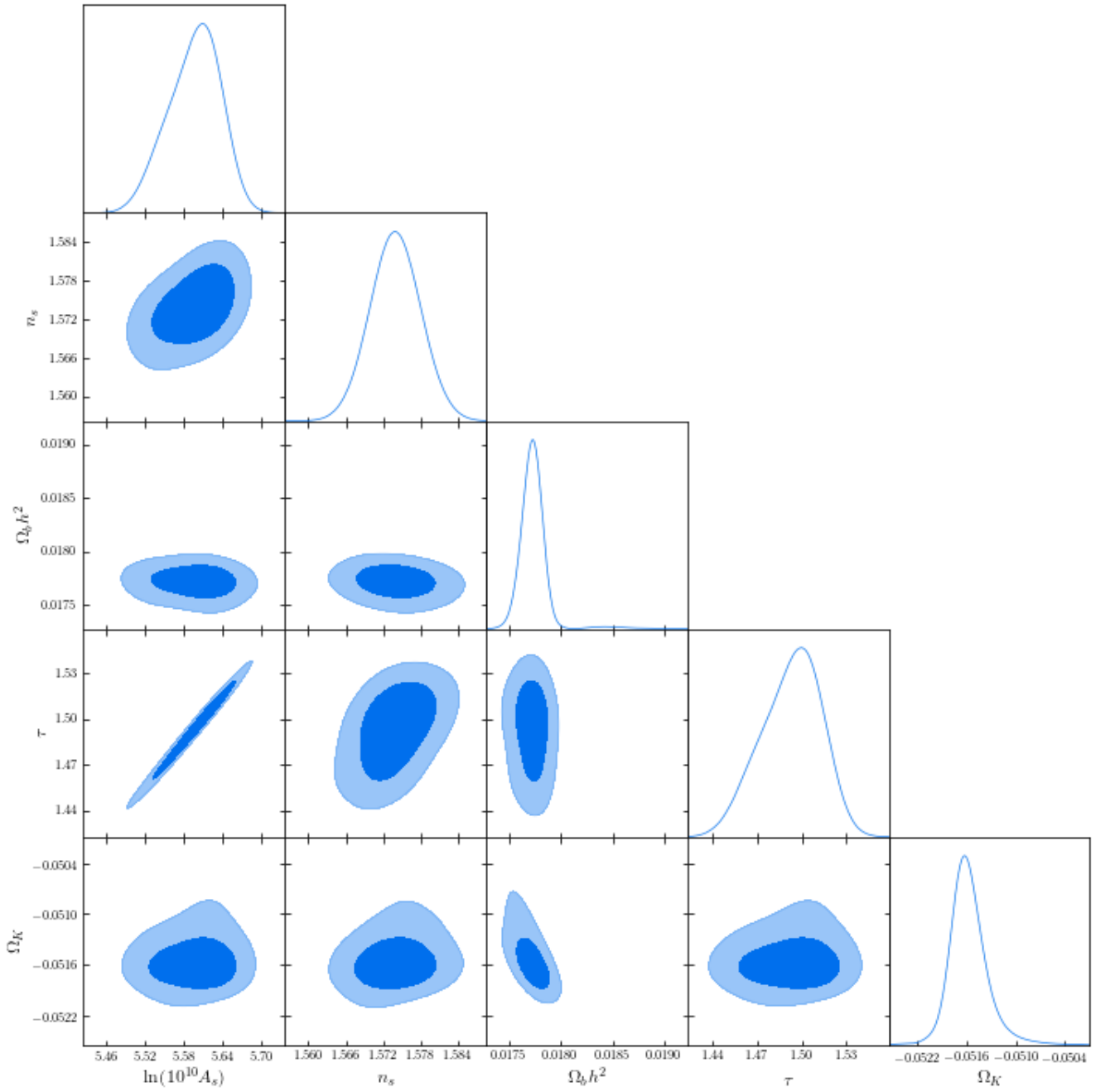


Figure 5.6: Triangle plot for $\Omega_c h^2 = 0.00005$ and lensing and low TEB likelihood with fixed H_0

We note that we cannot actually *fix* H_0 , but we can only restrict it to a very small range, between $67 \text{ km s}^{-1} \text{ Mpc}^{-1}$ and $69 \text{ km s}^{-1} \text{ Mpc}^{-1}$. However, these values are within 1σ of the measured values for all different likelihood combinations in the 2015 Planck analysis (Planck Collaboration, Ade, P. A. R., et al., 2016).

5.4 Discussion

Putting it altogether, we get

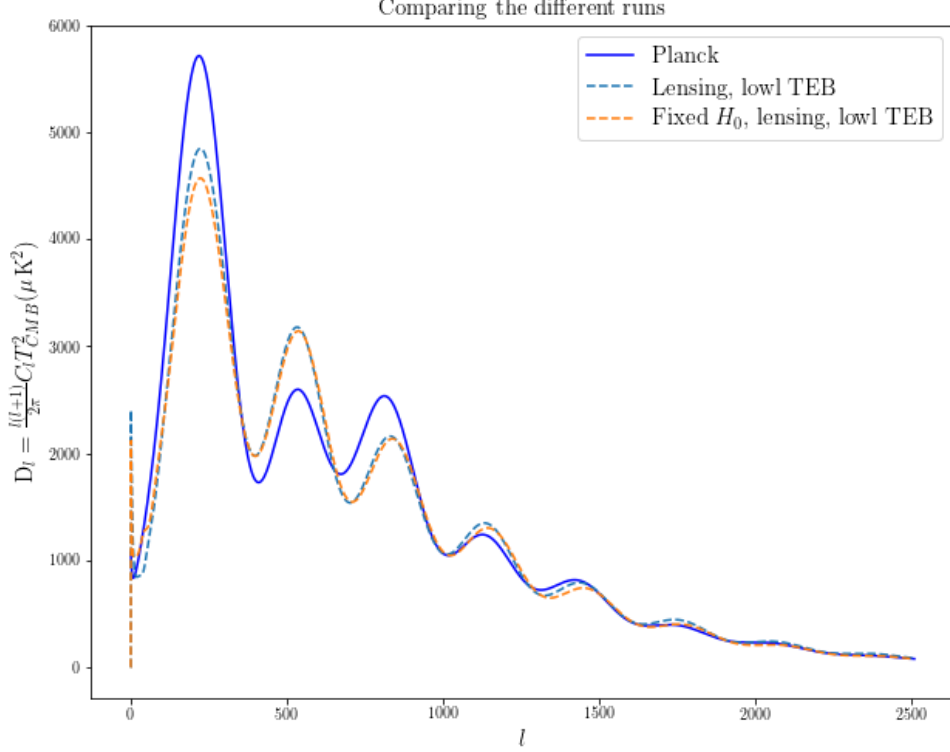


Figure 5.7: Comparing all the angular power spectra

Parameter	Lensing TEB	Fixed H_0 Lensing TEB
$\ln(10^{10} A_s)$	4.84	5.60
n_s	1.566	1.574
$\Omega_b h^2$	0.0240	0.01772
τ	1.11	1.49
H_0	242.1	67.10
Ω_K	0.0	-0.0516

Table 5.7: Summary of the best-fit values for the cosmological parameters (without the uncertainties)

In this section, we do not explicitly specify the cosmological prior ranges used for parameter estimation as the range varies depending on the value of $\Omega_c h^2$. However, our choices of the prior *do not* affect parameter estimation as long as they are wide enough so that regions of nontrivial likelihood are explored (Easther & Peiris, 2012).

The most prominent thing we see immediately from Fig. 5.7 is that the odd-numbered peaks are weakened and the even-numbered peaks are enhanced. This is the case with all the scenarios explored in general. This can be explained qualitatively. However, we should first point out that these are the best fits to the Planck CMB data (i.e. the likelihoods) *in the absence of dark matter*. This investigation demonstrates the extent to which the dark matter is necessary to

explain the CMB angular power spectrum. Physically, the inclusion of dark matter corresponds to the existence of deeper gravitational potential wells in the baryon-photon fluid in which compression (odd peaks) is enhanced and rarefaction (even peaks) is suppressed, relative to a dark matter-less universe.

We could not bring $\Omega_c h^2$ to exactly 0 because there were initial conditions set in CAMB that assumed non-zero dark matter, however we proceeded with the analysis using $\Omega_c h^2 = 0.00005$. Firstly, we see in general that $\ln(10^{10} A_s)$ has increased, i.e. the amplitude of the scalar perturbations is larger. From Fig. 3.4, we would expect the angular power spectrum to be shifted vertically upwards, i.e. temperature fluctuations are larger on all scales (though we do have not the same magnitude of increase for all scales - this effect is more prominent at larger angular scales compared to at smaller angular scales). However, this can be offset by the larger value of τ , the reionization optical depth, which parameterises the Thomson scattering of CMB photons off electrons (described prior). This relates to the temperature fluctuations by

$$\Delta T = \frac{\delta T}{T_{\text{CMB}}} \propto e^{-\tau};$$

we can relate this to the intensity (of CMB photons) by

$$I_{\text{new}} = I_0(1 + f(\theta)e^{-\tau})$$

where $f(\theta)$ is some direction-dependent function. So for a larger value of τ , there is a correspondingly larger scattering rate of the CMB photons, which leads to a ‘damping’ of the temperature fluctuations on all (angular) scales.

Looking at n_s , we see from Table 5.7 that the best-fit values for n_s are around 1.6 for all scenarios. From Figure 3.5, this would translate to a suppression of the power spectrum at larger angular scales and a slight enhancement on the smaller angular scales (spectrum is ‘pivoting’).

We know how $\Omega_b h^2$ changes the angular power spectrum. A reduction in $\Omega_b h^2$ (hence baryon content) translates to a suppression in the temperature fluctuations for the odd peaks (less compression), and a relatively lesser degree of suppression of the even peaks (lower rarefaction).

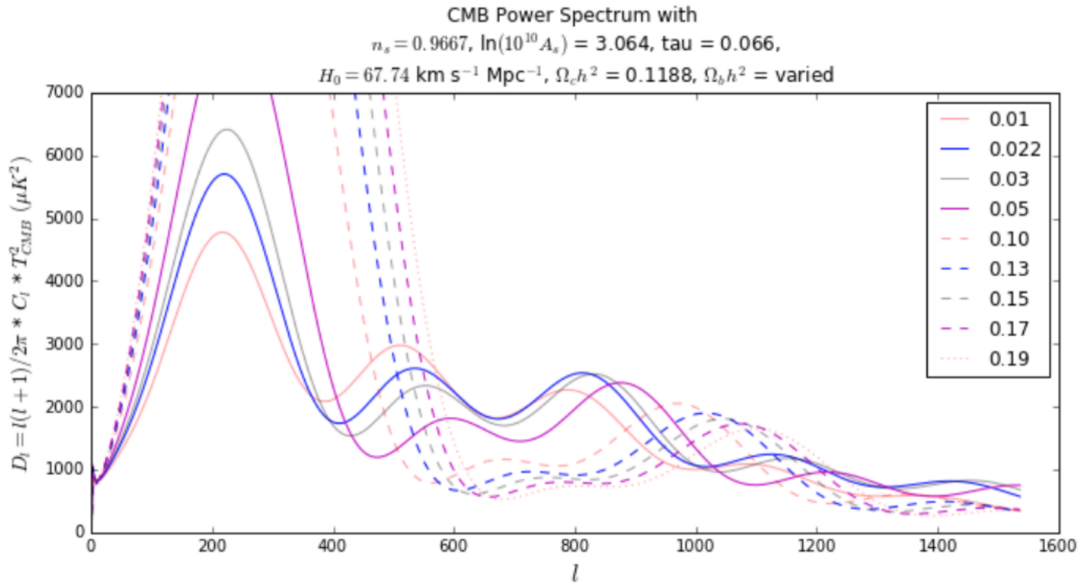


Figure 5.8: Changing $\Omega_b h^2$

Let us look how the cosmological parameters affect the location of the peaks. We go back to the expression we had for the Hubble parameter in Eq. 2.3,

$$H(z) = H_0 \sqrt{\Omega_M(1+z)^3 + \Omega_R(1+z)^4 + \Omega_\Lambda}.$$

The comoving redshift-distance relation is then from Eq. 2.4,

$$d = \frac{c}{a_0 H_0} \int_0^z \frac{dz'}{\sqrt{\Omega_M(1+z')^3 + \Omega_R(1+z')^4 + \Omega_\Lambda}}. \quad (5.1)$$

We can then define θ , the angular size of some given structure (in CMB),

$$\theta = \frac{s}{d_A},$$

where s is the sound horizon length (i.e. distance that sound travelled since Big Bang until last scattering), and d_A is the angular diameter distance. d_A can be related to d , where

$$d_A = ad = \frac{ac}{H_0} \int_0^z \frac{dz'}{\sqrt{\Omega_M(1+z')^3 + \Omega_R(1+z')^4 + \Omega_\Lambda}}.$$

We can see a few things from this relation. First, we see that $\theta \propto 1/d_A \propto H_0 \implies \theta \propto H_0$. A larger Hubble constant implies a more rapid expansion, and so as the last scattering surface is fixed, we get a younger universe (age of universe is lower), implying that the CMB is closer. So we would observe a larger temperature fluctuation at larger angular scales (i.e. at lower l). We illustrate this in the figure below.

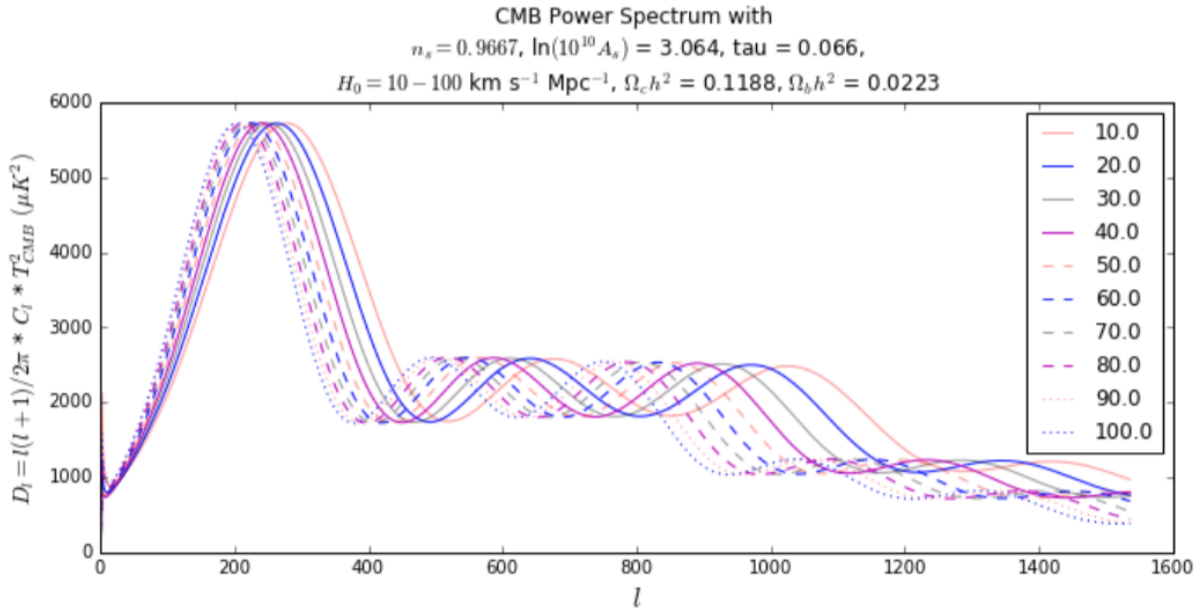


Figure 5.9: Changing H_0

Let us first look at how *just* changing H_0 in the set of parameters from Table 5.3.2 affects the angular power spectrum

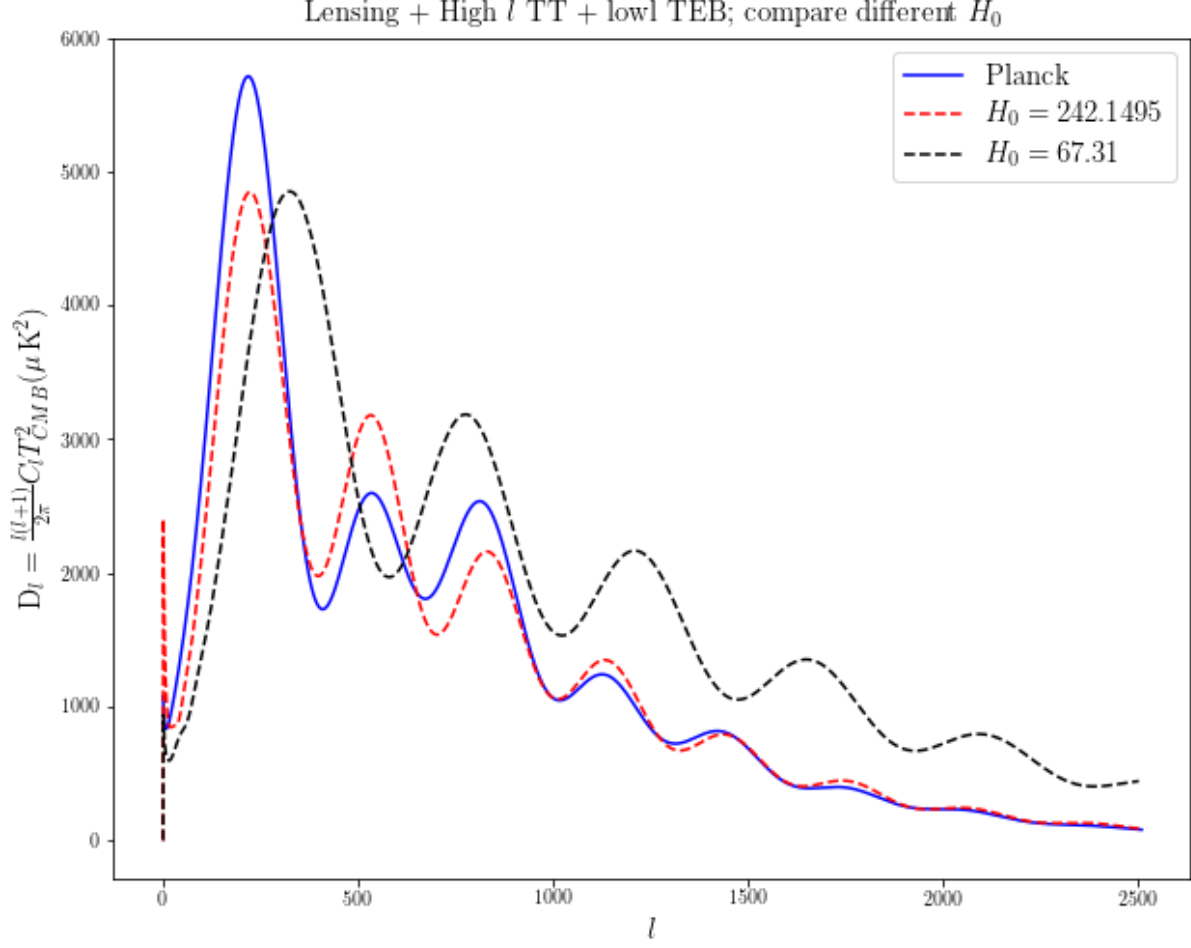


Figure 5.10: Changing H_0 for the case of lensing + High- l TT and low- l TEB

Bringing this altogether, we see that even though increasing A_s leads to more pronounced temperature fluctuations on all scales, the ‘damping’ effects of τ and the tilting of power spectrum from n_s are the main contributors to the lower height of the first peak relative to the Planck best-fit power spectrum. This is also in spite of the fact that the increase in H_0 contributed to larger power in the angular spectrum at larger angular scales (i.e. at lower l).

For the second peak, we see something similar with respect to A_s and τ , to a lesser degree. The scalar spectral index n_s does not change the second peak much, and having an increased H_0 resulted in larger temperature fluctuations. This is reversed for the third peak. A possible future extension to this work would be to deconvolve the degeneracy pertaining to the location of the third peak in particular, where relative to the Planck best fit, it can be seen that the peak is shifted slightly to the right.

Lastly, let us look at the last two cases explored, where H_0 was ‘fixed’. The Planck best fit was $(67.31 \pm 0.96) \text{ km s}^{-1} \text{ Mpc}^{-1}$. In CosmoMC, H_0 was parameterised with θ , the angular scale of the sound horizon. Even if θ was kept fixed, there was some room for H_0 to vary. This means that we could only tighten the bound for H_0 , but not fix it per se. However, we note from Fig. 5.9 that a shift in about $1 \text{ km s}^{-1} \text{ Mpc}^{-1}$ does not change the CMB angular power spectrum much.

The biggest differences pertain to the relatively lowered $\Omega_b h^2$ and consequently, a negative curvature (gave it a prior). We look first at how changing $\Omega_b h^2$ between the best-fit value (for

the model) and the Planck best fit value of $\Omega_b h^2 = 0.02222$ affects the angular power spectrum.

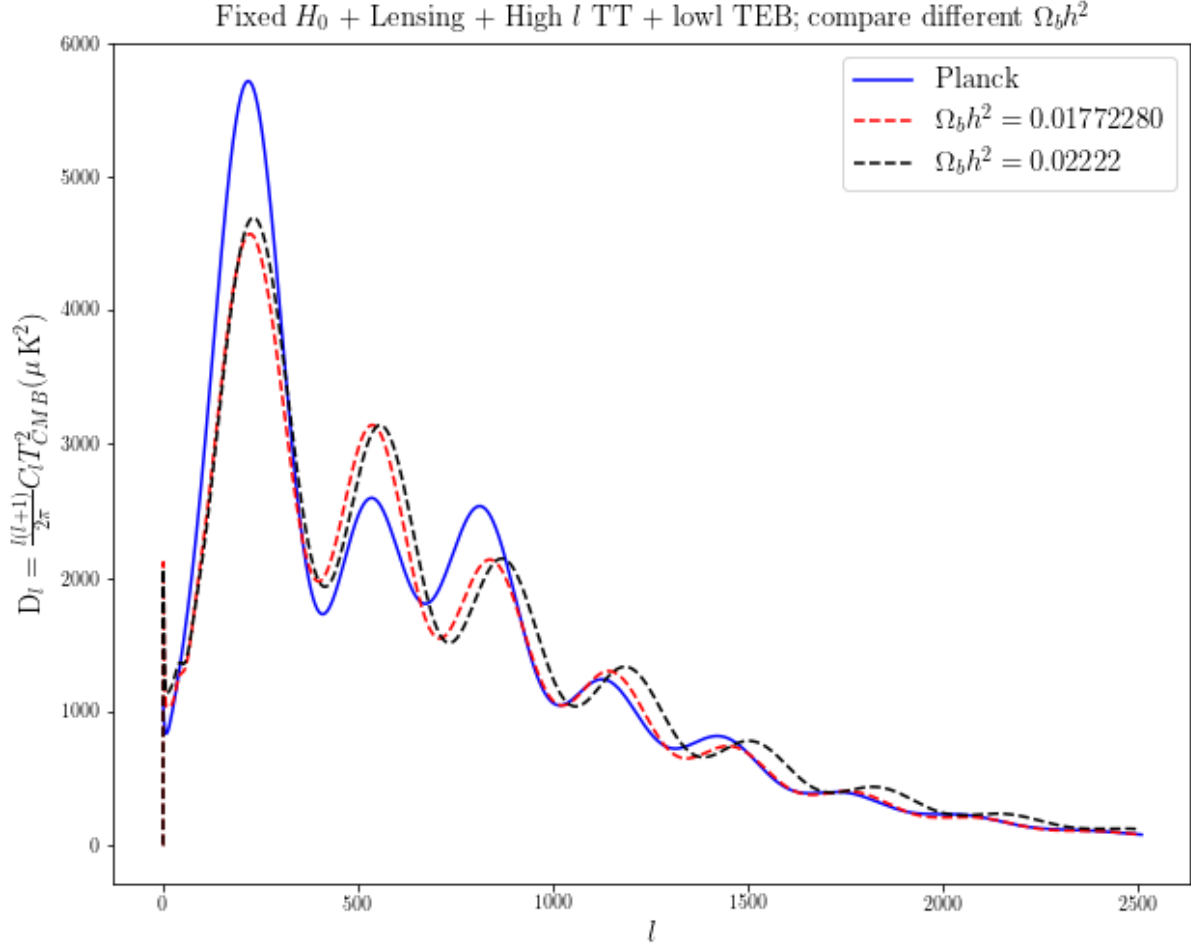


Figure 5.11: Fixed $H_0 +$ Lensing + High- l TT and low- l TEB; changing $\Omega_b h^2$

We see that having the ‘new’ value of $\Omega_b h^2$ shifts the power spectrum to the left slightly, i.e. that at a fixed angular scale, the temperature fluctuations decrease. This does not change the power spectrum much unless one looks at the smaller angular scales (damping tail), but this is beyond the scope of the analysis. Let us explore the differences admitted by introducing the non-zero curvature in the fitting process.

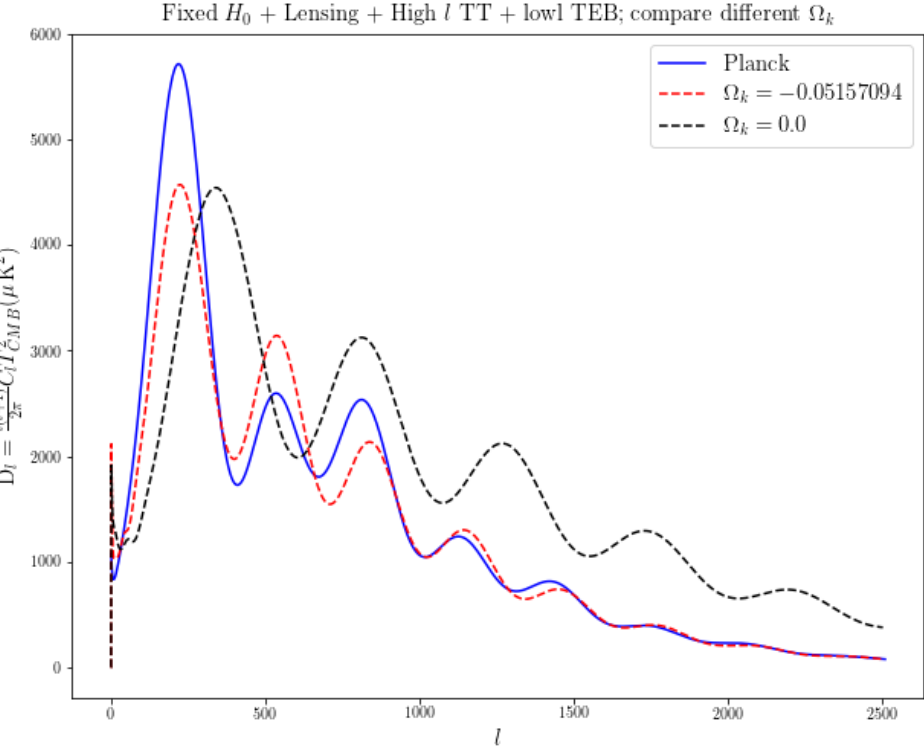


Figure 5.12: Fixed H_0 + Lensing + High- l TT and low- l TEB; changing curvature Ω_k

Fig. 5.12 looks similar to Fig. 5.10. In fact, if we plot the two changes in black over each other, we get

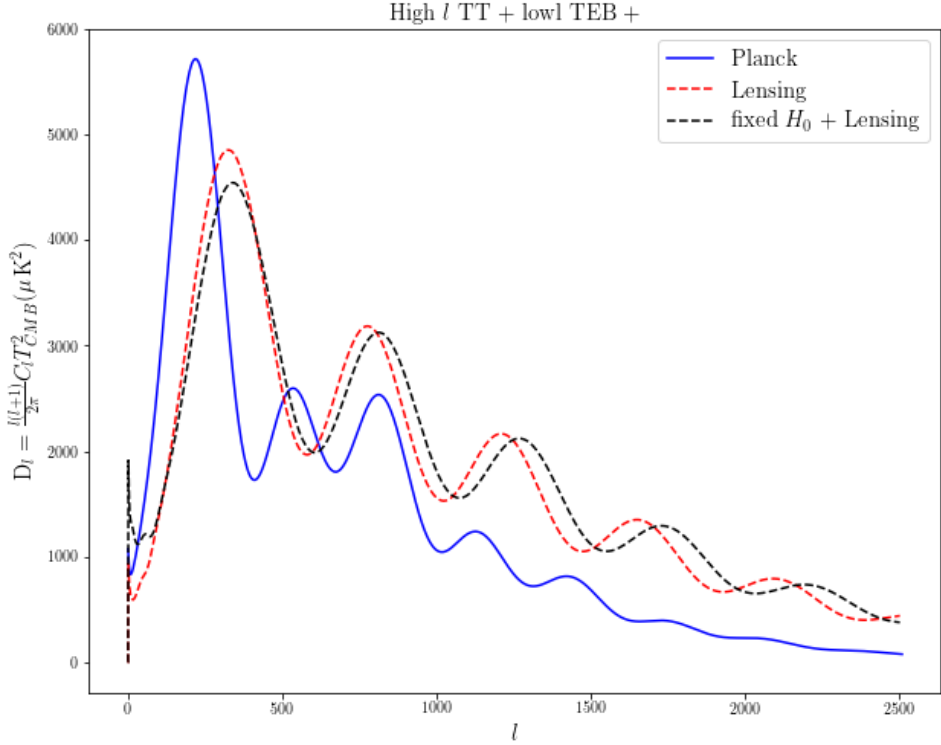


Figure 5.13: Comparing the change in parameters needed for the best fit

There is some difference, but the main idea is similar, where it boils down to adding a $\Omega_K(1+z')^2$ term inside the square root in Eq. 5.1; curvature was ignored previously. However, having a negative curvature (closed universe) would translate to a lower $H(z)$ (i.e. slower expansion rate), so we see an older universe which implies a CMB that is further away. This would translate to, as seen in Fig. 5.12, a shift of the power spectrum to the right, not to the left as was argued for 5.10. Since $\Omega_b h^2$ does not alter the power spectrum much as illustrated in 5.11, the ‘pulling’ of the power spectrum to the left must be dominated by the large value of Ω_Λ . We have deferred discussion of this quantity as it is beyond the scope of this work, but we can briefly mention it.

Ω_Λ parameterises dark energy - the invisible substance in the universe that is purported to be responsible for the current acceleration of the universe (Riess et al., 1998). Actually in our runs, we get that Ω_Λ is close to 1 ($\Omega_\Lambda \approx 0.995$ for non-fixed- H_0 models; $\Omega_\Lambda \approx 1.011$ for fixed- H_0 models, where curvature was negative). The Planck best fit gave $\Omega_\Lambda = 0.6851$. Hence it is possible that this increase in Ω_Λ would have produced a shift in the angular power spectrum to the left.

One last feature that we briefly mention is the very large temperature fluctuation (or power) at the largest angular scales

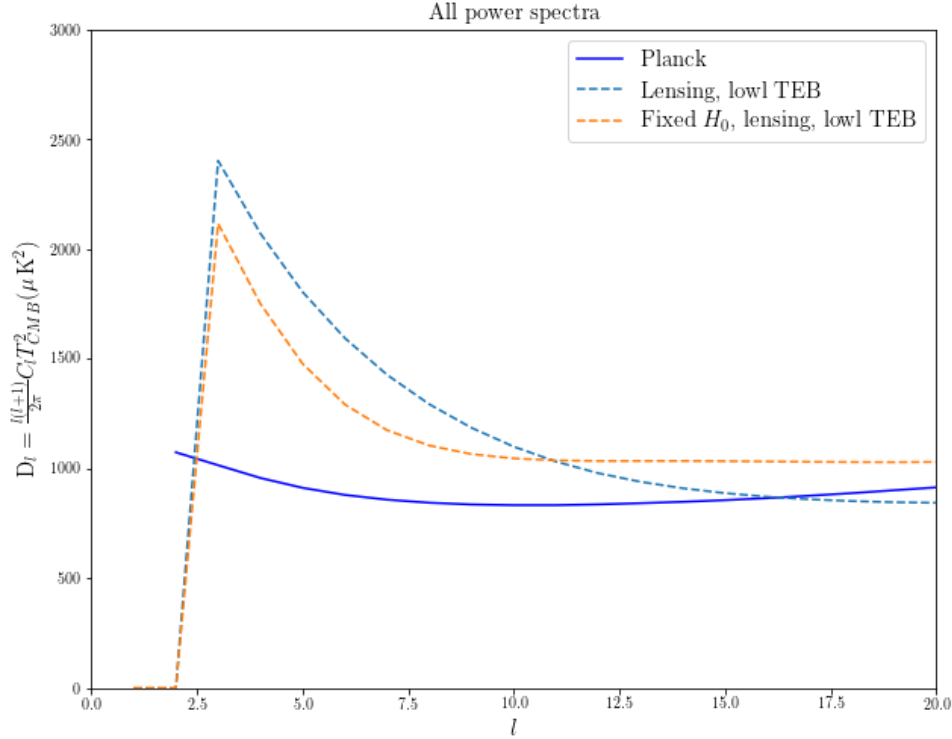


Figure 5.14: Comparing all the angular power spectra for $l \leq 20$

This is thought to be due to the integrated Sachs-Wolfe effect, where the CMB photons are gravitationally redshifted by time-evolving potential wells not caused by matter. This would be the case in a dark-energy dominated universe (or radiation), which is what we have seen here. This reflects what, in part, the angular power spectrum would look like on the largest scales in the very distant future (see Fig. 6.4 of (Lange, 2007)).

Lastly, let us quantitatively examine the improvement of the best fit to Planck data when dark matter is included in the calculation of the CMB angular power spectrum. Figure 3.3 showed the cosmological best fit to Planck data. Figure 5.7 compares the cosmological best fit to the best fit corresponding to $\Omega_c h^2 \approx 0$. We summarise the likelihood and χ^2 ($= -2\ln(\text{likelihood})$)

values below:

	Cosmological best fit	Lensing + TEB	Fixed H_0 + Lensing + TEB
-ln(likelihood)	5636.2161	10577.2400	10749.6900
χ^2	11272.4322	21154.4800	21499.3800

Table 5.8: Comparing χ^2 values for the different best fits to Planck data

We calculate the associated p-value between the cosmological best fit and the best fit when $\Omega_c h^2 \approx 0$, i.e. the probability that the best fit with $\Omega_c h^2 \approx 0$ can explain the Planck data, given that the cosmological best fit is true. The p-value can be calculated using the `stats` module in Python. The module `mpmath` is to deal with the representation of very small floats:

```
mpmath.exp(np.log(stats.distributions.chi2.sf(9882.0478, 70)))
```

where $21154.4800 - 11272.4322 = 9882.0478$ is the difference in χ^2 values and there were 70 degrees of freedom in the calculation for the CMB power spectra. The χ^2 values from the two different models are similar, so we use the χ^2 value for lensing + TEB. Python returns a ‘division by zero’ error; using the code with 7000 degrees of freedom returns a p-value of 3.20×10^{-104} , so we infer that the same calculation with 70 degrees of freedom will return an infinitesimally small number. Therefore there is a drastic improvement in the fit to the Planck data that comes from adding dark matter into the mix. We showed this with a quantitative analysis, a calculation which has not been done before.

The purported alternatives (e.g. modified Newtonian dynamics) to dark matter address the problem from the standpoint of galactic dynamics, which involves non-linear overdensities (particularly for spiral galaxies), star formation-feedback cycles, and non-trivial interactions between the baryonic and reputed dark matter content. The complex interplay of these different factors makes it difficult to deconvolve the effects of dark matter from that of gas dynamics.

On the other hand, the CMB is largely analysed within the regime of linear perturbation theory, and the simple integration of the dark matter hypothesis improves the fit to data at the 10^{100} level and accounts for observed data, leaving no significant residuals or clear discrepancies. In view of this, dark matter clearly possesses consequential predictive power, and suggests that any proposed dark matter alternative (e.g. modified Newtonian dynamics) would have to ‘mimic’ dark matter with a high degree of fidelity in order to match observations.

Chapter 6

Conclusions

In this dissertation, we have looked at two facets of cosmology using the 2015 Planck likelihoods. Firstly, we performed Bayesian evidence calculations for some simple monomial inflaton potentials and the new inflection point inflation model (Musoke & Easter, 2017) with a non-instant reheating scenario. This was an update on the calculations done by (Easter & Peiris, 2012), where we used the Planck likelihoods. Like Planck (Planck Collaboration, Ade, et al., 2016), we have confirmed that

$$V(\phi) = \frac{\lambda}{4}\phi^4$$

is decisively ruled out as the corresponding potential for the inflaton. There is also very strong evidence against

$$V(\phi) = \frac{m^2}{2}\phi^2.$$

It is very likely that the forthcoming final data Planck release will grant further discriminatory power between the inflationary models. We have also supplemented triangle plots to show the joint posterior distributions. Further work can be done in calculating the different evidence ratios arising from adopting contrasting scenarios within the inflection point inflation model framework, which has only been introduced in the literature very recently and grants further exploration.

Secondly, we have investigated the necessity of dark matter in explaining the cosmic microwave background temperature angular power spectrum. To carry out this task, we looked at various scenarios and brought $\Omega_c h^2$ to near zero. However, this was not a straightforward calculation, as CosmoMC will halt if it starts at a point of zero likelihood and does not find a region of a non-trivial likelihood after a finite number of iterations. This is akin to a traveller trying to find a large mountain in the middle of the Pacific Ocean (save Hawaii). In order to facilitate efforts, we employed a ‘mountain range’ analysis, where we made sure the sampler started at a point of non-zero likelihood (i.e. the foothills of a likelihood surface).

This investigation was carried out to highlight the extent to which dark matter is ‘detected’ in the CMB. In particular, many ‘modified gravity’ proposals focus on rotation curves, but spiral galaxies have complex dynamics whereas CMB physics takes place in the linear regime, giving a clean system to analyse. Despite the original motivation, there is very rich physics in studying the CMB and while there are many degeneracies within the Λ CDM cosmological model, it is possible, with the Planck data, to start to deconvolve the degeneracies and get a (at least) qualitative handle on understanding the CMB and what happens if dark matter is not included in the ingredient mix.

We have also carried out a brief quantitative analysis on the improvement of the best fit, to the Planck data, with the addition of dark matter. While the cosmology community understands the physical effects of dark matter on the CMB (and we recovered this above), such a quantitative analysis has not been carried out before. We showed that there is a very low probability ($\ll 10^{-104}$) that the best fit to Planck data with $\Omega_c h^2 \approx 0$ explains the Planck data compared with the cosmological best fit. The inclusion of dark matter in the mix thus improves the fit to the Planck data at the 10^{100} level and leaves no significant residuals. This demonstrates the predictive power of dark matter and puts forward a challenge to dark matter alternatives, such as modified gravity, to account for observations with the high level of fidelity that dark matter exhibits.

Chapter 7

Bibliography

References

- Anderson, L., Aubourg, É., Bailey, S., Beutler, F., Bhardwaj, V., Blanton, M., ... Zhao, G. (2014, June). The clustering of galaxies in the SDSS-III Baryon Oscillation Spectroscopic Survey: baryon acoustic oscillations in the Data Releases 10 and 11 Galaxy samples. *mnras*, *441*, 24–62. doi: 10.1093/mnras/stu523
- Baumann, D. (2009, July). TASI Lectures on Inflation. *ArXiv e-prints* (0907.5424).
- Baumann, D. (2014). Cosmology: Part III Mathematical Tripos. Retrieved from <http://www.damtp.cam.ac.uk/user/db275/Cosmology/Lectures.pdf>
- Bezrukov, F. (2013, November). The Higgs field as an inflaton. *Classical and Quantum Gravity*, *30*(21), 214001. doi: 10.1088/0264-9381/30/21/214001
- BICEP2 Collaboration, Keck Array Collaboration, Ade, P., Ahmed, Z., Aikin, R., Alexander, K., ... Yoon, K. (2016, January). Improved Constraints on Cosmology and Foregrounds from BICEP2 and Keck Array Cosmic Microwave Background Data with Inclusion of 95 GHz Band. *Physical Review Letters*, *116*(3), 031302. doi: 10.1103/PhysRevLett.116.031302
- BICEP2/Keck Collaboration, Planck Collaboration, Ade, P., Aghanim, N., Ahmed, Z., Aikin, R., ... et al. (2015, March). Joint Analysis of BICEP2/Keck Array and Planck Data. *Physical Review Letters*, *114*(10), 101301. doi: 10.1103/PhysRevLett.114.101301
- Cardoso, J.-F., Le Jeune, M., Delabrouille, J., Betoule, M., & Patanchon, G. (2008, November). Component separation with flexible models - application to multichannel astrophysical observations. *IEEE Journal of Selected Topics in Signal Processing*, *2*, 735–746. doi: 10.1109/JSTSP.2008.2005346
- Demozzi, V., & Ringeval, C. (2012, May). Reheating constraints in inflationary magnetogenesis. *jcap*, *5*, 009. doi: 10.1088/1475-7516/2012/05/009
- Easther, R., Flauger, R., & Gilmore, J. B. (2011, April). Delayed reheating and the breakdown of coherent oscillations. *jcap*, *4*, 027. doi: 10.1088/1475-7516/2011/04/027
- Easther, R., & Peiris, H. V. (2012, May). Bayesian analysis of inflation. ii. model selection and constraints on reheating. *Phys. Rev. D*, *85*, 103533. Retrieved from <https://link.aps.org/doi/10.1103/PhysRevD.85.103533> doi: 10.1103/PhysRevD.85.103533
- Fixsen, D. J., Cheng, E. S., Gales, J. M., Mather, J. C., Shafer, R. A., & Wright, E. L. (1996, dec). The Cosmic Microwave Background Spectrum from the Full COBE FIRAS Data Set. *Astrophysical Journal*, *473*, 576. doi: 10.1086/178173
- Guth, A. (1997). *The inflationary universe*. Basic Books. Retrieved from <https://books.google.co.nz/books?id=7toILLsQtIOC>

- Guth, A. H. (1981, Jan). Inflationary universe: A possible solution to the horizon and flatness problems. *Phys. Rev. D*, *23*, 347-356. Retrieved from <https://link.aps.org/doi/10.1103/PhysRevD.23.347> doi: 10.1103/PhysRevD.23.347
- Handley, W., Hobson, M., & Lasenby, A. (2015, November). POLYCHORD: next-generation nested sampling. *mnras*, *453*, 4384-4398. doi: 10.1093/mnras/stv1911
- Hubble, E. (1929, March). A Relation between Distance and Radial Velocity among Extra-Galactic Nebulae. *Proceedings of the National Academy of Science*, *15*, 168-173. doi: 10.1073/pnas.15.3.168
- J. D. Powell, M. (2009, 01). The bobyqa algorithm for bound constrained optimization without derivatives.
- Jeffreys, H. (1998). *The theory of probability*. OUP Oxford. Retrieved from <https://books.google.co.nz/books?id=vh9Act9rtzQC>
- Jones, B., & Wyse, R. (1985, August). The ionisation of the primeval plasma at the time of recombination. *aap*, *149*, 144-150.
- Lange, S. R. (2007). *The time evolution of the cosmic microwave background photosphere* (Thesis).
- Lewis, A., & Bridle, S. (2002, November). Cosmological parameters from CMB and other data: A Monte Carlo approach. *prd*, *66*(10), 103511. doi: 10.1103/PhysRevD.66.103511
- Lewis, A., Challinor, A., & Lasenby, A. (2000, August). Efficient Computation of Cosmic Microwave Background Anisotropies in Closed Friedmann-Robertson-Walker Models. *apj*, *538*, 473-476. doi: 10.1086/309179
- Liddle, A., & Lyth, D. (2000). *Cosmological inflation and large-scale structure*. Cambridge University Press. Retrieved from <https://books.google.co.nz/books?id=XmWauPZSovMC>
- Moore, T. (2012). *A general relativity workbook*. University Science Books. Retrieved from <https://books.google.co.nz/books?id=L-CAMAEACAAJ>
- Mortenson, M., Peiris, H., & Easther, R. (2011, February). Bayesian analysis of inflation: Parameter estimation for single field models. *prd*, *83*(4), 043505. doi: 10.1103/PhysRevD.83.043505
- Musoke, N., & Easther, R. (2017, September). Expectations for Inflationary Observables: Simple or Natural? *ArXiv e-prints*.
- Norena, J., Wagner, C., Verde, L., Peiris, H., & Easther, R. (2012, July). Bayesian analysis of inflation. III. Slow roll reconstruction using model selection. *prd*, *86*(2), 023505. doi: 10.1103/PhysRevD.86.023505
- Pan, Z., Knox, L., Mulroe, B., & Narimani, A. (2016, July). Cosmic microwave background acoustic peak locations. *mnras*, *459*, 2513-2524. doi: 10.1093/mnras/stw833
- Planck Collaboration, Adam, R., Ade, P., Aghanim, N., Akrami, Y., Alves, M., ... et al. (2016, September). Planck 2015 results. I. Overview of products and scientific results. *aap*, *594*, A1. doi: 10.1051/0004-6361/201527101
- Planck Collaboration, Adam, R., Ade, P., Aghanim, N., Arnaud, M., Ashdown, M., ... et al. (2016, September). Planck 2015 results. IX. Diffuse component separation: CMB maps. *aap*, *594*, A9. doi: 10.1051/0004-6361/201525936
- Planck Collaboration, Ade, P., Aghanim, N., Armitage-Caplan, C., Arnaud, M., Ashdown, M., ... et al. (2014, November). Planck 2013 results. XV. CMB power spectra and likelihood. *aap*, *571*, A15. doi: 10.1051/0004-6361/201321573
- Planck Collaboration, Ade, P., Aghanim, N., Arnaud, M., Arroja, F., Ashdown, M., ... et al. (2016, September). Planck 2015 results. XX. Constraints on inflation. *aap*, *594*, A20. doi: 10.1051/0004-6361/201525898
- Planck Collaboration, Ade, P. A. R., Aghanim, N., Arnaud, M., Ashdown, M., Aumont, J., ... Banday, A. J. (2016, October). Planck 2015 results - xiii. cosmological parameters. *Astronomy and Astrophysics*, *594*, A13. Retrieved from <https://doi.org/10.1051/0004-6361/201525830> doi: 10.1051/0004-6361/201525830

- Planck Collaboration, Aghanim, N., Arnaud, M., Ashdown, M., Aumont, J., Baccigalupi, C., ... et al. (2016a, September). Planck 2015 results. XI. CMB power spectra, likelihoods, and robustness of parameters. *aap*, *594*, A11. doi: 10.1051/0004-6361/201526926
- Planck Collaboration, Aghanim, N., Arnaud, M., Ashdown, M., Aumont, J., Baccigalupi, C., ... et al. (2016b, September). Planck 2015 results. XXII. A map of the thermal Sunyaev-Zeldovich effect. *aap*, *594*, A22. doi: 10.1051/0004-6361/201525826
- Reid, D., Kittell, D., Arszenov, E., & Thompson, G. (2002, September). The picture of our universe: A view from modern cosmology. *ArXiv Astrophysics e-prints*.
- Riess, A., Filippenko, A., Challis, P., Clocchiatti, A., Diercks, A., Garnavich, P., ... Tonry, J. (1998, September). Observational Evidence from Supernovae for an Accelerating Universe and a Cosmological Constant. *aj*, *116*, 1009-1038. doi: 10.1086/300499
- Rubin, V. C., Ford, W., Jr., & Thonnard, N. (1980, June). Rotational properties of 21 SC galaxies with a large range of luminosities and radii, from NGC 4605 /R = 4kpc/ to UGC 2885 /R = 122 kpc/. *apj*, *238*, 471-487. doi: 10.1086/158003
- Rubin, V. C., & Ford, W. K., Jr. (1970, February). Rotation of the Andromeda Nebula from a Spectroscopic Survey of Emission Regions. *apj*, *159*, 379. doi: 10.1086/150317
- Seljak, U., & Zaldarriaga, M. (1996, October). A Line-of-Sight Integration Approach to Cosmic Microwave Background Anisotropies. *apj*, *469*, 437. doi: 10.1086/177793
- Skilling, J. (2006, 12). Nested sampling for general bayesian computation. *Bayesian Analysis*, *1*(4), 833–859. Retrieved from <https://doi.org/10.1214/06-BA127> doi: 10.1214/06-BA127
- Takahashi, R., Hamana, T., Shirasaki, M., Namikawa, T., Nishimichi, T., Osato, K., & Shiroyama, K. (2017, June). Full-sky Gravitational Lensing Simulation for Large-area Galaxy Surveys and Cosmic Microwave Background Experiments. *ArXiv e-prints*.
- Tegmark, M. (1997, May). How to measure CMB power spectra without losing information. *prd*, *55*, 5895-5907. doi: 10.1103/PhysRevD.55.5895
- Tegmark, M., & de Oliveira-Costa, A. (2001, September). How to measure CMB polarization power spectra without losing information. *prd*, *64*(6), 063001. doi: 10.1103/PhysRevD.64.063001
- Trotta, R. (2017, January). Bayesian Methods in Cosmology. *ArXiv e-prints*.
- Wehus, I., Ackerman, L., Eriksen, H., & Groeneboom, N. (2009, December). The Effect of Asymmetric Beams in the Wilkinson Microwave Anisotropy Probe Experiment. *apj*, *707*, 343-353. doi: 10.1088/0004-637X/707/1/343
- Zwicky, F. (1937, October). On the Masses of Nebulae and of Clusters of Nebulae. *apj*, *86*, 217. doi: 10.1086/143864

Chapter 8

Appendix

8.1 CMB blackbody spectrum

```
from __future__ import division
import matplotlib.pyplot as plt
import numpy as np
import scipy as sp

h = 6.63e-34
c = 299792458
kb = 1.38e-23

### Plotting the CMB blackbody spectrum

#For cmb_blackbody.txt, we have that
#Reference1 = Table 4 of Fixsen et al. 1996 ApJ 473, 576.
#Reference2 = Fixsen & Mather 2002 ApJ 581, 817.
#Column 1 = frequency from Table 4 of Fixsen et al., units = cm^-1
#Column 2 = FIRAS monopole spectrum computed as the sum
#          of a 2.725 K BB spectrum and the
#          residual in column 3, units = MJy/sr
#Column 3 = residual monopole spectrum from Table 4 of Fixsen et al.,
#          units = kJy/sr
#Column 4 = spectrum uncertainty (1-sigma) from Table 4 of Fixsen et al.,
#          units = kJy/sr
#Column 5 = modeled Galaxy spectrum at the Galactic poles from Table 4 of
#          Fixsen et al., units = kJy/sr

input_file = open('cmb_blackbody.txt', 'r')
contents = input_file.read()
contents = contents.split()
input_file.close()

freq = np.array([float(contents[i]) for i in range(12,len(contents)-1,5)])
spectrum = np.array([float(contents[i]) for i in range(13,len(contents)-1,5)])
error = np.array([float(contents[i])/1000 for i in range(15,len(contents)-1,5)])
residual = np.array([float(contents[i])/1000 for i in range(14,len(contents)-1,5)])

theo = spectrum+residual

plt.errorbar(freq,spectrum,yerr=error,fmt='x')
```

```

plt.plot(freq, theo, 'r-')
plt.ylim([0,400])
plt.xlabel('Frequency (cm$^{-1}$)')
plt.ylabel('Intensity (MJy/sr)')
plt.title('Monopole spectrum from FIRAS')
plt.legend(('Planck blackbody', 'data from FIRAS'), loc='best')

```

8.2 Last Scattering Surface

```

from __future__ import division
import numpy as np
import matplotlib
from scipy.optimize import curve_fit

def gaussian(x,a,b,c):
    return a*np.exp(-(x-b)**2/(2*c**2))

plt.figure(figsize=(10,8))

# redshift values to use
z = np.linspace(0,1500,15001)

# approximate photon visibility function by Jones and Wyse 1985
dens = 5.26e-3 * (z/1000)**13.25*np.exp(-0.37*(z/1000)**14.25)
plt.plot(z,dens, 'r-')

# initial guess for the Gaussian parameters
pguess = np.array([0.0045, 1067, 80])

# applying the non-linear curve fitting
p,cov = curve_fit(gaussian,z,dens, p0=pguess)
#output is:
#p[0] - amplitude of Gaussian
#p[1] - where the Gaussian is centralised
#p[2] - the standard deviation

dens_fit = p[0]*np.exp(-(z-p[1])**2/(2*p[2]**2))
plt.plot(z,dens_fit, 'b-')
plt.xlabel('redshift $z$', fontsize=15)
plt.ylabel(r'$e^{-\tau} \frac{d\tau}{dz}$', fontsize=15)
plt.title('Photon Visibility Function', fontsize=18)
plt.legend(('Approximation', 'Gaussian Fit'), loc='best', fontsize=15)

### calculating the time difference
c = 3e8
h = 0.6731
error_h = 0.0096
H0 = 100 * 1000/(1e6*3.26*3e8*365*3600*24)
z_95 = p[1] - 2*p[2]
z_5 = p[1] + 2*p[2]
error_z95 = np.sqrt(cov[1][1])
error_z5 = np.sqrt(cov[2][2])

# time difference

```

```

Delta_t = 2/(3*H0*h) * (1/(1+z_95)**(3/2) - 1/(1+z_5)**(3/2))

# in years:
years = Delta_t/(3600*24*365)

#error calculation
dt_dH0 = -2/(3*H0*h)**2 * (1/(1+z_95)**(3/2) - 1/(1+z_5)**(3/2))
dt_dz95 = -1/(H0*h) * 1/(1+z_95)**(5/2)
dt_dz5 = 1/(H0*h) * 1/(1+z_5)**(5/2)

#error in seconds
error = np.sqrt(dt_dH0**2*(error_h*H0)**2 + dt_dz95**2*error_z95**2 +
dt_dz5**2*error_z5**2)

#error in years
error_years = error/(365*24*3600)

```

8.3 Angular Size of Largest Fluctuation

```

import numpy as np
import matplotlib.pyplot as plt

z_pd = 1100 #approximate redshift corresponding to photon decoupling
coeff = np.sqrt(1/(z_pd+1))/np.sqrt(3) #Also Omega_K = 0
k_neg = np.linspace(-1.0,0.0,1001) #Omega_K < 0
k_pos = np.linspace(0.0,1.0,1001) #Omega_K > 0

#calculating the angular size of the largest fluctuation in the
#photon-baryon fluid after photon decoupling
phi_neg = coeff*k_neg/np.sin(k_neg)
phi_pos = coeff*k_pos/np.sinh(k_pos)

plt.figure(figsize=(8,6))
plt.plot(k_neg, phi_neg)
plt.plot(k_pos, phi_pos)
plt.plot(0,coeff, 'rx')
plt.legend((r'$\Omega_K<0$', r'$\Omega_K=0$', r'$\Omega_K>0$'), loc='best',
           fontsize=15)
plt.xlabel(r'$\Omega_K$', fontsize=15)
plt.ylabel(r'$\Delta\phi$ (radians)', fontsize=15)

```

8.4 First Evidence Calculation

Here, we will describe an operational set of code to get one started on running their first evidence calculations.

At the start of the project, one should request an account¹ with the New Zealand eScience Infrastructure², the national computing research infrastructure. This project uses the Pan cluster

¹<https://wiki.auckland.ac.nz/display/CER/Request+an+account>

²<https://www.nesi.org.nz>

(Auckland). Once logged in³, enter into the SandyBridge node (newer infrastructure compared with Westmere) and navigate into the project directory by doing

```
ssh build-sb  
cd /projects/uoaXXXXX
```

where XXXXX corresponds to the project code. Next, download the following on your workstation:

- Planck Likelihood Code⁴
- Planck baseline likelihood data sets⁴
- CosmoMC⁵
- CosmoChord (CosmoMC-enabled version of PolyChord)⁶
- ModeChord⁷,

and move them into the cluster environment by executing

```
scp -r file_you_want_to_move abcd123@login.uoa.nesi.org.nz:/projects/uoa00518
```

Before doing anything else, load the appropriate module

```
module load intel/2015.02
```

The newest module (at the time of writing) intel/2017a has compatibility issues. **NB: Make sure that everything is compiled with the same module.**

Follow the instructions by Antony Lewis⁸ to install the Planck likelihood. The only deviation from the instructions is that in the 4th step, instead of

```
./waf configure --lapack_mkl=$MKLROOT --install_all_deps
```

execute

```
./waf configure --install_all_deps
```

instead. Before building CosmoMC (i.e. running ‘make’), remember to move/copy the zipped CosmoChord and ModeChord (in that order) files and extract the contents. The building process will automatically detect PolyChord and ModeCode. Additionally, in CosmoMC/source/Makefile, change the line (near the top)

```
MPIF90C ?= mpif90
```

to

```
MPIF90C ?= mpiifort
```

³<https://wiki.auckland.ac.nz/display/CER/How+to+log+in+using+ssh+keys>

⁴<http://pla.esac.esa.int/pla/#cosmology>

⁵<http://cosmologist.info/cosmomc/readme.html>

⁶https://ccpforge.cse.rl.ac.uk/gf/project/polychord/frs/?action=FrsReleaseBrowse&frs_package_id=249

⁷<https://github.com/ucl-cosmoparticles/modechord>

⁸http://cosmologist.info/cosmomc/readme_planck.html

for the version of Fortran most compatible with the cluster module intel/2015.02. At this point, feel free to execute

```
make
```

in the CosmoMC folder.

Start off by running a test case to make sure everything is working. We will first set up the test case and then elaborate on the input file. In the CosmoMC folder, open up a text editor for `test.ini`. Add the line

```
file_root = first_test #to your liking
```

under

```
root_dir = chains/
```

Then change the logical from F to T in

```
checkpoint = F
```

also change the number from 10 to 0 in

```
indep_sample = 10
```

The next step is to set up a job script for the cluster. In

```
/projects/uoa00518/
```

set up a new text file with the extension `.sl` (e.g. `modechord_job.sl`) and use this minimal working example

```
#!/bin/bash -e # shebang - points to path of program
#SBATCH -J first_test #job name to keep track of it
#SBATCH -A uoa00518 #project name
#SBATCH -time=20:00:00 #how long you want the job to go on for; more on this below
#SBATCH -ntasks=16 #MPI tasks
#SBATCH -mem-per-cpu=4096 #4GB
#SBATCH -cpus-per-task=8 #threads per MPI
#SBATCH -C avx #AVX nodes are faster

module load intel/2015.02 #module needed for the job to run
ulimit -s unlimited #to prevent segmentation fault
cd /projects/uoa00518/Check_29Oct/cosmomc #tells program where the parameter file
is stored
srun ./cosmomc test_planck.ini #run the cosmological model
```

If one follows the steps above and runs the job using

```
sbatch modechord_job.sl
```

they will see the message

```
Submitted batch job xxxxxxxx
```

then one can use the command

```
squeue -u [insert username]
```

to track the progress of the job. It is also possible to set up the job script such that an email is sent once the job starts and when the job ends (including failures/errors)⁹.

Once the job is running, one can check the ‘progress’ of the job by looking at the rate at which the evidence values are converging. Execute

```
grep -iaw --color "log(z)" slurm-xxxxxxxx.out
```

to look at the output file for the job.

Here are some miscellaneous, but important tips:

1. Visit <https://web.ceres.auckland.ac.nz/portal/#/portal/hpc/cgi-bin/noheader/heatmap.cgi> to:
 - (a) Check out the current load of the cluster
 - (b) Check the jobs that are being queued. This is useful to see the approximate start time of your time - hover over Cluster Status, click on Queued Jobs, then find your job. Note this cannot be done with job arrays.
 - (c) Look at the job history. Hover over Cluster Job History to see:
 - i. Job Statistics - summarises the number of jobs and the resources used thus far. One can also check the number of core hours left by running

```
show_my_projects
```

in the login node of the cluster. This is important! Jobs will **stop** running once the allocated resources for the project run out. However, it is possible to ask for more resources, so do check to make sure that one has enough resources.

- ii. Detailed Job History - Summarises each completed job (whether failed or not), including runtime, number of core hours used, job name, and the Job ID.
2. One will notice that

```
ntasks=16  
cpus-per-task=8
```

in the script file. We found that this is the best combination for the evidence calculations to run optimally. However, one should, before their proper runs, test different configurations

⁹<https://support.nesi.org.nz/hc/en-gb/articles/115000194910-Submitting-Slurm-Jobs-on-Pan>

to see what is their best combination. Runs typically took 25-35 hours for the monomial potentials, and about 50 hours for the inflection point inflaton. This is with 1000 live points and 125 repeats per chain length (i.e. `num_repeats = 125`).

3. Write different parameter files for the different models of inflation to not get confused.
4. Regarding `CosmoMC`-related errors, one can either look in `CosmoCoffee`¹⁰ or make a post there.
5. Above, we wrote that we should have

```
checkpoint = T
```

Enabling this setting allows for `.resume` files to be created. So if a job ends prematurely (due to wall time limit), the job can be started again (make sure settings are exactly the same) and ‘resumed’ rather than starting all over again. These are saved in the same folder as the produced chains. This is useful because:

- (a) there is no need to run one 50-hour job with a wall time (of say) 60 hours, where the job could be queued for a long time;
- (b) running 2-3 jobs of about 20 hours of wall-time each means that the job stays in the queue for a shorter time

However, they tend to be large files on the order of 1GB, so delete them once the run is complete.

¹⁰<http://cosmocoffee.info/viewforum.php?f=11>

8.5 Typical Parameter File

```
#Use Planck 2015 likelihoods
DEFAULT("./batch2/plik_dx11dr2_HM_v18_TT.ini) #high-l temperature likelihood
DEFAULT("./batch2/lowTEB.ini) #low-l temperature and polarization polarisation
#DEFAULT("./batch2/lowl.ini) #low-l temperature without polarisation
#DEFAULT("./batch2/lensing.ini) #for lensing

#other likelihoods
DEFAULT("./batch2/BAO.ini)
DEFAULT("./batch2/BKPlanck.ini)

#general settings
DEFAULT("./batch2/common.ini)

## INFLATION MODEL TO USE
DEFAULT(Models/lphi4/lphi4.ini)

## Reheating settings:
## Instant reheating
#DEFAULT(batch2/modecode_inst.ini)
DEFAULT(batch2/modecode_reheat3a.ini) #non-instant reheating

## Defaults
DEFAULT(batch2/modecode_defaults.ini)
DEFAULT(batch2/modecode_adjustments.ini)

# Many model parameters can be 'un-physical'. We make use of cosmomc's logzero
# functionality, but this requires that it doesn't stop when it hits an error
stop_on_error= F

#high for new runs
MPI_Max_R_ProposeUpdate = 30

# used for faster convergence (more efficient sampling of likelihood)
propose_matrix = ./planck_covmats/base_BAO_TT_lowTEB_plik.covmat

#folder where files (chains, checkpoints, etc.) are stored
root_dir = ./chains/

#root name for the files produced
file_root = lphi4_bkp
```

```

#action = 0 to MCMC, action = 1 to postprocess .data file
#action = 1 for important samples, action = 4 to quickly test likelihoods
#action = 5 for the PolyChord sampler
action = 5
DEFAULT(batch2/polychord.ini)
nlive = 1000
# was set to a number high enough so that the error in the evidences was about 0.20
num_repeats = 125

num_threads = 8
start_at_bestfit = F
#use feedback = 2 for more detailed output - very useful for error diagnosis
feedback = 1 #limited feedback
use_fast_slow = T

#to create .resume files
checkpoint = T

#sampling_method = 7 is a new fast-slow scheme good for Planck
sampling_method = 7
dragging_steps = 3
propose_scale = 2

# Set > 0 to make data files for importance sampling
# This is for rerunning chains with a different likelihood. Might be useful when # the
final_data_release for Planck comes out. indep_sample = 0

#small speedups for testing
get_sigma8 = F
#already F in batch2/modecode_adjustments.ini

#REMEMBER, to use lensing, turn OFF semi slow parameters.
##### Semi Slow parameters ON #####
# Turn on semi-slow parameters
use_nonlinear_lensing = F
block_semi_fast = T

# Set up the fraction of time to spend on each type of parameter
nest_frac_slow = 0.75
nest_frac_semi_slow = 0.20
nest_frac_semi_fast = 0.00
nest_frac_fast = 0.05

##### Semi Slow parameters OFF #####
# Remove the equivalent lines directly above, and uncomment
# the lines below in order to turn on non-linear lensing
# (and turn off semi slow parameters)

# # Turn off semi-slow parameters
#use_nonlinear_lensing = T
#block_semi_fast = F
#

```

```

# # Set up the fraction of time to spend on each parameter
#nest_frac_slow = 0.95
#nest_frac_semi_slow = 0.00
#nest_frac_semi_fast = 0.00
#nest_frac_fast = 0.05

## priors for physical parameters
H0_min = 20
H0_max = 100

#to vary parameters, set param[name] = center, min, max, start width, propose_width
#for fixed, can just fix fixed value

#MODIFIED P(K)
#inflationary potential parameters
#N_pivot
param[N_pivot] = 50.0 20.0 90.0 0.1 0.1
#vparams array
param[vpar1] = -12.82 -16.0 -10.0 0.001 0.001
param[vpar2] = 0
param[vpar3] = 0
param[vpar4] = 0
param[vpar5] = 0
param[vpar6] = 0
param[vpar7] = 0
param[vpar8] = 0
param[vpar9] = 0
param[vpar10] = 0
param[vpar11] = 0
param[vpar12] = 0
param[vpar13] = 0
param[vpar14] = 0
param[vpar15] = 0
param[vpar16] = 0
param[vpar17] = 0
param[vpar18] = 0
param[vpar19] = 0
param[vpar20] = 0
# END MODIFIED P(K)

param[omegabh2] = 0.02225 0.019 0.025 0.0001 0.0001
param[omegach2] = 0.12 0.095 0.145 0.001 0.0005
param[theta] = 1.0411 1.03 1.05 0.004 0.004
param[tau] = 0.09 0.01 0.40 0.001 0.001

param[logA] = 3.1 2.5 3.7 0.001 0.001
#log[1010 A_s]
param[ns] = 0.96 0.9 1.02 0.004 0.002
inflation_consistency = T

```

```

param[omegak] = 0
#param[w] = 0.33333 -1.0 1.0 0.001 0.001

#altered on 7 Sept
param[r] = 0.03 0 2 0.001 0.001
compute_tensors = T

param[nrun] = 0
param[nrunrun] = 0

neutrino_hierachy = degenerate
num_massive_neutrinos = 1
param[mnu] = 0.06

```

8.6 Making Triangle Plots

```

chain = '/Users/masonng/Documents/University/Honours Project/cosmomc/chains/'
# where the chains are stored
dirlist = [chain, chain+'planck/000_omegach2']
# tells the code where the chain is stored; can be altered to include your own folders
g = plots.getSubplotPlotter(chain_dir=dirlist, analysis_settings='ignore_rows':0.2)
# generates .pysamples for GetDist. Also include burn-in settings here if desired
roots = ['base_plikHM_TT_lowl', '000_omegach2']
# the root files that you want. You can add multiple roots to compare triangle plots.
params = ['omegabh2', 'logA', 'ns', 'tau', 'H0']
# the parameters you want to investigate
param_3d = None
g.triangle_plot(roots, params, plot_3d_with_param=param_3d, filled_compare=True,
shaded=False)
g.export('/Users/masonng/Documents/University/Honours Project/000_omegach2.pdf')

```